UNIVERSITY OF CALIFORNIA
Los Angeles

From the galactic to atomic scale: understanding planet formation and evolution

A dissertation submitted in partial satisfaction
of the requirements for the degree
Doctor of Philosophy in Planetary Science

by

Akash Gupta

2023

ABSTRACT OF THE DISSERTATION

From the galactic to atomic scale: understanding planet formation and evolution

by

Akash Gupta
Doctor of Philosophy in Planetary Science
University of California, Los Angeles, 2023
Professor Hilke E. Schlichting, Chair

The discovery of thousands of planets since 1995 has transformed how we perceive our place in this universe. One of the most profound findings since is the unexpected dearth of close-in planets of sizes 1.5 to 2.0 Earth radii, i.e., a radius valley. This valley divides the population of the most abundant class of planets yet known, those between the sizes of Earth and Neptune, into (1) super-Earths: planets smaller than 1.5 Earth radii with rocky, Earth-like bulk compositions, and (2) sub-Neptunes: planets larger than 2 Earth radii with hydrogen-rich atmospheres or interiors with substantial amounts of ices.

The origin of the radius valley is typically attributed to atmospheric escape due to photoevaporation. Through this work, we have demonstrated that atmospheric mass-loss driven by the cooling luminosity of a planet and its host star's bolometric luminosity, i.e., the core-powered mass-loss mechanism, can also explain this observation, even in the absence of any other process. In a nutshell, our work shows that the typical observed exoplanet has an Earth-like interior composition and accreted a hydrogen atmosphere from

the protoplanetary disk. However, over millions to billions of years, some planets lost their atmospheres because of core-powered mass-loss and transformed into super-Earths. In contrast, those that survived with their primordial atmospheres are today's sub-Neptunes.

For this work, we used analytical theory and numerical simulations to model a planet's thermal evolution and atmospheric escape and explored the impact of this mechanism on planet demographics. We find that the core-powered mass-loss mechanism explains not just the bimodality in planet sizes but even the numerous trends observed in the planet demographics across various planetary and host star properties. For instance, we find that in the planet size-orbital period space, the radius valley slope is -0.11 across FGKM dwarfs, which is in excellent agreement with observations. In addition, my work gives several insights into the nature of these planets. As an example, we find that most close-in super-Earths and sub-Neptunes formed with hydrogen envelopes. This finding has major implications for the chemical evolution of their atmospheres. Finally, we also seek testable predictions of the core-powered mass-loss theory. For example, we predict that the slope of the radius valley decreases in magnitude in the planet size-stellar mass space as the stellar mass decreases from 1 to 0.1 Solar masses. In the same vein, with my collaborators, we find that a powerful diagnostic to distinguish between the signatures of core-powered mass-loss and photoevaporation is to explore the radius valley in the three-dimensional phase space of planet size-stellar mass insolation flux. Many of these tests are being employed today by observational studies.

One of our significant findings, also corroborated by other contemporary theoretical and observational studies, is that most observed exoplanets have hydrogen atmospheres interacting with molten or super-critical interiors for millions to billions of years. In our Solar system, we see this for planets such as Jupiter and Neptune. Studies show that such interactions can have far-reaching implications for an atmosphere's composition, structure,

and evolution. However, we hardly understand these interactions, and studying them in a laboratory is difficult. The last chapter presents a novel method to address this problem via computational experiments based on density functional theory molecular dynamics.

Specifically, we examined how hydrogen and water interact under conditions similar to those found in planets such as Uranus and Neptune. We determined their phase diagram, which is in good agreement with laboratory experiments. Our findings indicate that planets like Neptune and Uranus have regions where hydrogen and water are thoroughly mixed, as well as regions of compositional gradients. We identify the pressure depths where these compositional changes likely happen in Uranus and Neptune and find that these locations are strongly correlated with the variations in observationally constrained density-pressure profiles of these planets. Furthermore, our results help elucidate the physical and chemical processes responsible for Neptune's higher internal heat flux compared to Uranus. We find that this difference in heat flux can be attributed to a higher degree of water-hydrogen demixing in Neptune's interior which would have led to the release of larger amounts of gravitational energy. Additionally, we identified regions where the magnetic fields of these planets are likely generated and discussed how their different magnitudes are also a possible by-product of hydrogen-water mixing properties. Our results highlight the importance of understanding the interaction between the fundamental building materials of planets if we want to develop a comprehensive understanding of how planets, in our Solar system and beyond, form and evolve.

The dissertation of Akash Gupta is approved.

David C. Jewitt

Smadar Naoz

Erik A. Petigura

Lars P. Stixrude

Hilke E. Schlichting, Committee Chair

University of California, Los Angeles

2023

TABLE OF CONTENTS

LIST OF FIGURES

LIST OF TABLES

ACKNOWLEDGMENTS

First and foremost, I would like to thank my advisor, Hilke Schlichting, for her unending support, care, guidance, and encouragement throughout my time at UCLA. Not only has she taught me innumerous things about how to be a better scientist and person, but I have so much enjoyed my time working with her, exploring how distant Earth-like worlds are born. I am also indebted to Lars Stixrude for his time and patience in teaching me how quantum mechanics can help us understand what happens inside planets and for giving me the chance to work with him during the latter stages of my PhD. I will forever cherish my time working with both of them at UCLA.

I would also like to thank the other members of my thesis committee, David Jewitt, Erik Petigura, and Smadar Naoz, for all their frank advice, and support in taking new initiatives throughout graduate school. In addition, my academic journey would not have been as enriching as it has been without the exposure that Edward Young, David Paige and James Owen gave me to new subjects in astrophysics and planetary science. At the same time, I feel fortunate to have had the chance to collaborate with James Rogers, Dakotah Tyler, Raissa Estrela, and Mark Swain. Furthermore, I would also like to thank the amazing EPSS staff for their hard work behind the scenes, especially Elyse Chou, Carlene Brown, Rod O' Conner, and Lauri Holbrook.

Last but not least, I feel incredibly lucky to have not only a family who has supported my journey in exploring a career in research and my move to another country in its pursuit but also in finding a family away from home: my friends and colleagues from my time at UCLA, IIT Kanpur and in the exoplanet community. During my stay at UCLA, I am particularly thankful to have met William Misener, Leslie Insixiengmay, Tyler Powell, Yufan Xu, Weixin Yang, Ariel Graykowski, Kevin Shao, Sebastian Krause, Han Bao, Abijah Si-

mon, Hanna Graykowski, Colin Wilkins, Fekireselassie Beyene, Valeria Jaramillo, Elisha Jhoti, Megan Li, Ashley Schoenfeld, Jaahnavee Venkatraman, Kyle Webster, Emily Whittaker, Lauren Tafla, Travis Gilmore, Francis Dragulet, David James, Zijin Zhang, Xiyuan Bao, Jason Utas, Jeffrey Osterhout, Ethan Tsai, Mai Tran, Francisco Spaulding-Astudillo, Raquel Nuno, Julia Miller, Saeed Mohanna, Ashna Aggarwal, Heather Kirkpatrick, Daniel Fineman, Liutauras Rusaitis, Sarah Millholland, Malena Rice, Alexandra Doyle, and David Rice. I am grateful that they have always been there for me, both academically and personally. On certain days they taught me about quantum mechanics, on others, they taught me how to drive and sometimes, best of all, treated me to their delicious home-cooked food! Without them, these last few years would not have been so memorable!

At the same time, I am also grateful to have come to know of a number of amazing friends from my time at IIT Kanpur and before, who have been there all these years for whenever I have needed them, including Harsh Gupta, Rasool Ahmad, Unnat Jain, Hemant Meharchandani, Deepanshu Singhania, Indra Kanshana, Amandeep Gupta, Sarthak Jain, Jai Prakash Menaria, Rishabh Gupta, Abhishek Sharma, Shubham Gupta, Sandesh Chopade, Amol Agarwal, Nitin Gupta, and Sriram Tejavath.

Finally, I would also like to acknowledge the funding provided by the National Aeronautics and Space Administration (NASA) under the Future Investigators in NASA Earth and Space Science and Technology (FINESST) grant, which supported three years of my graduate studies. In addition, part of this thesis was facilitated by the computational and storage support provided by the UCLA Institute for Digital Research and Education's Research Technology Group/Hoffman2 Cluster.

Thank you again to everyone who has helped me along the way. I am truly grateful for your support.

VITA

2017 - 2019 University of California, Los Angeles
M.S. in Geophysics and Space Physics

2011 - 2016 Indian Institute of Technology, Kanpur
B.Tech. and M.Tech. Dual degree in Aerospace Engineering

PUBLICATIONS

Gupta, A., and Stixrude, L. 2023. In preparation.
Investigating the solubility of hydrogen in water using ab initio molecular dynamics: implications to water-rich planets and exoplanets

Owen, J. E., Murray-Clay, R. A., Schreyer, E., Schlichting, H. E., David, A., **Gupta, A.**, Loyd, R. O. P., Shkolnik, E. L., Sing, D. K. & Swain, M. R., 2022. *MNRAS*. 518, 4357-4371.
The fundamentals of Lyman-alpha exoplanet transits

Gupta, A., Nicholson, L. and Schlichting, H. E. 2022. *MNRAS*, 516, 4585-4593.
Properties of the radius valley around low mass stars: Predictions from the core-powered mass-loss mechanism

Rogers, J. G., **Gupta, A.**, Owen, J. E. & Schlichting, H. E. 2021. *MNRAS*, 508, 5886-5902.
Photoevaporation vs. core-powered mass-loss: Model comparison with the 3D radius gap

Gupta, A. and Schlichting, H. E. 2021. *MNRAS*, 504, 4634-4648.
Caught in the act: Core-powered mass-loss predictions for observing atmospheric escape

Gupta, A. and Schlichting, H. E. 2020. *MNRAS* 493, 792-806.
Signatures of the core-powered mass-loss mechanism in the exoplanet population: Dependence on stellar properties and observational predictions

Estrada, R. Swain, M., **Gupta, A.**, Sotin, C. and Valio, A.. 2020. *ApJ.* 898, 104-109.
Evolutionary tracks of H/He envelopes of the observed pop. of sub-Neptunes and super-Earths

Gupta, A. and Schlichting, H.E. 2019. *MNRAS* 487, 24-33.
Sculpting the valley in the radius distribution of small exoplanets as a by-product of planet formation: The core-powered mass-loss mechanism

Gupta, A., Nadkarni-Ghosh, S. and Sharma, I. 2018. *Icarus* 299, 97-116.
Rings of non-spherical, axisymmetric bodies

CHAPTER 1

Introduction

Until the late 20th century, we only knew of the eight planets in our Solar system. This number had hardly changed over the last four millennia — the ancient astronomers from Babylon itself had reportedly known of the six planets closest to the Sun. In the thousands of years that have followed, scientists have studied these distant worlds and other planetary bodies in great detail, but we were always confined within the realm of our Solar system. However, things changed in the early 1990s. With the discovery of 51 Pegasi b, the first planet ever found around a Sun-like star outside our Solar system, Mayor & Queloz (1995) and other researchers started a revolution which has since led to the detection of over five thousand planets; see also Wolszczan & Frail (1992). These discoveries have since transformed how we perceive our place in this universe.

According to the latest National Academy of Sciences' Decadal Surveys on *Astronomy and Astrophysics*, and *Planetary Science and Astrobiology*, the search and characterization of Earth-like exoplanets is now a leading objective. Once a topic of philosophical discourse, the search for a habitable Earth-like planet is now a tractable, albeit challenging, scientific goal. However, to realize this, we need to first understand how such planets form and evolve. This Ph.D. thesis is a step in that direction — containing a series of papers that explore how the most abundant class of planets in our galactic neighborhood, those between the sizes of Earth and Neptune, form and evolve. In the following sections, we give an

overview of the observational and theoretical studies that motivated the work discussed in the subsequent chapters.

1.1 Discovering exoplanets

Today, numerous techniques are being used to discover exoplanets. In the 1990s, however, it all started with the method of radial velocity (RV). The idea behind this technique is that if a planet is orbiting a star, their mutual gravitational interaction will make them orbit their common center of mass. Therefore, if someone observes such a star, they should notice the star wobble, i.e., to have a reflex motion due to a companion planet, as it zooms across the sky towards or away from the observer. The radial velocity method involves ascertaining the existence of a planet by estimating this reflex motion by measuring the Doppler shift in the light coming from the star. Such measurements not only help determine the existence of a planet but also allow constraints on the accompanying planet's mass. This method has led to the discovery of hundreds of planets to date – allowing, for the first time, to study planet formation and evolution at a statistical level. In the first decade of RV surveys itself, there were several intriguing discoveries, such as the existence of a correlation between the occurrence of giant planets and host star metallicity (e.g., Fischer & Valenti, 2005).

The era of RV discoveries was soon eclipsed by the method of transits with the launch of NASA's *Kepler* space telescope in 2009, which has since led to the discovery of over four thousand planets during its roughly decade long operation (e.g., Borucki et al., 2010); see Figure 1.1. This method relies on the fact that if a planet orbits its parent star such that it comes in between the star and the observer, there should be a periodic dimming of the light coming from that star (e.g., Charbonneau et al., 2000). The degree of dimming depends on the square of the ratio of the planet's size to the host star's size, and the periodicity of

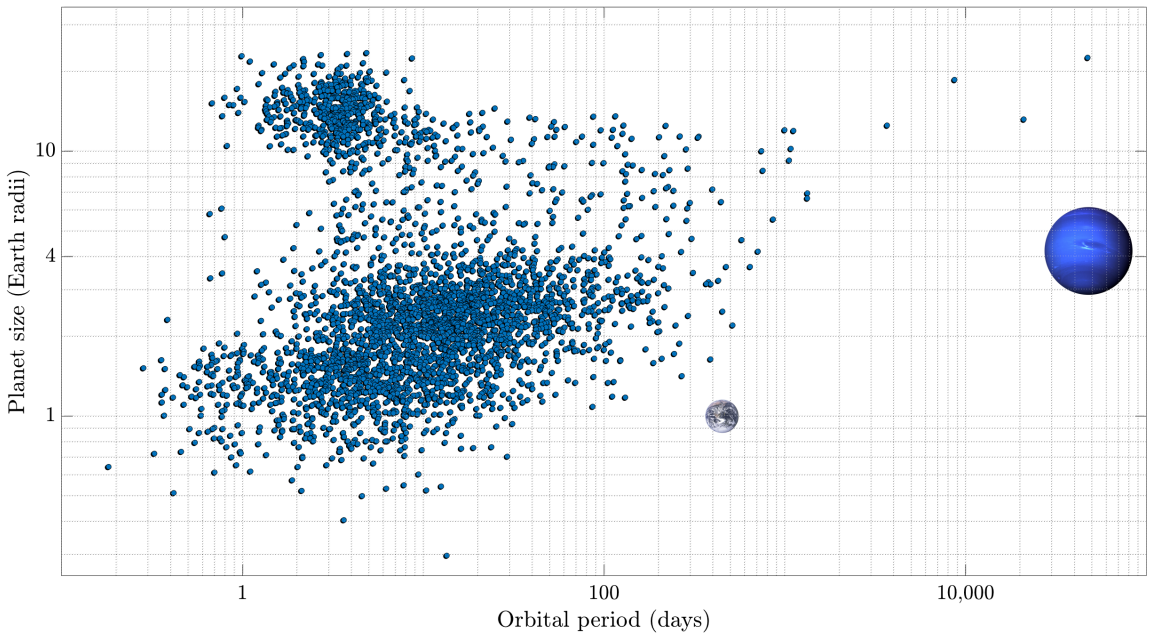

Figure 1.1: Distribution of exoplanets with observed planet sizes across the planet size-orbital period space. This dataset includes planets with observed sizes using the transit method, those with orbital periods $\lesssim$ 2000 days, and direct imaging, those with orbital periods $\gtrsim$ 2000 days. To put this exoplanet population into context, we also plot Earth and Neptune, denoted by their images. Most of these planets, except four, were detected using the transit method and are thus evidently limited to short orbit periods. This plot also reflects the abundance of small planets, those roughly between the sizes of Earth and Neptune, even when not corrected for the observational bias towards larger planets being easier to find. Source: NASA Exoplanet Archive (December 1, 2022).

the dimming corresponds to the planet's orbital period. Therefore, this method helps us obtain the respective planet's radius and orbital period. On the flip side, this method is thus biased towards finding planets that are larger relative to their host star and at shorter orbital periods. This bias can, however, be systematically corrected for (e.g., Fulton et al., 2017). Such bias corrections then allow us to estimate the *true* occurrence of planets in nature. From here onwards, any reference to the 'planet occurrence rate' or simply 'occurrence' will refer to this bias-corrected occurrence and not the raw, observed distribution of planets. The thousands of planets that *Kepler* and other observatories have discovered using this transit technique have revealed unprecedented details about planet formation and evolution.

1.2 Super-Earths, sub-Neptunes, and the radius valley

The last three decades of exoplanet discoveries have thrown one surprise after another at the scientific community. The very first exoplanet, 51 Pegasi b, was found orbiting its Sun-like host star at a period of ∼4.2 days, which meant it had a planetary equilibrium temperature of ∼ 1300 K. Constraints on its mass suggested it to be similar to our Jupiter. On the other hand, in our Solar system, Mercury is the closest planet to the Sun with an orbital period of 88 days, whereas Jupiter orbits the Sun only every 12 years. So naturally, the discovery of 51 Pegasi b not only astounded everyone, including the researchers who reported it, but the finding was met with skepticism in the community. After all, at the time, no planet formation theory predicted a Jupiter-like planet to exist that close to its host star. Nevertheless, in the years that followed, this discovery of 51 Pegasi b and other 'hot-Jupiters' revolutionized the field of astronomy and planetary science and paved the way to a number of theoretical and observational investigations and a deeper understanding of how giant planets form and evolve.

The discoveries facilitated by the transit method have inspired a similar paradigm shift in our understanding of small planets, which had been elusive due to technological limitations in the pre-*Kepler* era. At first, it started with finding small planets in regions where no planet exists in our Solar system, with their mass measurements revealing a fascinating degree of compositional diversity (e.g., Charbonneau et al., 2009; Batalha et al., 2011). However, soon *Kepler* unraveled that planets between the sizes of Earth and Neptune are, by far, the most abundant class of planets in our galactic neighborhood (Fressin et al., 2013; Petigura et al., 2013), having an occurrence rate that is an order of magnitude higher than that observed for giant planets (e.g., Petigura et al., 2017).

Further follow-up studies of the *Kepler* planets and their host stars, led by the California-Kepler Survey (CKS) team in particular, then revealed something unexpected: the most abundant class of planets, those between the sizes of Earth and Neptune ($\sim$ 4 Earth radii), are in fact divided into two planet populations by, what is now referred to as, the *radius valley* or *gap* (e.g., Fulton et al., 2017); see Figure 1.2. Interestingly, past studies exploring the role of photoevaporation in atmosphere loss had already predicted the existence of this feature and found tentative evidence for it in the Kepler Input Catalog (Owen & Wu, 2013; Lopez & Fortney, 2013). But this was concluded with certainty only in 2017. Follow-up RV studies measuring masses of accessible planets in these two populations revealed that planets smaller than $\sim$ 1.5 Earth radii have higher densities consistent with rocky, Earth-like composition. In contrast, planets with sizes $\gtrsim$ 2 Earth radii have lower densities such that they likely have H-dominated atmospheres or ice-rich interiors (e.g., Dressing et al., 2015). Studies have thus suggested that the radius valley likely marks a transition from a population of smaller, rocky planets, i.e., *super-Earths*, to a population of larger planets with significant H/He envelopes or ice-rich interiors, i.e., *sub-Neptunes*.

Several questions then arise, given this surprising and statistically significant obser-

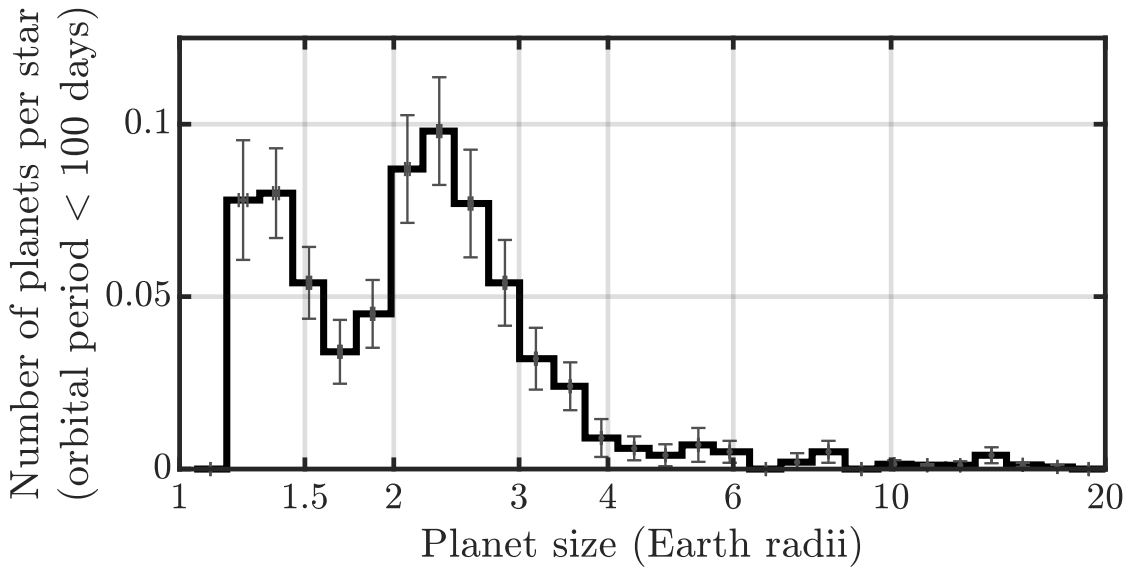

Figure 1.2: Planet occurrence rate as a function of planet size as reported by the California-Kepler Survey in Fulton et al. (2017). Small exoplanets are found to have a substantially higher occurrence when compared to any other class of planets observed. The dearth of planets of sizes 1.5 to 2 Earth radii is referred to as the radius valley. This valley divides this population of the most abundant class of planets into (1) super-Earths, i.e., smaller, rocky planets with sizes $\sim$ 1 to 1.5 Earth radii, and (2) sub-Neptunes, i.e., larger, puffy planets with likely H-dominated atmospheres or ice-rich interiors and with sizes $\sim$ 2 to 4 Earth radii.

vation, for instance: What is the origin of the radius valley? Do super-Earths and sub-Neptunes have a common origin, and if so, how did they form? Otherwise, do they form through distinct formation and evolution pathways? Can the radius valley tell us something about the influence of the stellar environment on planet formation? What are the physical characteristics of these planets? Is a rocky 'super-Earth' Earth analog? Since its discovery, this feature of planet demographics has thus become the prime observational evidence of planet formation and evolution processes and the majority of this thesis focuses on answering the questions outlined above.

There are two schools of thought that attempt to explain this radius valley observation (Bean et al., 2021). According to one, the radius valley is primordial. For instance, according to Zeng et al. (2019) and Mousis et al. (2020), super-Earths are planets that were born rocky, whereas sub-Neptunes are water or ice-rich planets, with ices amounting to $\sim 50\%$ of the planet's composition by mass. On the other hand, Lee & Connors (2020) suggest that super-Earths are those planets that are so small that they could have hardly accreted any primordial H atmosphere, unlike sub-Neptunes.

The other school of thought claims that the radius valley is a result of atmospheric loss driven by *core-powered mass-loss* and/or photoevaporation. Today, this is considered as the leading idea behind the origin of the radius valley given its success in explaining a multitude of radius valley observations (e.g., Bean et al., 2021).

According to the photoevaporation theory, the short wavelength/high energy radiation from the host star can inject energy into the upper regions of the atmosphere by ionizing it, which can then drive hydrodynamic winds and thus lead to atmospheric loss (e.g., Owen & Wu, 2013; Lopez & Fortney, 2013; Jin et al., 2014; Owen & Wu, 2017). This theory has been explored by numerous studies over the last decade.

On the other hand, much of this thesis is dedicated to exploring the more recently proposed theory of core-powered mass-loss and how it could be the dominant process that led to the formation of the radius valley (Ginzburg et al., 2018; Gupta & Schlichting, 2019, 2020, 2021; Gupta et al., 2022). This is explored in Chapters 2 through 5. According to this theory, most observed exoplanets formed inside the ice line and, unlike Earth, finished forming in the presence of these natal disks. Besides accreting an Earth-like rocky, silicate interior, these planets thus also accreted primordial atmospheres of H, which puffed up their sizes - like today's sub-Neptunes. However, over the subsequent millions to billions of years, certain planets lost their entire atmospheres, which transformed them into super-Earths. This atmosphere loss was driven by the thermal energy injected in these atmospheres due to a planet's own cooling luminosity and the host star's bolometric luminosity. The planets that survived with their primordial H atmospheres are today's sub-Neptunes. The radius valley is thus a signature of this evolution of gas-rich sub-Neptunes into rocky, Earth-like super-Earths. In these chapters, we use a simple analytic model to show how this theory can not only explain the observed bimodality in planet sizes but even the numerous trends observed in the planet demographics across the myriad planetary and host star properties. At the same time, we share several predictions and tests for ongoing and future observational studies, many of which are being employed today. An independent avenue to actively probe how gas-rich planets evolve is to search for direct observational signatures of atmospheric loss. In complement to population-level studies, we thus also investigate for planet candidates that could be actively losing their atmospheres today at a significant rate. This further allows us to identify planet candidates that likely harbor high-molecular weight secondary atmospheres, or low-density interiors with substantial amount of ices.

1.3 Interaction of H-rich atmospheres and planetary interiors

Given the work presented in this thesis and that in other contemporary studies, our current understanding is that most planets or their progenitors should have a hydrogen atmosphere (or protoplanetary disk) interacting with an interior of liquid or super-critical water (e.g., Uranus, Neptune or water-rich exoplanets) or silicates (e.g., the typical super-Earth or sub-Neptune), for millions to billions of years. Numerous theoretical studies suggest that this interaction can have far-reaching consequences for the structure, formation, and evolution of a planet and, thus, on its atmosphere's composition and planet demographics (e.g., Kite & Barnett, 2020; Schlichting & Young, 2022; Markham & Stevenson, 2021; Misener & Schlichting, 2022). In fact, we even have observational evidence of such interactions in our Solar system: the *Juno* spacecraft recently discovered that Jupiter's core is diluted by its atmosphere (e.g., Wahl et al., 2017).

However, we hardly understand how such primary building blocks interact under the conditions expected when planets form or at their interior-atmosphere interface during subsequent evolution. In these conditions, temperatures and pressures can exceed even 5,000 K and 50 GPa. Studying such interactions in a laboratory is thus not possible at present. Chapter 6 attempts to address this by investigating the interaction of a planet's hydrogen-dominated atmosphere and water-rich interior using quantum mechanics. This is the only way possible to understand such interactions today. Quantum calculations such as ab-initio molecular dynamics can help us predict material behavior with high accuracy. And studying the hydrogen-water system has the advantage of allowing comparison of our understanding of such interactions with the observational constraints on the interiors of Uranus and Neptune from existing and future spacecraft data (e.g., Voyager 2 and the Uranian Orbiter & Probe). As demonstrated in this chapter, H can completely dissolve in

large parts of the super-critical water-rich interior of Neptune-like planets, whereas in some regions, we expect compositional gradients. We will discuss how our results are consistent with experiments and, how they help us better understand the formation and evolution of planets and exoplanets such as Neptune and Uranus.

CHAPTER 2

Sculpting the Valley in the Radius Distribution of Small Exoplanets as a by-product of Planet Formation: The Core-Powered Mass-Loss Mechanism

[1]Recent observations revealed a bimodal radius distribution of small, short-period exoplanets with a paucity in their occurrence, a radius 'valley', around 1.5-2.0 $R_\oplus$. In this work, we investigate the effect of a planet's own cooling luminosity on its thermal evolution and atmospheric mass-loss (core-powered mass-loss) and determine its observational consequences for the radius distribution of small, close-in exoplanets. Using simple analytical descriptions and numerical simulations, we demonstrate that planetary evolution based on the core-powered mass-loss mechanism alone (i.e., without any photoevaporation) can produce the observed valley in the radius distribution. Our results match the valley's location, shape and slope in planet radius-orbital period parameter space, and the relative magnitudes of the planet occurrence rate above and below the valley. We find that the slope of the valley is, to first order, dictated by the atmospheric mass-loss timescale at the Bondi radius and given by $\mathrm{d}\log R_p/\mathrm{d}\log P \simeq 1/(3(1-\beta))$ which evaluates to -0.11 for $\beta \simeq 4$, where $M_c/M_\oplus = (R_c/R_\oplus)^\beta(\rho_{c*}/\rho_\oplus)^{\beta/3}$ is the mass-radius relation of the core.

[1]This chapter was previously published in similar form as Gupta, A. and Schlichting, H. E. 2019, MNRAS 487, 24-33.

This choice for β yields good agreement with observations and attests to the significance of internal compression for massive planetary cores. We further find that the location of the valley scales as $\rho_{c*}^{-4/9}$ and that the observed planet population must have predominantly rocky cores with typical water-ice fractions of less than $\sim 20\%$. Furthermore, we show that the relative magnitude of the planet occurrence rate above and below the valley is sensitive to the details of the planet-mass distribution but that the location of the valley is not.

2.1 Introduction

NASA's *Kepler* mission has unveiled a wealth of new planetary systems (e.g., Borucki et al., 2010). These systems offer new insights into the process of planet formation and evolution. One of *Kepler*'s key findings is that the most common planets in our galaxy, observed to date, are between 1 and 4 $R_\oplus$, i.e., larger than Earth but smaller than Neptune (Fressin et al., 2013; Petigura et al., 2013). Further observations revealed a transition in average densities at planet sizes $\sim 1.5\ R_\oplus$ (Marcy et al., 2014a; Rogers, 2015), with smaller planets having densities consistent with rocky compositions while larger planets having lower densities indicating significant H/He envelopes. In addition, Owen & Wu (2013) noticed a bimodal distribution of observed planet radii. Since then, refined measurements have provided strong observational evidence for the sparseness of short-period planets in the size range of $\sim 1.5 - 2.0\ R_\oplus$ relative to the smaller and larger planets, yielding a valley in the small exoplanet radius distribution (e.g., Fulton et al., 2017; Fulton & Petigura, 2018). For example, the California-*Kepler* Survey reported measurements from a large sample of 2025 planets, detecting a factor of ~ 2 deficit in the relative occurrence of planets with sizes $\sim 1.5 - 2.0\ R_\oplus$ (Fulton et al., 2017). Studies suggest that this valley likely marks the transition from the smaller rocky planets: 'super-Earths', to planets

with significant H/He envelopes typically containing a few percent of the planet's total mass: 'sub-Neptunes' (e.g., Lopez & Fortney, 2013; Owen & Wu, 2013; Rogers, 2015; Ginzburg et al., 2016). Furthermore, the location of this valley is observed to decrease to smaller planet radii, R_p, with increasing orbital period, P. In a recent study involving asteroseismology-based high precision stellar parameter measurements for a sample of 117 planets, a slope $\mathrm{d}\log R_p/\mathrm{d}\log P = -0.09^{+0.02}_{-0.04}$ was reported for the radius valley by Van Eylen et al. (2018). A similar value for the slope of $-0.11^{+0.03}_{-0.03}$ was reported by Martinez et al. (2019).

The observed valley in the exoplanet radius distribution has been attributed to photoevaporation of H/He atmospheres by high energy stellar radiation (e.g., Owen & Wu, 2013; Lopez & Fortney, 2013). Recent work showed that thermal evolution models with photoevaporation can reproduce the observed radius distribution (e.g., Owen & Wu, 2017; Van Eylen et al., 2018).

However, photoevaporation by high energy photons is not the only proposed mechanism for shaping the radius valley. Ginzburg et al. (2018) demonstrated that the core-powered mass-loss mechanism (Ginzburg et al., 2016) can produce the exoplanet radius distribution, even without photoevaporation, solely as a by-product of the planet formation process itself. In the core-powered mass-loss mechanism, it is the luminosity of the cooling planetary cores that provide the energy for atmospheric loss. The assembly of planetary cores results in large core temperatures as gravitational binding energy is converted into heat. Furthermore, if this assembly takes place in the presence of a gas disk, planetary cores not only accrete H/He atmospheres, but they are also prevented from cooling significantly since the optically thick H/He envelopes act like thermal blankets regulating the heat loss from both the core and envelope at the radiative-convective boundary (e.g. Lee & Chiang, 2015; Ginzburg et al., 2016). As a result, the temperature of super-Earth and sub-Neptune

cores is dictated by the maximum temperatures that still allows for the accretion of H/He envelopes onto the core. This temperature is approximately given by $T_c \sim GM_c\mu/k_BR_c$, where μ is the mean molecular weight of the atmosphere, k_B the Boltzmann constant, G the gravitational constant and M_c and R_c are the mass and radius of the planetary core, respectively. These core temperatures evaluate to about 10,000-100,000 K for planets with masses between Earth and Neptune and these cores and envelopes take Gyrs to cool (Ginzburg et al., 2016).

In this paper, we extend the results from Ginzburg et al. (2018) and show that the core-powered mass-loss mechanism can produce the valley's location, shape and slope in planet radius-orbital period parameter space, and the relative magnitudes of the planet occurrence rate above and below the valley. We further use it to constrain the planet's core composition and the mass-radius relation of the core. This paper is structured as follows: Section 2.2 is divided into several parts. In the first, we describe our planetary model, its structure and relevant equations. We then outline the core-powered mass-loss mechanism and define the parameters of the exoplanet population used in our numerical evolution calculations. We discuss our results in Section 2.3, which includes a comparison with observations and investigations into how our results depend on the physical parameters of the planet population. Our conclusions are summarized in Section 2.4.

2.2 Planet Structure and Evolution

In this section, we describe our model for the structure of the core and envelope of close-in super-Earths and sub-Neptunes and their evolution due to core-powered mass-loss after the dispersal of the gas disk. For a detailed review of this mechanism, the reader is referred to Ginzburg et al. (2016) and Ginzburg et al. (2018).

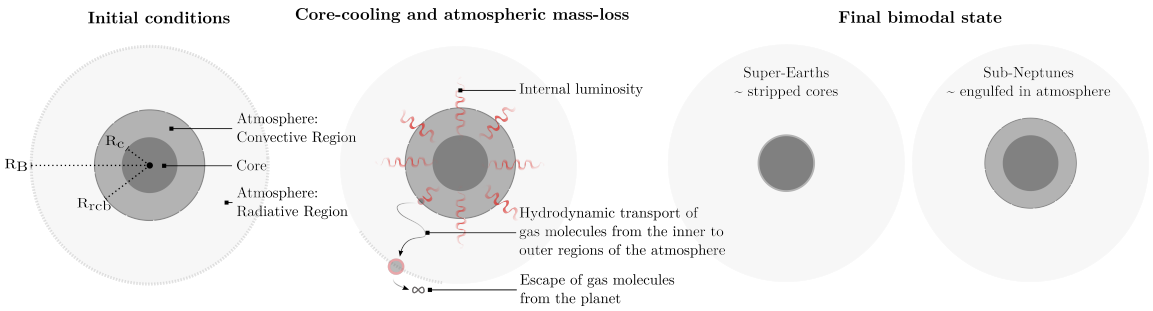

Figure 2.1: Schematic of the main stages in the evolution of a planet due to the core-powered mass-loss mechanism. *Left panel*: The primary components of the planet structure: core (dark gray), and atmospheric convective (gray) and radiative (light gray) regions. As shown, the convective region of the atmosphere extends from the core to the radiative-convective boundary, R_{rcb}, which is comparable to a few core radii, R_c, at the end of the disk dispersal phase (our initial condition), and the radiative region extends from the R_{rcb} to the Bondi radius, R_B. *Middle panel*: Illustration of the thermal evolution and atmospheric mass-loss at the Bondi radius. *Right panel*: The two end-member states at the end of 3 Gyrs. of evolution: (i) super-Earths, stripped rocky cores found below the valley, and (ii) sub-Neptunes, engulfed in H/He atmospheres and located above the valley.

2.2.1 Planet Structure

We assume a planet of radius R_p and mass M_p with a dense core surrounded by a gaseous atmosphere, with most its mass in the core such that $M_c \sim M_p$. We note here that by core we mean the non-gaseous part of the planet and such that this includes both the iron core and silicate mantle of an Earth analog. We assume, accounting for gravitational compression, that the mass-radius relationship for the core is given by $M_c/M_\oplus = (R_c/R_\oplus)^4(\rho_{c*}/\rho_\oplus)^{4/3}$, where ρ_{c*} is the density of the core scaled to an Earth mass, R_c is the radius of the core and $\oplus$ refers to the corresponding Earth values (Valencia et al., 2006; Fortney et al., 2007). For pure water/ice, silicate and iron cores, we assume ρ_{c*} to be 1.3 g cm^{-3}, 4 g cm^{-3} and 11 g cm^{-3}, respectively (Fortney et al., 2007).

We assume that all cores are initially surrounded by H/He envelopes of mass M_{atm} and define the atmosphere to core mass fraction as $f = M_{atm}/M_c$. As has been shown in previous works (e.g., Piso & Youdin, 2014; Lee & Chiang, 2015; Inamdar & Schlichting, 2015), the structure of the atmosphere is, to first order, well described by an inner convective region that contains most of the atmospheric mass and an outer radiative, nearly-isothermal, region of negligible mass. The transition between these two regions occurs at the radiative-convective boundary which we denote as R_{rcb}. We treat the R_{rcb} as the planet's effective radius, i.e., $R_p \simeq R_{rcb}$. This is a good approximation as the density profile changes sharply at the R_{rcb}. We model the atmosphere as an ideal gas.

The dispersal of the protoplanetary disk causes a loss of pressure support on the outer edge of the envelope, causing atmospheric mass-loss powered by the luminosity of the cooling inner regions of the atmosphere (Owen & Wu, 2016; Ginzburg et al., 2016). As a result, the envelopes of close-in planets rapidly shrink (roughly on the timescale on which the disk disperses) to thicknesses $\Delta R \simeq R_c$, where $\Delta R = R_{rcb} - R_c$ is the thickness of the

envelope measured from the core's surface. Since we are interested in the evolution of the planets after disk dispersal, we assume $\Delta R \simeq R_c$ as initial condition for the thickness of the planetary envelopes (see also Owen & Wu, 2017).

The atmospheric mass can be obtained by integrating the density profile over the convective region, which yields

$$M_{atm} = \frac{\gamma - 1}{\gamma} 4\pi R_c^2 \rho_{rcb} \Delta R \left(\frac{R'_B \Delta R}{R_c^2} \right)^{1/(\gamma-1)}, \tag{2.1}$$

where γ is the adiabatic index of the atmosphere, ρ_{rcb} is the density of the atmosphere at R_{rcb} and R'_B is the modified Bondi radius (Ginzburg et al., 2016), such that

$$R'_B \equiv \frac{\gamma - 1}{\gamma} \frac{G M_c \mu}{k_B T_{rcb}} \tag{2.2}$$

where μ is the molecular mass of the atmosphere, k_B is Boltzmann constant, G is the gravitational constant and $T_{rcb} \sim T_{eq}$ is the temperature at the R_{rcb}, and T_{eq} the equilibrium temperature for a given distance from the host star. Throughout this study, we assume Sun-like host stars.

The temperature at the base of the envelope is

$$T_c \simeq \frac{\gamma - 1}{\gamma} \frac{1}{k_B} \frac{G M_c \mu}{R_c^2} \Delta R, \tag{2.3}$$

which is valid for $R_c/R'_B \lesssim \Delta R/R_c \lesssim 1$ (Ginzburg et al., 2018). We ignore the ultra-thin regime, $\Delta R/R_c \lesssim R_c/R'_B \sim 0.1$, for which $T_c \sim T_{eq}$ as this regime cannot yet be detected in the exoplanet radius distribution. We also ignore any additional heat generated by radioactive decay in the core. Including this would delay the transition to the ultra-thin regime further, and it may lead to additional atmospheric mass-loss for planets whose loss is not limited by the cooling time or age of the system.

We model the core, to first order, as incompressible, molten and fully convective such that its temperature is close to isothermal and given by the temperature at the bottom of

the convective region, T_c. We assume that the core-envelope interface is well coupled such that the core temperature always matches that of the base of the adiabatic atmosphere.

As a result, the thermal and gravitational energy available for cooling is

$$E_{cool} \simeq g\Delta R \left(\frac{\gamma}{2\gamma - 1} M_{atm} + \frac{1}{\gamma} \frac{\gamma - 1}{\gamma_c - 1} \frac{\mu}{\mu_c} M_c \right), \tag{2.4}$$

where γ_c and μ_c are the adiabatic index and molecular mass of the core, respectively, and $g = GM_c/R_c^2$ is the surface gravity of the planet. The first and second term on the right-hand side correspond to the atmosphere's energy and core's thermal energy, respectively.

2.2.2 Evolution Model

We start our evolution models right after the disk dispersal phase. To distinguish our results from any atmospheric mass-loss due to photoevaporation, we only consider the planet's evolution due to its own cooling luminosity and its subsequent mass-loss.

As shown above, the core temperatures are, as a result from formation, of the order of $10^4 - 10^5$ K. Since the core-envelope interface is well coupled, the cooling of both the core and envelope is dictated by radiative diffusion through the radiative-convective boundary. This implies that the planet cools at a rate

$$L = -\frac{\mathrm{d}E_{cool}}{\mathrm{d}t} = \frac{64\pi}{3} \frac{\sigma T_{rcb}^4 R'_B}{\kappa \rho_{rcb}}, \tag{2.5}$$

where σ is the Stefan-Boltzmann constant and κ is the opacity at the R_{rcb}. Equations (2.4) and (2.5) can be combined to yield a cooling timescale of the envelope, t_{cool}, given by $t_{cool} = |E_{cool}/(\mathrm{d}E_{cool}/\mathrm{d}t)| = E_{cool}/L$. Following Freedman et al. (2008), we model the opacity at the R_{rcb} as $\kappa/0.1\ \mathrm{cm}^2\ \mathrm{g}^{-1} = (\rho_{rcb}/10^{-3}\ \mathrm{g\ cm}^{-3})^{0.6}$.

The energy required to lose the entire atmosphere is $E_{loss} \simeq gM_{atm}R_c$. Comparing this with the energy available for cooling given in Equation (2.4) yields that $E_{cool} \lesssim E_{loss}$ for

$M_{atm}/M_c > \mu/\mu_c \sim 5\%$ (heavy atmospheres) and $E_{cool} \gtrsim E_{loss}$ for $M_{atm}/M_c < \mu/\mu_c \sim 5\%$ (light atmospheres). Note, we ignored the γ and γ_c factors here for simplicity. This implies that, depending on the atmosphere to core mass-ratio after disk dispersal, planets can continue to evolve in two different ways. Planets with heavy atmospheres ($M_{atm}/M_c > \mu/\mu_c$) don't have enough energy to continually lose mass and their envelopes will cool and contract over time. In contrast, planets with light envelopes ($M_{atm}/M_c < \mu/\mu_c$) can, from an energy point of view, continue to lose mass over time. Furthermore, since for light envelopes $E_{cool} \gtrsim E_{loss}$ and since mass-loss proceeds at almost constant ΔR while decreasing the envelope density, atmospheric loss is a run-away process in the sense that energetically it gets easier with time (i.e., once the first half has been lost, it is even easier to loose the next half), ensuring that there is enough energy to lose the entire envelope (Ginzburg et al., 2016, 2018).

However, despite sufficient energy, planets with light atmospheres are not necessarily stripped of their envelopes because, analogous to a Parker type wind, atmospheric mass-loss proceeds at a finite rate dictated by the escape rate of molecules at the Bondi radius (Ginzburg et al., 2016; Owen & Wu, 2016). Since the hydrodynamic flow needs to pass through the sonic point and since the mass flux is conserved, it is convenient to determine the mass-loss rate at the sonic point, $R_s = GM_p/2c_s^2$, where $c_s = (k_B T_{eq}/\mu)^{1/2}$ is the isothermal speed of sound. This yields a mass-loss rate of $\dot{M} = 4\pi\rho_s R_s^2 c_s$, where ρ_s is the density at the sonic point, which can be related to the density at the radiative convective boundary by $\rho_s = \rho_{rcb}\exp(-2R_s/R_{rcb})$ in the limit that $R_s >> R_{rcb}$. The mass-loss rate at the Bondi radius can therefore be written as

$$\dot{M}^B_{atm} = 4\pi R_s^2 c_s \rho_{rcb} \exp\left(-\frac{GM_p}{c_s^2 R_{rcb}}\right). \tag{2.6}$$

From Equation (2.6) we define the atmospheric mass-loss timescale as $t_{loss} = |M_{atm}/(\mathrm{d}M_{atm}/\mathrm{d}t)|$.

This finite mass-loss rate is critical to the existence of planets in the valley and for explaining planets that have atmospheres of a few percent. The exponential dependence ensures that planets can hold on to their atmospheres because they did not have enough time for loss at larger orbital periods and/or that the cooling timescale can become shorter than the mass-loss timescale as a planet contracts during its evolution terminating any further mass-loss.

We follow the evolution of a given planet by simultaneously calculating its cooling and its atmospheric-loss due to core-powered mass-loss. The energy of the planet decreases as a function of time as dictated by its internal luminosity, such that

$$E_{cool}(t + \mathrm{d}t) = E_{cool}(t) - L(t)\mathrm{d}t, \tag{2.7}$$

where L is given by Equation (2.5). Similarly, the evolution of the atmospheric mass can be written as

$$M_{atm}(t + \mathrm{d}t) = M_{atm}(t) - min\left\{\dot{M}^{E}_{atm}(t), \dot{M}^{B}_{atm}(t)\right\}\mathrm{d}t, \tag{2.8}$$

where the mass-loss rate at the Bondi radius is given by Equation (2.6) and $\dot{M}^{E}_{atm} \simeq L(t)/gR_c$ is the energy-limited mass-loss rate. The energy-limited mass-loss rate should be regarded as an absolute upper limit as it assumes that all of the cooling luminosity goes into driving the mass loss. In reality, the efficiency of this cannot be a 100% since roughly half of the luminosity is radiated away, which is required, together with the irradiation from the star, to sustain the radiative-convective profile. The minimum of the energy-limited rate and the mass-loss rate at the Bondi radius determines the rate at which atmospheric loss proceeds as it can be limited by the energy available for cooling or the escape rate of gas molecules from the Bondi radius.

Parameter	Value/Range (initial)
Orbital period (P)	[1, 100] days
Core radius (R_c)	[0.7, 4] $R_\oplus$
Core molecular mass (μ_c)	56 amu
Core adiabatic index (γ_c)	4/3
Core characteristic density (ρ_{c*})	$\rho_\oplus \sim 5.5$ g cm^{-3}
Atmosphere molecular mass (μ)	2 amu
Atmosphere adiabatic index (γ)	7/5
Host star	$\sim$ Sun
Integration time-step	$10^{-2} \times \min\{t_{cool}, t_{loss}\}$
Total evolution time	3 Gyrs.
Number of planets	1 million

Table 2.1: Planet population and evolution parameters for our 'reference' case.

2.2.3 Modeling the Exoplanet Population

Similar to previous works (Owen & Wu, 2017; Ginzburg et al., 2018), we adopt the following period and mass distribution when modeling the exoplanet population:

$$\frac{\mathrm{d}N}{\mathrm{d}\log P} \propto \begin{cases} P^2, & P < 8 \text{ days} \\ \text{constant}, & P > 8 \text{ days, and} \end{cases} \tag{2.9}$$

$$\frac{\mathrm{d}N}{\mathrm{d}M_c} \propto \begin{cases} M_c \exp\left(-M_c^2/(2\sigma_M^2)\right), & M_c < 5\ M_\oplus \\ M_c^{-2}, & M_c > 5\ M_\oplus. \end{cases} \tag{2.10}$$

The planet mass distribution is described by a Rayleigh distribution with for planets less massive than $5M_\oplus$ and as an inverse square tail for the planets more massive than $5M_\oplus$. We use $\sigma_M = 2.7M_\oplus$ throughout this paper, unless stated otherwise. We note here that Ginzburg et al. (2018) investigated both dN/dM_c = [constant] and dN/dM_c = [Rayleigh distribution] for planets less massive than $5M_\oplus$ and found no significant difference in the resulting 1-D radius distributions. For simplicity, we only investigate the latter in this work which is similar to the planet mass distribution used in published photoevaporation studies (e.g., Owen & Wu, 2017).

For the initial atmosphere to core mass-fraction (f) of the planets, we use

$$f \simeq 0.05(M_c/M_\oplus)^{1/2}, \tag{2.11}$$

which is motivated by a previous work on gas accretion and loss during disk dispersal (Ginzburg et al., 2016).

The results presented in Section 2.3 are based on the evolution of a population of a million planets over a period of 3 Gyrs. The defining parameters for our 'reference' planet population and the numerical calculations for its evolution are summarized in Table 2.1.

The planets in this 'reference' population have rocky Earth-like cores, H_2 atmospheres and Sun-like host stars. Beyond this reference case, we explore a range of core compositions and planet-mass distributions. The choice of parameters for our reference case only differs from Ginzburg et al. (2018) in the explicit use of Equation (2.4) for calculating ΔR instead of assuming the ratio of the core's and atmosphere's heat capacity to be $(17\mathrm{f})^{-1}$.

2.3 Results

In this section, we present the results of our evolution model described in Section 2.2. First we discuss the results for the 'reference' population as defined in Table 2.1 and then investigate the dependence of our findings on core compositions and planet-mass distributions.

2.3.1 Comparing the Core-powered Mass-loss Results with Observations

Ginzburg et al. (2018) already demonstrated that the core-powered mass-loss mechanism itself produces a bimodal exoplanet radius distribution and that it yields results consistent with the observed valley in the radius distribution of close-in super-Earths and sub-Neptunes. Here we extend this comparison from a single histogram of planet radii to a two-dimensional orbital period-planet radius parameter space and use our results to infer properties of the observed exoplanet population.

Figure 2.2 displays our core-powered mass-loss results and compares it with the observations from Fulton et al. (2017) and Fulton & Petigura (2018). The left panel shows the histogram of relative occurrence of planet radii from our model (red) and observations (grey) (Fulton et al., 2017). To facilitate the comparison between our results and obser-

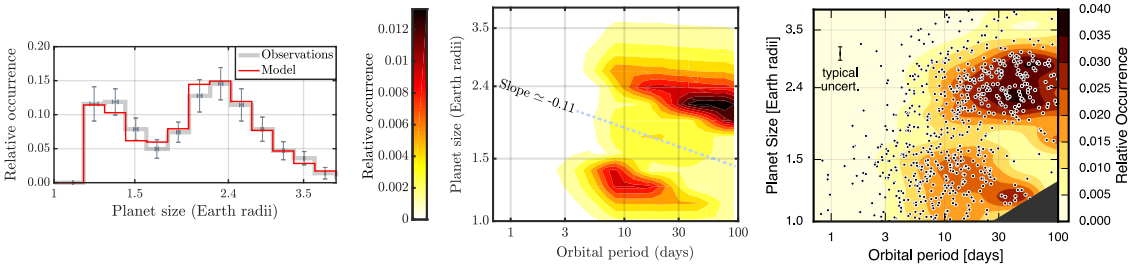

Figure 2.2: Comparing core-powered mass-loss results with observations. *Left panel*: Histogram of planet size (radii). The two histograms correspond to the results from our evolution model for our 'reference' planet population (see Table 1) shown in red and observations shown in gray (Fulton et al., 2017, see Table 3). *Middle and right panels*: Two-dimensional distributions of planet size and orbital period. The middle panel displays the results from our core-powered mass-loss evolution model, while the right panel corresponds to observations (from Fulton & Petigura, 2018, with permission). The dashed blue line in the middle panel corresponds to the center of the valley. Its slope is given by $\mathrm{d}\log R_p/\mathrm{d}\log P \simeq -0.11$. The results from our core-powered mass-loss model are in good agreement with the observations.

vations, we display and normalize our results over the same planet radius range as for the observations shown in Figure 2.2. As shown in previous work (Ginzburg et al., 2018), we find good agreement between the radius distribution produced by the core-powered mass-loss mechanism and the observed exoplanet population. The left panel of Figure 2.2 shows that the valley is located between $\sim$ 1.5-2.0 $R_\oplus$ with a width of $\sim$ 0.5 $R_\oplus$. The lower peak of the 'super-Earths', i.e., planets stripped of their envelopes, is at 1.2-1.4 $R_\oplus$ and the higher peak of the 'sub-Neptunes', i.e., planets that kept most of their atmospheres, is at 2.0-2.7 $R_\oplus$.

The middle panel of Figure 2.2 presents our results in the two-dimensional parameter space of planet size and orbital period. The right panel shows the observational results from Fulton & Petigura (2018) for the same two-dimensional parameter space. We generally find good agreement with observations. Specifically, our results display a valley of approximately constant width that moves to smaller planet radii with increasing orbital period. This is a manifestation of the decreasing susceptibility of planets to lose their atmospheres with increasing orbital period. This results in a negative slope for the valley, which is plotted as a dashed line in the middle panel. We find a slope $\mathrm{d}\log R_p/\mathrm{d}\log P \simeq -0.11$ both analytically and numerically, which is in excellent agreement with observations reported by Van Eylen et al. (2018) and Martinez et al. (2019) who find $\mathrm{d}\log R_p/\mathrm{d}\log P = -0.09^{+0.02}_{-0.04}$ and $\mathrm{d}\log R_p/\mathrm{d}\log P = -0.11^{+0.03}_{-0.03}$, respectively. We discuss the physical processes determining the slope and analytically derive the slope of the valley in Section 2.3.2.

The degree of similarity between observations and the core-powered mass-loss results presented here demonstrates that the core-powered mass-loss mechanism can by itself reproduce the observed valley in the exoplanet radius distribution and this is not unique to photoevaporation (Owen & Wu, 2017). Specifically, Figure 2.2 shows that the core-powered mass-loss mechanism can reproduce the valley in radius-period space, its position,

shape and slope, and the location and magnitude of the peaks of the exoplanet population on either side of the valley.

2.3.2 Slope of the Valley

As discussed in Section 2.2.2, for a planet to lose its envelope it not only has to have enough energy to unbind the atmosphere but it also needs to have enough time for the mass-loss to occur.

2.3.2.1 Mass-loss limited by time, $t_{cool} = t_{loss}$, $P \gtrsim 8$ days

We find that it is the time-limit and not the energy-limit that dictates which planets lose and retain their atmospheres for orbital periods of about 8 days and larger. It is, to first order, the mass-loss timescale, due to its exponential dependence on period and planet size, that creates the valley and determines its slope in the planet radius and orbital period space. Specifically, we find that the criterion $t_{cool} = t_{loss}$ separates the planets that will end up above and below the valley.

Planets accrete their envelopes with $R_{rcb} \sim R_B$ (e.g. Lee & Chiang, 2015; Ginzburg et al., 2016) and then shed their outer layers and shrink in radius during and after the disk dispersal phase (e.g. Owen & Wu, 2016; Ginzburg et al., 2016). This ensures that, from a planet formation point of view, initially all planets start out with $t_{loss} < t_{cool}$, i.e. initially the envelope mass-loss timescale is short because $R_{rcb} \sim R_B$ and hence the exponent in the mass-loss timescale is small. However, as planets initially lose mass, they also shrink, increasing the mass-loss timescale, and in some cases the cooling timescale catches up with the mass loss timescale such that $t_{cool} = t_{loss}$. The criterion $t_{cool} = t_{loss}$ separates the planets that will end up above and below the valley because once planets can cool

faster than they can lose mass (i.e., $t_{cool} < t_{loss}$), they shrink in size and any subsequent mass-loss is hence cut-off rapidly due to the exponential dependence on planet size of the mass-loss timescale (see Section 2.2). Furthermore, due to the exponential dependence of the mass-loss timescale, it is, to first order, the exponent that determines the slope of the valley in the radius-period parameter space. Setting the mass-loss timescale equal to the cooling timescale, we have from Equation (2.6) that $GM_p/c_s^2 R_{rcb} \simeq$ constant and hence

$$\frac{R_c^4 P^{1/3}}{R_p} \rho_{c*}^{4/3} \simeq R_p^3 P^{1/3} \rho_{c*}^{4/3} = \text{constant}, \tag{2.12}$$

where we substituted for the speed of sound and the mass-radius relation of the core and used the fact that $R_{rcb} = R_p \simeq 2R_c$. As long as a planet's core density has no semi-major axis dependence, Equation (2.12) yields $R_p \propto P^{-1/9}$ which corresponds to a slope in the logarithmic parameter space of planet radius and orbital period of

$$\frac{\mathrm{d}\log R_p}{\mathrm{d}\log P} = -\frac{1}{9} \simeq -0.11. \tag{2.13}$$

This is in excellent agreement with the observed slope reported by Van Eylen et al. (2018), $\mathrm{d}\log R_p/\mathrm{d}\log P = -0.09^{+0.02}_{-0.04}$, based on high precision asteroseismic measurements of stellar parameters and results obtained by Martinez et al. (2019) who report a slope of $\mathrm{d}\log R_p/\mathrm{d}\log P = -0.11^{+0.03}_{-0.03}$. The middle panel of Figure 2.2 shows a dashed line denoting the center of the observed valley. The slope of this line, as measured from our numerical simulations, is in full agreement with our analytical estimate above. Equation (2.12) shows that the valley's slope in the radius-period space does, to first order, not depend on f, properties of the host star or the core density as these only change the constant in Equation (2.12) but not the power-law relation between R_p and P. These quantities, do however, change the location of the valley, which is set by the constant in Equation (2.12) and which we will come back to when examining the dependence of our results on the core composition in Section 2.3.3.

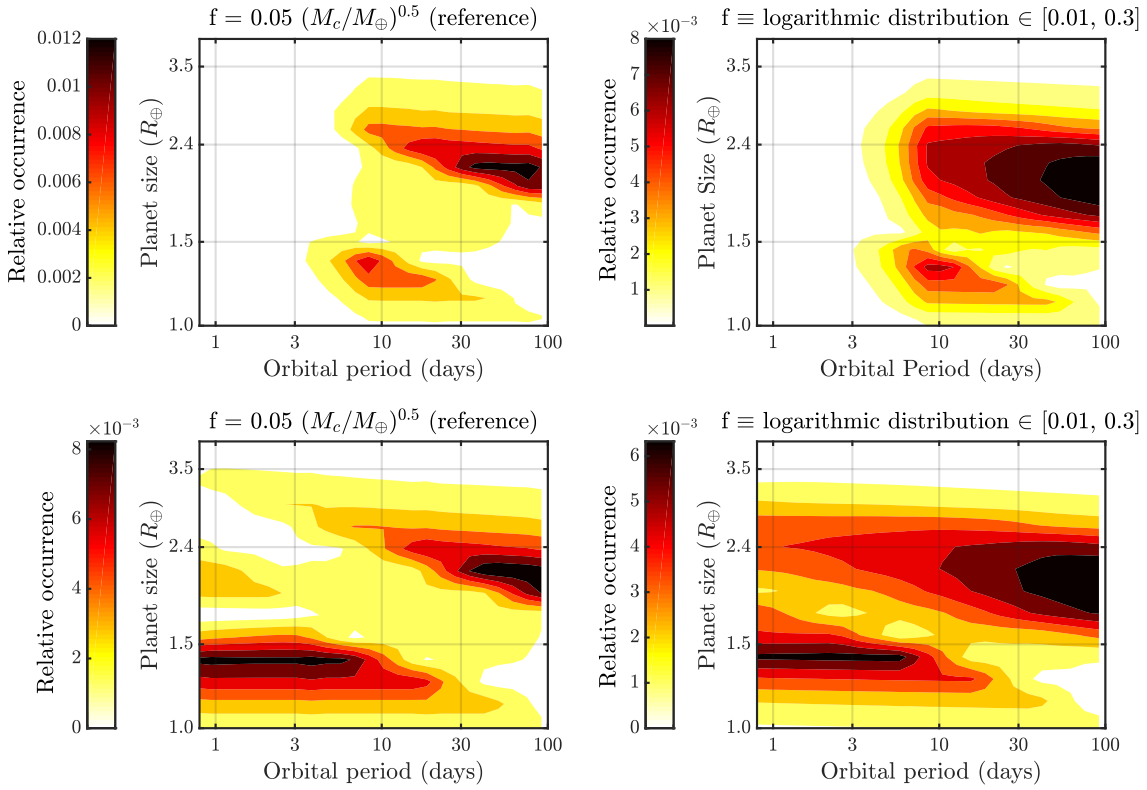

Figure 2.3: Core powered mass-loss results for different distributions of initial envelope fractions, f (*continued next page*).

Figure 2.3: Core powered mass-loss results for different distributions of initial envelope fractions, f. The left column corresponds to envelope fractions distributed according to Equation (2.11) and the right column to the logarithmic distribution used in Owen & Wu (2017). The top panel shows the results weighted by the exoplanet period distribution given by Equation (2.9) and the bottom panel shows, for clarity, the results for a uniform period distribution. For the f distribution used in this work (see Equation (2.11)), the transition between the energy-limited and the time-limited mass-loss regime occurs around 8 days (see flat lower edge of the valley for periods of less than about 8 days in bottom left panel of the figure). If there is no unique relationship between a planet's core mass and its envelope fraction (e.g. in the logarithmic distribution for f used in the right panel), then there is no flat line that sets the lower edge of the radius valley at short orbital periods (see bottom right side of the panel) and there is no single orbital period that marks the transition between the energy-limited and time-limited mass loss regime (see Section 2.3.2.2 for details).

It may at first seem surprising that the slope that is obtained by setting $t_{cool} = t_{loss}$ is not significantly modified over time as the planets continue to thermally evolve and contract. However, we find both analytically and numerically that the contraction rate, for planets that satisfy $t_{cool} = t_{loss}$, only weakly depends on R_c and f for the parameters investigated here. Furthermore, even if a logarithmic distribution of f is assumed, the slope of the valley is, to first order, still well described by setting $t_{cool} = t_{loss}$ as is illustrated by the results shown in Figure 2.3. The logarithmic f distribution does change the shape of the valley somewhat, especially the upper edge which is due to the fact that, for a logarithmic f distribution, the evolution rates start to differ significantly for a given planet mass.

The one quantity that does change the slope of the valley is the mass-radius relationship of the core. Specifically, we find from Equations (2.6) and (2.12) that

$$\frac{\mathrm{d}\log R_p}{\mathrm{d}\log P} \simeq \frac{1}{3(1-\beta)}, \text{ where } M_c \propto R_c^{\beta}. \tag{2.14}$$

Precise observational measurements of the valley's slope are therefore able to determine the exoplanet mass-radius relation of the core. We find that published measurements of the slope (Van Eylen et al., 2018) are in agreement with $M_c/M_\oplus \propto (R_c/R_\oplus)^4$ but inconsistent with $M_c/M_\oplus \propto (R_c/R_\oplus)^3$, highlighting the significance of internal compression of massive cores.

2.3.2.2 Mass-loss limited by energy, $E_{cool} = E_{loss}$, $P \lesssim 8$days

As shown in Section 2.2.2, whether a planet has enough energy to lose its envelope is solely dictated by the envelope to core mass-fraction, f. If f has, to first order, no dependence on the distance from the host star, as we assume in Equation (2.11), then the maximum envelope fraction for which significant atmospheric loss can occur corresponds to a single planet mass independent of period provided that there is a unique relationship between f and the

core mass (as, for example, given in Equation (2.11) and predicted by planet formation models of atmospheric accretion of super-Earths and sub-Neptunes (Lee & Chiang, 2015; Ginzburg et al., 2016)). Evaluating $E_{loss} = E_{cool}$ and accounting for all the γ dependencies yields $M_{atm}/M_c \simeq 14\%$ for $\gamma = 7/5$. This implies that planets with $f \lesssim 14\%$ have enough energy available from cooling that they can unbind their H/He envelopes. This envelope fraction can be converted into a core mass and radius using Equation (2.11) which yields $M_c \simeq 8M_\oplus$ and $R_c \simeq 1.7R_\oplus$, respectively. We therefore expect a single flat line for the lower edge of the valley corresponding to $R_c \simeq 1.7R_\oplus$ for planets whose atmospheric loss is energy and not time-limited, which corresponds to planets with orbital periods of less than about 8 days (see the left panel in Figure 2.3).

We note here, that if there is no unique relationship between a planet's core mass and its envelope fraction, like, for example, in the logarithmic distribution for f used in Owen & Wu (2017), then the critical atmosphere to core mass ratio, for which significant atmospheric loss will occur in the energy-limited regime, cannot be converted to a single core mass and radius. Hence, in this case, there is no flat line that sets the lower edge of the radius valley and there is no single orbital period at which the transition from energy-limited to time-limited atmospheric loss occurs (see the right panel in Figure 2.3).

For the parameters used in this work, the transition between the energy-limited and time-limited mass-loss occurs around 8 days, but the exact transition in period space depends on the relationship between f and the core mass (see Figure 2.3 and Equation (2.11)). This implies that if the lower edge of the radius valley is observed to be a flat line for planets inside orbital periods of several days than this can be used to constrain the initial envelope fractions from planet formation and hence the atmospheric accretion process itself.

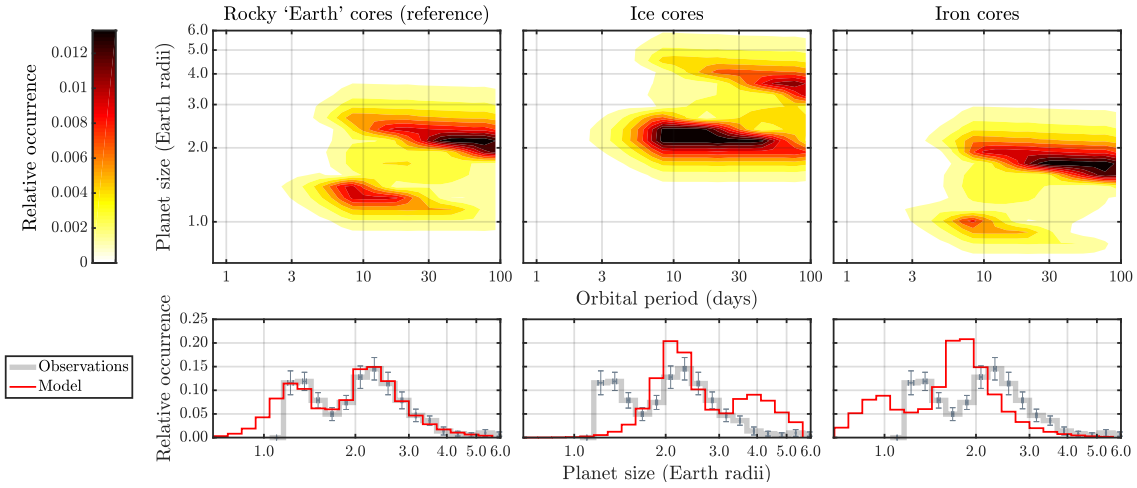

Figure 2.4: Dependence of the core-powered mass-loss results on core composition. This figure displays two-dimensional distributions of planet size and orbital period in the top row, and histograms of planet size in the bottom row. The three columns correspond to three different core materials, namely (from left to right), rocky 'Earth' like (reference case; $\mu_c = 56\ amu,\ \rho_{c*} = 5.5$ g cm^{-3}), ice ($\mu_c = 18\ amu,\ \rho_{c*} = 1.3$ g cm^{-3}) and iron ($\mu_c = 56\ amu,\ \rho_{c*} = 11$ g cm^{-3}). While the case with rocky cores closely resembles the observations (see Figure 2.2), for icy and iron cores the valley shifts to higher and lower planet sizes, respectively. To aid the comparison between our results and observations, we normalized our findings over the same planet radius range as the observations, but display our numerical results down to planet sizes that are smaller than the smallest observed radius bin in Fulton et al. (2017).

2.3.3 Constraints on the Core Composition

We investigate the dependence of our results on composition of the exoplanet cores. We account for changes in core material by modifying the core density (ρ_{c*}) and its molecular mass (μ_c).

2.3.3.1 Single Composition Cores

As we can see from Equation (2.12), the slope of the valley should be insensitive to changes in core density, ρ_{c*}, but its location should scale as $\rho_{c*}^{-4/9}$, or more generally as $\rho_{c*}^{-\beta/9}$, where β is the exponent in the mass-radius relation of the core. We therefore expect the slope to remain the same but the location of the valley to move to larger planet radii for lower density cores and to smaller planet radii for high density cores. This is exactly what we find numerically in our results shown in Figure 2.4 for cores made of ice and iron. From the scaling with core composition above, we predict that the bottom of the valley should move up by a factor of 1.9 from about $1.6R_p$ to about $3.0R_p$ for icy core and move down by a factor of 0.7 for iron cores from about $1.6R_p$ to about $1.1R_p$ compared to our rocky 'reference' case, which is indeed what is shown in Figure 2.4. Another implication of the exponential dependence on core density is that the characteristics of the final radius distribution are, to first order, not affected by the changes in μ_c.

Finally, our numerical results in Figure 2.4 confirm that, while there are significant changes in the location of the valley for the different core compositions, the slope of the valley remains essentially unchanged, as expected.

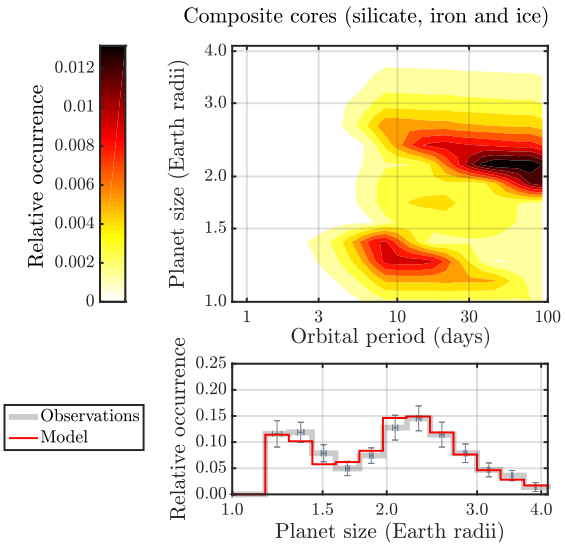

Figure 2.5: Maximum water-ice content for Earth-like cores. This figure shows a two-dimensional distribution of planet size and orbital period in the top panel and histogram of planet size in the bottom panel. The cores of the planet population have the following composition: 56% silicate (μ_c = 76 amu, ρ_{c*} = 4 g cm^{-3}), 28% iron (μ_c = 56 amu, ρ_{c*} = 11 g cm^{-3}) and 16% ice (μ_c = 18 amu, ρ_{c*} = 1.3 g cm^{-3}) with an effective μ_c = 61 amu and $\rho_{c*} \simeq 5.5$ g cm^{-3}. Earth-like composition cores can contain up to $\sim$ 20% of water-ice and still match the observations.

2.3.3.2 Maximum Water/Ice Content of Super-Earths and Sub-Neptune Cores

The strong dependence of the valley's location on the density of planetary cores implies that we can, not only constrain the bulk composition of the cores of super-Earths and sub-Neptunes, but that we can also place limits on their maximum water/ice content. We demonstrate this in an example in which we assume a core composition that initially consists of $1/3$ iron ($\rho_{c*} = 11$ g cm^{-3}) and $2/3$ silicate ($\rho_{c*} = 4$ g cm^{-3}) by mass, and then add the maximum amount of water-ice ($\rho_{c*} = 1.3$ g cm^{-3}) that can reproduce the observations. Figure 2.5 shows that 16% of water-ice can be added to Earth-like composition cores without causing a noticeable discrepancy between our core-powered mass-loss results and the observations. This implies that, first, the location of the valley constrains the bulk density of the super-Earth and sub-Neptune population and, second, this in turn can be used to place limits on their possible compositions. Overall we find, similar to photoevaporation studies (e.g., Owen & Wu, 2017; Jin & Mordasini, 2018), that cores must be predominantly rocky with water-ice fractions of less than $\sim 20\%$.

In addition, we can conclude from the location of the valley and the peaks for the different core compositions in Figure 2.4 that the fraction of pure water/ice worlds and pure iron cores must be relatively small.

These inferences imply that most of the close-in super-Earths and sub-Neptunes formed in a water/ice poor environment.

2.3.4 Dependence on Planet-mass Distribution

We also investigate the sensitivity of our results to the underlying distribution of planet masses ($M_p \simeq M_c$). Specifically, we keep the Rayleigh distribution and the inverse-square tail, but change the value of σ_M; see Equation (2.10). Figure 2.6 displays our 'reference'

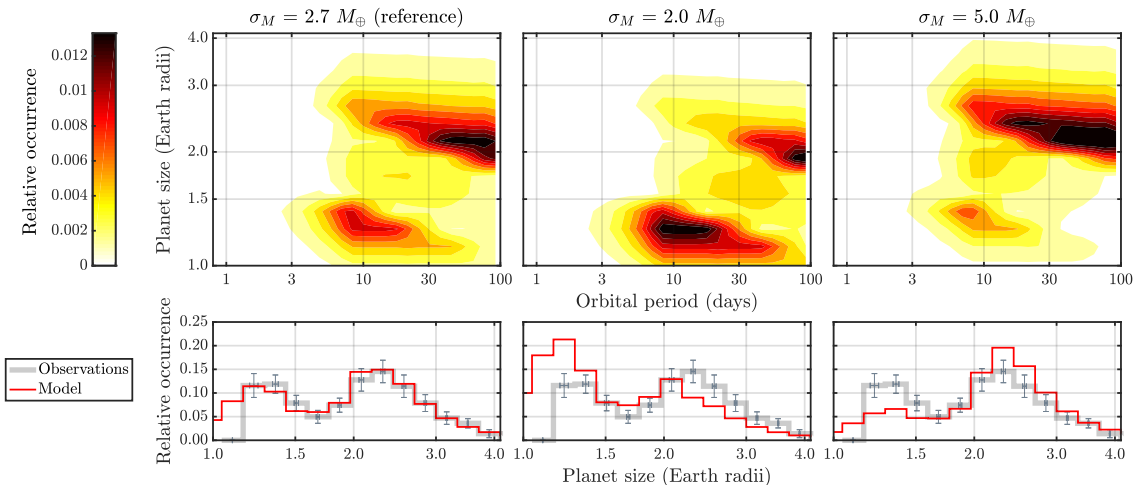

Figure 2.6: Dependence of the core-powered mass-loss results on planet-mass distribution. Figure shows two-dimensional distributions of planet size and orbital period in the top row, and histograms of planet size in the bottom row. The three columns correspond to three different planet-mass distributions modeled as a Rayleigh distribution with an inverse-square tail, with σ_M values of 2.7 $M_\oplus$ (reference case, left panel), 2.0 $M_\oplus$ (middle panel) and 5.0 $M_\oplus$ (right panel), see Equation (2.10) for details. As, expected, for a lower σ_M, the occurrence of planets below the valley is larger than in the 'reference' case. In contrast, the peak above the valley is more pronounced for the higher σ_M value than in the 'reference' case. To aid the comparison between our results and observations, we normalized our findings over the same planet radius range as the observations, but display our numerical results down to planet sizes that are smaller than the smallest observed radius bin in Fulton et al. (2017).

case (left panel) and results for $\sigma_M = 2.0 M_\oplus$ and $\sigma_M = 5.0 M_\oplus$ in the middle and right panel, respectively. Figure 2.6 shows that for a lower σ_M, i.e., for an underlying distribution peaking at a lower planet mass, the peak below the valley is more significant than in the 'reference' case. In contrast, for higher values of σ_M the peak above the valley is more pronounced. However, any changes in the mass distribution do not fundamentally change the location of the valley itself. This implies that the location of the valley does not depend on the detailed assumptions of the planet-mass distribution (as long as it is chosen to cover the observed parameter space in planet radii/masses), but is determined by the planet's core composition instead (see Figure 2.4 and discussion in Section 2.3.3). In contrast, the relative magnitude of the peaks above and below the valley is sensitive to the details of the underlying planet-mass distribution and it can hence be used to constrain the planet population from observations. Similar to previous studies, we find a Rayleigh distribution with an inverse-square tail, with $\sigma_M \sim 3.0 M_\oplus$, yields a good fit to the observations; see Figure 2.2 and Figure 2.6.

2.4 Discussion & Conclusions

Close-in exoplanets display an intriguing gap in their radius distribution around 1.5-2.0 Earth radii (Owen & Wu, 2013; Fulton et al., 2017; Fulton & Petigura, 2018; Van Eylen et al., 2018).

In this work, we numerically followed the thermal evolution and atmospheric loss of small, short-period planets modeled on the observed exoplanet population. To distinguish our results from any atmospheric loss due to photoevaporation, we only considered the planet's evolution due to its own cooling luminosity and its subsequent mass-loss, i.e., we focus on the planet's evolution due to the core-powered mass-loss mechanism (Ginzburg

et al., 2016, 2018).

We demonstrated that planetary evolution based on the core-powered mass-loss mechanism alone (i.e., without any photoevaporation) is capable of reproducing the observed valley in the radius distribution of small, close-in planets. In particular, we are able to match the valley's position, shape, slope and the relative magnitude of the peaks above and below the valley. Our results are in good agreement with observations both when examining the histogram of planet sizes and the two-dimensional planet size-orbital period parameter space. Our findings imply that even super-Earths that appear as barren rocky cores today likely formed with primordial hydrogen and helium envelopes and that they are therefore not true terrestrial planet analogs from the point of view of their formation.

We analytically derive the slope of the valley by equating the atmospheric mass-loss timescale to the cooling timescale and find a slope for the valley $\mathrm{d}\log R_p/\mathrm{d}\log P \simeq -0.11$. This is identical to the slope that we find from our numerical evolution models and is in good agreement with the value reported by Van Eylen et al. (2018), $-0.09^{+0.02}_{-0.04}$ and Martinez et al. (2019), $-0.11^{+0.03}_{-0.03}$.

We find, both numerically and analytically, that the slope of the valley is, to first order, independent of the core density and planet-mass distribution, but that it does depend on the mass-radius relation of the core. Precise observational measurements of the valley's slope should therefore probe the exoplanet mass-radius relation of the core. We find that published measurements of the slope are in agreement with $M_c/M_\oplus \propto (R_c/R_\oplus)^4$ but inconsistent with $M_c/M_\oplus \propto (R_c/R_\oplus)^3$, highlighting the significance of internal compression of massive cores.

In addition to understanding the formation of the valley itself, we investigated the dependence of our results on core composition and planet-mass distribution, and compared

our findings with observations from recent exoplanet studies (Fulton et al., 2017; Fulton & Petigura, 2018; Van Eylen et al., 2018).

By varying the density and mean molecular mass of the cores, we demonstrated analytically and numerically that the location of the valley depends primarily on the core's density and that it shifts to larger (smaller) planetary radii for lower (higher) density cores. This implies that the location of the valley constrains, to first order, the bulk density of the cores of the super-Earth and sub-Neptune population. We find that cores must be predominantly rocky with typical water-ice fractions of less than $\sim 20\%$ to match observations. In addition, we conclude from the location of the valley and the peaks for the different core compositions that the fraction of water worlds and iron cores must be relatively small. These inferences imply that most of the close-in super-Earths and sub-Neptunes accreted predominantly inside the ice line.

We also investigated the sensitivity of our results to the underlying distribution of planet masses and discovered that the location of the valley does not depend on the detailed assumptions of the planet-mass distribution (as long as it is chosen to cover the observed parameter space in planet radii/masses). In contrast, the relative magnitude of the peaks above and below the valley is sensitive to the details of the planet-mass distribution and it can hence be used to constrain the planet population from observations. Similar to previous studies, we find that the planet-mass distribution modeled as a Rayleigh distribution with an inverse-square tail, with $\sigma_M \sim 3.0 M_\oplus$, can closely reproduce observations (e.g. Fulton et al., 2017; Fulton & Petigura, 2018; Van Eylen et al., 2018).

Throughout this work, we use $\gamma = 7/5$ which corresponds to molecular gas. However, temperatures deep inside the envelope, especially early on, can be hot enough for hydrogen to exist as monatomic gas for which $\gamma = 5/3$ and the dissociation of hydrogen in the

atmosphere even allows for the possibility of values of $\gamma < 4/3$. Although we chose to model our atmospheres with $\gamma = 7/5$ the results presented in this work are general and do not depend on the exact value of γ used. The main way in which the exact choice of γ matters is that it determines how the mass and energy is distributed in the atmosphere. However, because we are investigating planets after the spontaneous mass-loss/boil-off phase, the radius of the atmosphere, given by R_{rcb}, varies only between one and and a few R_c which implies that the actual variations between the monatomic and diatomic case for the mass distribution in the atmosphere are rather small. In addition, since the exponent given in Equation 2.12 that determines the slope of the valley does not depend on γ, the slope of the radius valley is the same regardless of the value of γ used. Possibly, the most interesting difference between the monatomic and diatomic case relevant for this work is the envelope-to-core-mass ratio for which $E_{loss} \simeq E_{cool}$ (see Sections 2.2.1 and 2.2.2 for details). However, even in this case the difference is small. Evaluating $E_{loss} = E_{cool}$ accounting for all the γ dependencies yields $M_{atm}/M_c \simeq 14\%$ and $M_{atm}/M_c \simeq 15\%$, for $\gamma = 7/5$ and $\gamma = 5/3$, respectively. These envelope fractions can be converted into core radii using Equation 2.1 which yields $R_c \simeq 1.7R_\oplus$ for both cases. Finally, the evolution timescales are longer by a factor of several for $\gamma = 5/3$. However, this longer evolution timescale would have the most significant effect on Gyr timescales by which time most planets will have cooled sufficiently such that the $\gamma = 7/5$ case investigated here likely provides a better description of their envelopes than the $\gamma = 5/3$.

In this study, we demonstrate that a planet's own cooling luminosity is capable of reproducing the observed valley in the radius distribution of close-in planets. Although atmospheric loss by the core-powered mass-loss mechanism seems an inevitable by-product of atmospheric accretion and the planet formation process itself, our results should not be taken to imply that atmospheric loss by photoevaporation does not happen or that it has

to be unimportant. In fact, it seems likely that both processes contributed to sculpting the observed exoplanet population. Our work demonstrates that the core-powered mass-loss mechanism (Ginzburg et al., 2016, 2018) yields similar results to the photoevaporation mechanism (Owen & Wu, 2017) in terms of the existence, location and slope of the radius valley, core composition, and the core mass distribution. This implies that, regardless of which of the two mechanism dominates (if any), the conclusions concerning, for example, the core composition and the implications that most super-Earths and sub-Neptunes are water-ice poor, are independent of the mass-loss mechanism.

In future work, we plan to combine photoevaporation with the core-powered mass-loss mechanism, and to extend the current investigation to a range of stellar types with the hope to be able to disentangle the specific signatures that these two mechanisms leave in the observed exoplanet population. This work will also address whether the core-powered mass-loss mechanism supports claims from photo-evaporation models that the planet-mass distribution varies with stellar mass (Wu, 2019) and it will examine the radius valley's dependence on metallicity (Owen & Murray-Clay, 2018).

CHAPTER 3

Signatures of the Core-Powered Mass-Loss Mechanism in the Exoplanet Population: Dependence on Stellar Properties and Observational Predictions

[1]Recent studies have shown that atmospheric mass-loss powered by the cooling luminosity of a planet's core can explain the observed radius valley separating super-Earths and sub-Neptunes, even without photoevaporation. In this work, we investigate the dependence of this core-powered mass-loss mechanism on stellar mass (M_*), metallicity (Z_*) and age (τ_*). Without making any changes to the underlying planet population, we find that the core-powered mass-loss model yields a shift in the radius valley to larger planet sizes around more massive stars with a slope given by $\mathrm{d}\log R_p/\mathrm{d}\log M_* \simeq 0.35$, in agreement with observations. To first order, this slope is driven by the dependence of core-powered mass-loss on the bolometric luminosity of the host star and is given by $\mathrm{d}\log R_p/\mathrm{d}\log M_* \simeq (3\alpha - 2)/36 \simeq 0.33$, where $(L_*/L_\odot) = (M_*/M_\odot)^\alpha$ is the stellar mass-luminosity relation and $\alpha \simeq 4.6$ for the CKS dataset. We therefore find, in contrast to photoevaporation models, no evidence for a linear correlation between planet and stellar mass, but can't rule it out either. In addition, we show that the location of the radius valley is, to first

[1]This chapter was previously published in similar form as Gupta, A. and Schlichting, H. E. 2020, MNRAS 493, 792-806.

order, independent of stellar age and metallicity. Since core-powered mass-loss proceeds over Gyr timescales, the abundance of super-Earths relative to sub-Neptunes increases with age but decreases with stellar metallicity. Finally, due to the dependence of the envelope's cooling timescale on metallicity, we find that the radii of sub-Neptunes increase with metallicity and decrease with age with slopes given by $\mathrm{d}\log R_p/\mathrm{d}\log Z_* \simeq 0.1$ and $\mathrm{d}\log R_p/\mathrm{d}\log \tau_* \simeq -0.1$, respectively. We conclude with a series of observational tests that can differentiate between core-powered mass-loss and photoevaporation models.

3.1 Introduction

In the last decade, NASA's *Kepler* mission has revolutionized the field of exoplanets by discovering more than 4000 planetary candidates (e.g., Borucki et al., 2010). These discoveries offer new insights into the formation and evolution of planets. One of *Kepler*'s key findings is that the most common planets, observed to date, are one to four Earth radii ($R_\oplus$) in size (e.g., Fressin et al., 2013; Petigura et al., 2013). In addition, transit-timing variations (e.g., Carter et al., 2012; Hadden & Lithwick, 2017) and follow-up radial velocity (e.g., Marcy et al., 2014b; Weiss & Marcy, 2014) measurements have revealed that planets smaller than about 1.6 $R_\oplus$ have higher densities suggesting rocky 'Earth-like' compositions while larger planets have lower densities consistent with significant H/He envelopes (e.g., Marcy et al., 2014a; Rogers, 2015). Intriguingly, analyses of early photometry data from the *Kepler* Input Catalog (e.g., Brown et al., 2011), the recent spectroscopic follow-up of planet-hosting stars by the California-*Kepler* Survey (CKS; Petigura et al., 2017; Johnson et al., 2017), and the latest studies incorporating *Gaia* astrometry and asteroseismology-based data have all revealed a 'radius valley' in the distribution of these small, close-in (orbital period $<$ 100 days) exoplanets (e.g., Owen & Wu, 2013; Lopez & Fortney, 2013;

Fulton et al., 2017; Fulton & Petigura, 2018; Van Eylen et al., 2018; Berger et al., 2018; Martinez et al., 2019).

This radius valley marks the transition from a population of small, rocky 'super-Earths' to a population of large 'sub-Neptunes' with significant H/He envelopes (e.g., Owen & Wu, 2013; Lopez & Fortney, 2013; Rogers, 2015; Ginzburg et al., 2016). Furthermore, studies involving *Gaia* astrometry (Martinez et al., 2019) and asteroseismology-based (Van Eylen et al., 2018) high-precision measurements of stellar parameters have measured the slope of the radius valley and obtained values of $\mathrm{d}\log R_p/\mathrm{d}\log P = -0.11^{+0.03}_{-0.03}$ and $-0.09^{+0.04}_{-0.02}$, respectively.

The bimodality in the radius distribution has been attributed to photoevaporation of H/He envelopes by high-energy radiation (e.g., XUV) from the host stars (e.g., Owen & Wu, 2013; Lopez & Fortney, 2013; Jin et al., 2014; Chen & Rogers, 2016; Owen & Wu, 2017; Jin & Mordasini, 2018). Under this mechanism, close-in planets can receive, over a lifetime, a total time-integrated high-energy flux comparable to their atmosphere's binding energy and are thus able to lose their atmospheres (e.g., Owen & Wu, 2017). Studies have demonstrated that planetary evolution with photoevaporation can reproduce the radius valley. In addition, these studies infer 'Earth-like' bulk composition of the planetary cores implying a low overall water-fraction (e.g., Owen & Wu, 2017; Jin & Mordasini, 2018; Wu, 2019).

Recently, Ginzburg et al. (2018) and Gupta & Schlichting (2019) showed that the core-powered mass-loss mechanism is also able to reproduce the observed radius valley, even in the absence of photoevaporation. In this mechanism, a planet's internal luminosity drives the loss of its atmosphere (Ginzburg et al., 2016, 2018; Gupta & Schlichting, 2019). The source of this luminosity is a planet's primordial energy from formation, which can be

of the order of, or even larger than, its atmosphere's gravitational binding energy. Gupta & Schlichting (2019) showed that evolution of planets under the core-powered mass-loss mechanism around 'Sun-like' host stars , i.e. stars with solar mass and metallicity and an age of 3 Gyrs, successfully reproduces the location, shape and slope of the radius valley as a function of orbital period. They also demonstrated that the exact location of the radius valley depends on the bulk composition of the planetary cores whereas the relative abundance of super-Earths and sub-Neptunes depends on the underlying planet mass distribution. Similar to photoevaporation studies, Gupta & Schlichting (2019) found that the observations are consistent with 'Earth-like' cores with a maximum water-fraction of ∼20%.

New observations provide us with the opportunity to characterize the super-Earth and sub-Neptune populations as a function of their host star properties (e.g., Fulton & Petigura, 2018; Petigura et al., 2018; Dong et al., 2018). This opens new avenues to investigate and contrast possible signatures the core-powered mass-loss mechanism and photoevaporation imprint on the exoplanet population (e.g., Owen & Murray-Clay, 2018; Wu, 2019).

Fulton & Petigura (2018) and Wu (2019) have found that the radius valley increases in planet size with stellar mass. Moreover, Fulton & Petigura (2018) found that the planet size distribution also shifts to higher insolation flux with increasing stellar mass.

In addition, Petigura et al. (2018) have reported that the relative occurrence of sub-Neptunes increases with increasing stellar metallicity while the relative occurrence of super-Earths remains largely unchanged; see also Dong et al. (2018). Furthermore, Dong et al. (2018) and Owen & Murray-Clay (2018) have reported that sub-Neptunes are larger around higher metallicity FGK stars; see also Petigura et al. (2018). Hirano et al. (2018) reported a similar trend in the distribution of planet sizes around M-dwarfs.

Furthermore, studies based on the Zodiacal Exoplanets in Time (ZEIT) survey have reported a trend in planet size with stellar age (e.g., Mann et al., 2016; Rizzuto et al., 2018). Most *Kepler* planets are older than a Gyr and have significant uncertainties in their age estimates. This makes it difficult to investigate any trends in planet size with stellar age. However, observations from the *K2* mission have allowed the discovery of planets in young clusters like Praesepe and Hyades, both of which are about 650 million years old (e.g., Mann et al., 2016; Rizzuto et al., 2018). The number of planets observed in such clusters is still below ten and thus not statistically significant, nevertheless, these younger planets are bigger, on average, than their older *Kepler* counterparts; see Figure 12 in Rizzuto et al. (2018).

In this study, we extend previous work on the core-powered mass-loss mechanism (Ginzburg et al., 2018; Gupta & Schlichting, 2019), and investigate how stellar mass, metallicity and age impact the resulting planet size distribution. We model our host star population on the stars in the CKS survey and investigate, collectively and in isolation, the impact of stellar mass, metallicity and age on the resulting exoplanet size distribution. We show that core-powered mass-loss can explain many of the observational trends with stellar properties discussed above. In addition, we quantify how different stellar properties shape the observed planet size distribution. In contrast to photoevaporation models, we find no evidence for a linear correlation between planet and stellar mass but can't rule it out either. We show that in the core-powered mass-loss model the observed dependence of the radius valley on stellar mass is, to first order, driven by the stellar mass-luminosity relation.

This paper is structured as follows: In Section 3.2, we describe the core-powered mass-loss mechanism and discuss our model for planetary structure and composition. We then explain, in Section 3.3, how we model the exoplanet and stellar populations. The numerical and analytical core-powered mass-loss results are divided into two sections. In

Section 3.4, we present a comparison of our results with the current exoplanet observations. Complementing this, in Section 3.5, we show how the core-powered mass-loss mechanism depends on individual stellar parameters, make predictions for trends with stellar mass, metallicity and age and investigate if there is any correlation between planet and stellar mass. Finally, we summarize our results in Section 3.6 and present observational tests for distinguishing between the signatures of core-powered mass-loss and photoevaporation.

3.2 Planet Structure and Evolution under the Core-Powered Mass-Loss Mechanism

To study the imprint of the core-powered mass-loss mechanism on the exoplanet population, we solely focus on core-powered mass neglecting mass-loss due to photoevaporation and other mechanisms. For a detailed review of this mechanism, we refer the reader to Ginzburg et al. (2016) and for its dependence on planetary properties, to Gupta & Schlichting (2019).

As a planetary core grows by accreting solids, gravitational binding energy is converted into heat. This thermal energy can be efficiently radiated away if the core forms in isolation. However, if this accretion occurs in the presence of a gas disk, then the core will start accreting a H/He envelope from the surrounding nebula once its Bondi radius is larger than its physical radius. The presence of an optically thick envelope acts as a 'thermal blanket' since, from this point onward, the core's heat loss is limited by the thermal diffusion across the radiative-convective boundary of the envelope (e.g., Rafikov, 2006; Lee & Chiang, 2015; Ginzburg et al., 2016), significantly reducing the cooling rate of the underlying core. As a result, the core temperature is essentially set by the maximum temperature that permits the accretion of a H/He envelope and is roughly given by $T_c \sim GM_c\mu/k_B R_c$,

where μ is the mean molecular mass of the atmosphere, k_B is the Boltzmann constant, G is the gravitational constant and M_c and R_c are the mass and radius of the planetary core, respectively. This implies typical core temperatures of 10^4 - 10^5 K for core masses ranging from the mass of Earth to Neptune. It is this primordial energy from planet formation that drives atmospheric loss in the core-powered mass-loss mechanism which proceeds over Gyr timescales.

As the protoplanetary disk disperses, it causes a loss of pressure support on the outside of the planet's atmosphere. As a consequence, the planet experiences 'spontaneous' atmospheric mass-loss driven by the luminosity of the inner regions of its atmosphere (Ginzburg et al., 2016; Owen & Wu, 2016). Due to this atmospheric mass-loss, the atmosphere rapidly shrinks to a few times the planet's core radius over the disk dispersal timescale. This sets the initial condition for planetary evolution under the core-powered mass-loss and photoevaporation (Owen & Wu, 2017) mechanisms.

At this stage, we assume that a typical planet with radius R_p and mass M_p has a dense core of radius R_c and mass M_c, and a surrounding gaseous atmosphere of mass M_{atm}. We define the core as the non-gaseous part of the planet which dominates the planet's mass such that $M_c \sim M_p$. We account for gravitational compression by assuming that the mass-radius relation of the core is given by $M_c/M_\oplus = (R_c/R_\oplus)^4(\rho_{c*}/\rho_\oplus)^{4/3}$, where ρ_{c*} is the density of the core scaled to an Earth mass and $\oplus$ refers to the corresponding Earth values (Valencia et al., 2006; Fortney et al., 2007). Motivated by direct observational measurements of super-Earth masses and radii (see Figure 10 from Bower et al., 2019) and core-powered mass-loss results from Gupta & Schlichting (2019), we assume throughout this paper a density of $\rho_{c*} = 5.0$ g cm^{-3} for the cores, when scaled to an Earth mass; see also Dorn et al. (2019); Dressing et al. (2015). This density estimate is 10% lower than that used by Gupta & Schlichting (2019) but is in better agreement with the radius distribution

observations from Fulton et al. (2017) when considering a distribution of planet host stars modelled after the CKS dataset (Johnson et al., 2017; Fulton et al., 2017, see Section 3.3.2 for more details). In addition, we assume that the core is molten and fully convective, and that the core-envelope interface is well-coupled.

Following previous work on gas accretion and loss during disk dispersal (Ginzburg et al., 2016), we model all planets with an initial atmosphere to core mass-fraction (f) given by

$$f \simeq 0.05(M_c/M_\oplus)^{1/2}. \tag{3.1}$$

We assume that all planets have initial H_2 envelopes and that they can be described as a diatomic ideal gas with $\gamma = 7/5$ and $\mu = 2$ amu. Although the initial atmosphere to core mass-fraction is only a few percent, the presence of the atmosphere significantly increases the size of the planet. Following past works (e.g., Piso & Youdin, 2014; Lee & Chiang, 2015; Inamdar & Schlichting, 2015), we assume that the atmosphere is structured such that it has an inner convective and outer isothermal region. The convective region is modeled to be adiabatic and contains most of the atmospheric mass while the radiative region is close to isothermal. The atmosphere transitions from the convective to radiative region at the radiative-convective boundary, R_{rcb}. We assume that the planet size is given by the radiative-convective boundary, i.e., $R_p \sim R_{rcb}$, since the atmospheric density decreases exponentially outside the R_{rcb}. In other words, we assume that the atmospheric thickness is $\Delta R \sim R_{rcb} - R_c$, where ΔR initially is a few R_c.

The aforementioned model yields an atmospheric mass of

$$M_{atm} = \frac{\gamma - 1}{\gamma} 4\pi R_c^2 \rho_{rcb} \Delta R \left(\frac{R'_B \Delta R}{R_c^2} \right)^{1/(\gamma-1)}. \tag{3.2}$$

Here γ is the ratio of heat capacities for the atmosphere, ρ_{rcb} is the density of the atmosphere

at the R_{rcb} and R'_B is the modified Bondi radius, such that

$$R'_B \equiv \frac{\gamma - 1}{\gamma} \frac{G M_c \mu}{k_B T_{rcb}}, \tag{3.3}$$

where T_{rcb} is the temperature at the R_{rcb}. T_{rcb} is approximately the planetary equilibrium temperature, $T_{\rm eq}$, for a given distance from the host star which can written as

$$T_{\rm eq} = \left(\frac{1}{16\pi\sigma} \frac{L_*}{a^2} \right)^{1/4}, \tag{3.4}$$

where σ is the Stefan-Boltzmann constant, a is the planet's semi-major axis and L_* is the luminosity of the host star. To facilitate direct comparison with observations, we present some of our results as a function of stellar insolation flux, S, which is related to the equilibrium temperature by $S/S_\oplus = (T_{\rm eq}/T_{eq,\oplus})^4$.

The total energy available for cooling (E_{cool}) is the sum of the thermal energy in the atmosphere and core and the atmosphere's gravitational energy, i.e.

$$E_{cool} \simeq g \Delta R \left(\frac{\gamma}{2\gamma - 1} M_{atm} + \frac{1}{\gamma} \frac{\gamma - 1}{\gamma_c - 1} \frac{\mu}{\mu_c} M_c \right), \tag{3.5}$$

where μ_c and γ_c are the molecular mass and adiabatic index of the core, and $g = G M_c / R_c^2$. Since the core-envelope interface is well coupled, the cooling of both the core and atmosphere is dictated by the radiative diffusion through the radiative-convective boundary, and thus the luminosity of the planet is

$$L = -\frac{{\rm d}E_{cool}}{{\rm d}t} = \frac{64\pi}{3} \frac{\sigma T_{rcb}^4 R'_B}{\kappa \rho_{rcb}}, \tag{3.6}$$

where κ is the opacity at the radiative-convective boundary. We assume that this opacity scales as

$$\frac{\kappa}{0.1 \text{ cm}^2 \text{ g}^{-1}} = \frac{Z_*}{Z_\odot} \left(\frac{\rho_{rcb}}{10^{-3} \text{ g cm}^{-3}} \right)^\beta \tag{3.7}$$

where Z_* is the stellar metallicity, $Z_\odot$ the metallicity of the Sun, β is assumed to be 0.6 throughout this paper (e.g., Lee & Chiang, 2015; Freedman et al., 2008) and any temperature dependence is neglected. We are assuming in Equation 3.7 that the envelope opacity scales linearly with the metallicity of the envelope and that the envelope metallicity can be approximated by the metallicity of the host star such that [Fe/H] $\simeq [Z_*/Z_\odot]$. The assumption that the envelope metallicity scales linearly with the metallicity of the host star is a reasonable first guess, given the absence of direct observational measurements, since more metal-rich stars are expected to have more metal-rich disks which should, in turn, lead to more metal-rich planetary envelopes. Recent observational measurements provide tentative evidence for a correlation between the metallicity of envelope and that of the host star for gas giant exoplanets (e.g., Wallack et al., 2019).

Combining Equations (3.5) and (3.6) yields a planetary cooling timescale given by

$$t_{cool} = \frac{E_{cool}}{|\mathrm{d}E_{cool}/\mathrm{d}t|} = \frac{E_{cool}}{L}. \tag{3.8}$$

There are two regimes of atmospheric mass-loss: energy-limited mass-loss and Bondi-limited mass-loss. The energy-limited mass-loss rate is

$$\dot{M}^E_{atm} \simeq \frac{L(t)}{gR_c}, \tag{3.9}$$

i.e., it is the absolute upper limit on the atmospheric mass-loss rate achievable assuming all the cooling luminosity goes into driving the mass-loss. On the other hand, the Bondi-limited mass-loss rate, $\dot{M}^B_{atm}$, signifies a physical limit on the atmospheric mass-loss rate dictated by the thermal velocity of the gas molecules at the Bondi radius (e.g., Ginzburg et al., 2016; Owen & Wu, 2016). Because the hydrodynamic outflow of the atmosphere has to pass through the sonic point and since the mass flux is conserved, it is convenient to determine the mass-loss rate at the sonic point, $R_s = GM_p/2c_s^2$, where $c_s = (k_B T_{\mathrm{eq}}/\mu)^{1/2}$

is the isothermal speed of sound. In this case, the mass-loss rate is $\dot{M} = 4\pi\rho_s R_s^2 c_s$, where ρ_s is the density at the sonic point. In the limit that $R_s >> R_{rcb}$, ρ_s is related to the density at the radiative-convective boundary by $\rho_s = \rho_{rcb}\exp(-2R_s/R_{rcb})$. The mass-loss rate at the Bondi radius is therefore given by

$$\dot{M}^B_{atm} = 4\pi R_s^2 c_s \rho_{rcb} \exp\left(-\frac{GM_p}{c_s^2 R_{rcb}}\right). \tag{3.10}$$

The actual atmospheric mass-loss rate is the minimum of the energy-limited and Bondi-limited mass-loss rates, i.e., $\dot{M}_{atm} = min\{\dot{M}^E_{atm}, \dot{M}^B_{atm}\}$. Combining Equations (3.2), (3.9) and (3.10) yields an atmospheric mass-loss timescale that can be written as

$$t_{loss} = \frac{M_{atm}}{|\mathrm{d}M_{atm}/\mathrm{d}t|} = max\left\{\frac{M_{atm}}{\dot{M}^E_{atm}}, \frac{M_{atm}}{\dot{M}^B_{atm}}\right\}. \tag{3.11}$$

Planets which eventually become super-Earths have enough energy to lose their atmospheres entirely and have mass-loss timescales shorter than cooling timescales. On the other hand, sub-Neptunes either do not have enough energy for complete atmospheric loss or have mass-loss timescales that are longer than their cooling timescales or the age of the system.

In our numerical simulations, we simultaneously calculate cooling and atmospheric mass-loss of a planet by evolving the planet's energy and atmospheric mass as

$$E_{cool}(t + \mathrm{d}t) = E_{cool}(t) - L(t)\ \mathrm{d}t \text{ and} \tag{3.12}$$

$$M_{atm}(t + \mathrm{d}t) = M_{atm}(t) - \dot{M}_{atm}(t)\ \mathrm{d}t, \tag{3.13}$$

respectively; using Equations (3.2), (3.5), (3.9) and (3.10). We choose an integration time step dt = $10^{-2} \times \min\{t_{cool}, t_{loss}\}$.

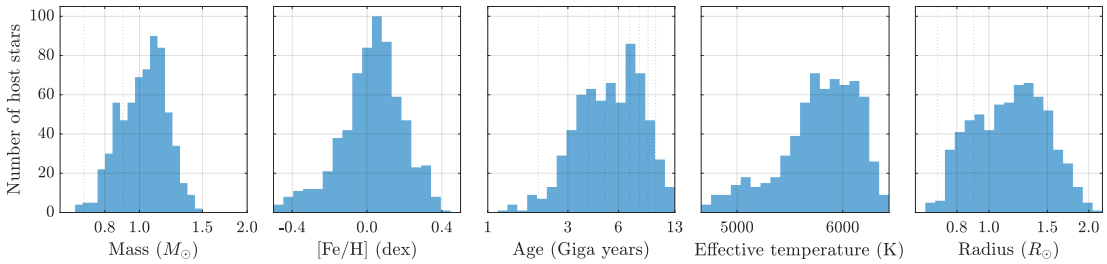

Figure 3.1: Distributions of stellar properties from the CKS dataset (Petigura et al., 2017; Johnson et al., 2017; Fulton et al., 2017, see discussion in Section 3.3.2).

3.3 Modeling the exoplanet population and its host stars

In this section, we discuss how we model the planetary and stellar populations in our numerical simulations.

3.3.1 Exoplanet Population

Following Owen & Wu (2017) and Gupta & Schlichting (2019), we adopt the following orbital period and planet mass distribution to model the exoplanet population:

$$\frac{\mathrm{d}N}{\mathrm{d}\log P} \propto \begin{cases} P^2, & P < 8 \text{ days} \\ \text{constant}, & P > 8 \text{ days, and} \end{cases} \tag{3.14}$$

$$\frac{\mathrm{d}N}{\mathrm{d}M_c} \propto \begin{cases} M_c \exp\left(-M_c^2/(2\sigma_M^2)\right), & M_c < 5\ M_\oplus \\ M_c^{-2}, & M_c > 5\ M_\oplus. \end{cases} \tag{3.15}$$

Here, σ_M is the planet mass where the planet mass distribution peaks. As in Gupta & Schlichting (2019), we assume $\sigma_M = 3M_\oplus$ unless otherwise stated. Throughout this work, we assume that the period distribution is independent of stellar mass, which is, to first order, consistent with observations (Fulton & Petigura, 2018).

3.3.2 Host Star Population

We model the stellar population after the full CKS dataset (Petigura et al., 2017) and use the isochrone-fitted stellar parameters from Johnson et al. (2017). The full CKS dataset consists of 2025 *Kepler* planets. We exactly follow Fulton et al. (2017) to implement a series of cuts to restrict this dataset to a well-characterized sub-sample of 900 planets and 652 host stars. These cuts involve removing false-positive planetary candidates, limiting the sample to planets with impact parameter $b < 0.7$ and orbital periods $P < 100$ days, and excluding faint stars with Kepler-magnitudes $K_p > 14.2$, giant stars (using the empirical criteria mentioned in Fulton et al., 2017) and stars with effective temperatures $T_{\rm eff} < 4700$ K and $T_{\rm eff} > 6500$ K. Hereafter, we simply refer to this refined subset of host stars as the CKS dataset or CKS stellar distribution.

We characterize a host star by the following properties: mass (M_*), radius (R_*), effective temperature ($T_{\rm eff}$), metallicity (Z_*) and age (τ_*). Figure 3.1 shows histograms of these stellar properties from the CKS dataset. We use these parameters as stellar inputs when numerically modelling a planet's thermal evolution and mass-loss while further assuming that the age of the planets is well approximated by the age of their host stars. In total, we evolve a population of 10,000 planets with varying periods and masses (see Equations (3.14) and (3.15)) around each of the 652 CKS stars. The stellar parameters are kept fixed in time, as the stars in our sample are not expected to evolve significantly over the typical core-powered mass-loss timescales, which range from 0.5 to a few Gyrs. We present the results from our core-powered mass-loss model for a host star population modeled after the CKS dataset and compare them with observations in Section 3.4.

In addition, in order to understand the impact of the individual stellar parameters on the observable exoplanet population, we also investigate how the core-powered mass-

loss depends on each of the stellar parameters (mass, metallicity and age) separately in Section 3.5. For the stellar parameters that we do not vary, we assume $M_* = 1\ M_\odot$, $[Z_*/Z_\odot] = 0.0$ dex and $\tau_* = 3$ Gyrs. As in Section 3.4, we evolve a population of 10,000 planets with period and mass distributions given by Equations (3.14) and (3.15) around each of the host stars in the population.

3.4 Results: Comparison with observations

In this section, we compare our core-powered mass-loss results with observations of the planet size distribution and its dependence on orbital period, insolation flux and stellar mass, metallicity and age.

Ginzburg et al. (2018) and Gupta & Schlichting (2019) demonstrated that, for a population of planets around identical 'Sun-like' stars, the core-powered mass-loss mechanism successfully reproduces the radius valley observed in the distribution of small, close-in exoplanets. Here, we extend these previous works to account for the actual, observed properties of the host star population. All the results presented in this section are based on a host star population modeled after the stellar properties of the CKS dataset; see Section 3.3.2 for details. This facilitates direct comparison between our results and observations based on the CKS dataset (e.g., Fulton et al., 2017; Fulton & Petigura, 2018; Owen & Murray-Clay, 2018; Wu, 2019).

In Figures 3.2, 3.3, 3.5 and 3.6, we compare our results with completeness-corrected observations (right-hand panels) from Fulton et al. (2017), Fulton & Petigura (2018) and Owen & Murray-Clay (2018). These studies make completeness-corrections to recover the underlying planet size distribution from the distribution of detected planets. To achieve this, they account for transit and detection probabilities when calculating the underlying

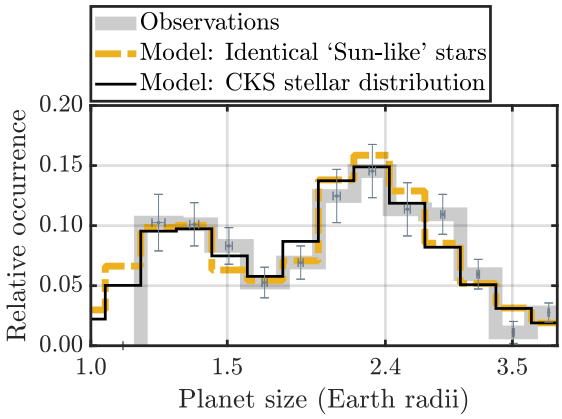

Figure 3.2: Comparison of results based on the core-powered mass-loss evolution model with observations in a one-dimensional histogram of planet size. The thick-gray histogram corresponds to completeness-corrected observations by Fulton et al. (2017, see Table 3) for planets larger than 1.16 $R_\oplus$. The orange-dashed histogram corresponds to the results from Gupta & Schlichting (2019) assuming planetary evolution around identical 'Sun-like' host stars. The thin-black histogram corresponds to results of our model assuming planetary evolution around a distribution of host stars based on the CKS dataset (Johnson et al., 2017; Fulton et al., 2017). The results show good agreement with the observations.

planet occurrence rates. While the transit probability simply depends on the ratio of host star radius and the planet's semi-major axis, the detection probability depends on the signal-to-noise ratio, planet-to-star size ratio and orbital period and is estimated by injecting synthetic transits into the Kepler data to check if they can be recovered or not (Christiansen et al., 2015); for details, see Fulton et al. (2017). In contrast, the observations from Fulton & Petigura (2018) shown in the right-hand panel of Figures 3.4 and 3.11 have not been completeness-corrected such that the relative intensities of the peaks above and below the radius valley are not representative of the underlying planet population.

Figure 3.2 shows a comparison between our core-powered mass-loss results for a host star population modeled on the CKS dataset and with results obtained for 'Sun-like' host stars from Gupta & Schlichting (2019) and completeness-corrected observations reported by the CKS team (e.g. Fulton et al., 2017). The histogram shows no significant difference between results obtained for 'Sun-like' host stars (dashed orange-line) and stars modeled directly after the CKS dataset (thin black-line). Both models show good agreement with the observations (thick grey-line).

3.4.1 Changes in planet size distribution with orbital period and insolation flux

Figure 3.3 shows a comparison, in planet size-orbital period and insolation flux space, of our core-powered mass loss results for CKS host stars (middle-panel), with results based on identical 'Sun-like' host stars (left-panel; Gupta & Schlichting, 2019) and observations (right-panel; Fulton & Petigura, 2018). The core-powered mass-loss results are in good agreement with observations successfully reproducing the location, shape and slope of the valley, as well as the location and magnitude of the peaks of the exoplanet populations above and below the valley. In addition, comparison of the middle- and left-panel shows that the core-powered mass-loss results for the two stellar populations are similar but, accounting for the true properties of the underlying stellar population (middle-panel) reproduces even finer features of the observations (right-panel). For example, our new results can reproduce the 'triangular' shape of the radius valley seen in the observations (right-panel) better than our previous study that was based on identical 'Sun-like' host stars (Gupta & Schlichting, 2019). This is due to the range of stellar parameters used in this work, which leads to a shallower upper edge of the valley compared to results for planets around identical 'Sun-like' stars.

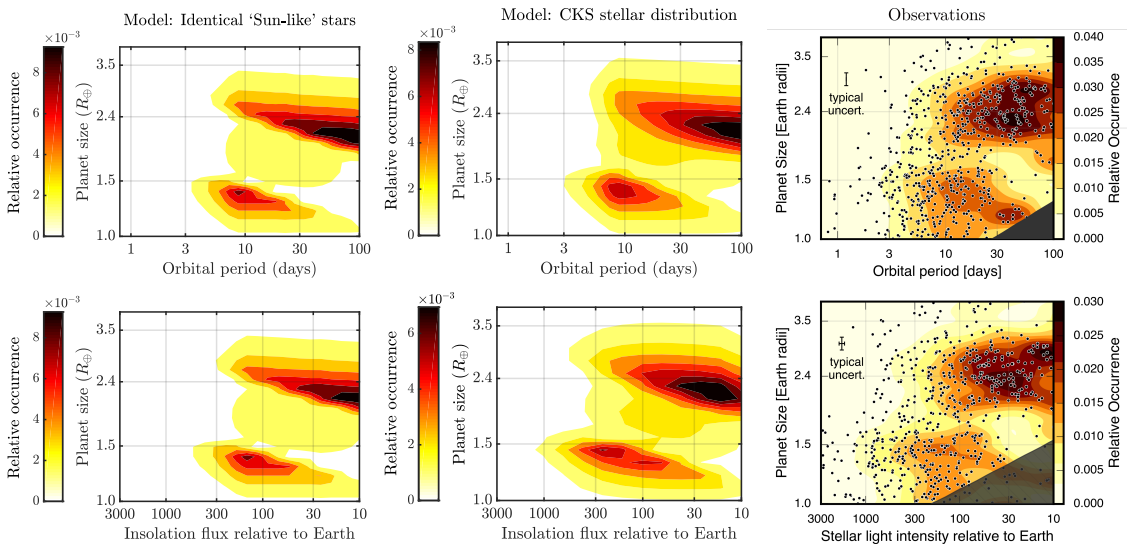

Figure 3.3: Comparison of core-powered mass-loss results with observations. The top row shows planet size as a function of orbital period whereas the bottom row displays planet size as a function of stellar insolation flux. The left panel corresponds to results from Gupta & Schlichting (2019) which were calculated for planets around identical 'Sun-like' host stars, the middle panel displays results from this work for planets around host stars that are modeled after the stellar properties of the CKS dataset (Johnson et al., 2017; Fulton et al., 2017), and the right panel corresponds to completeness-corrected observed planet size distribution from Fulton & Petigura (2018) based on the CKS dataset (reproduced with permission).

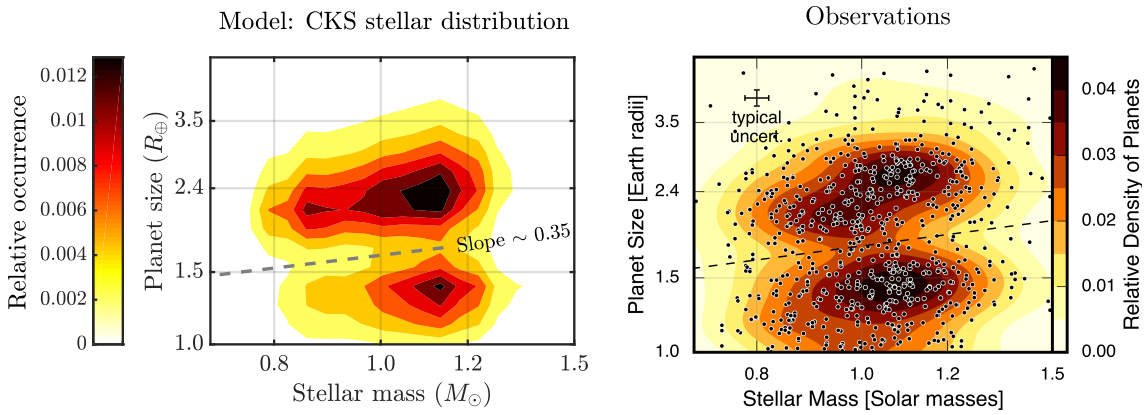

Figure 3.4: Comparison of core-powered mass-loss results (left-panel) with observations (right-panel) from Fulton & Petigura (2018) (reproduced with permission). The left panel shows the dependence of the core-power mass loss results on stellar mass, demonstrating that larger planetary cores are stripped of their envelopes when residing around more massive host stars compared to planets around lower mass stars. This yields a shift in the valley separating the super-Earth and sub-Neptune populations to larger planet radii for higher mass stars. To first order, this slope is driven by the dependence of the core-powered mass-loss mechanism on the bolometric luminosity of the host star as this dictates the outer boundary condition for atmospheric mass-loss. The dashed lines in both panels indicate the shift in the valley's location with stellar mass and are plotted with the same slope. *Note:* Completeness corrections associated with observational bias were not accounted for in the right panel (B.J. Fulton, personal communication). Therefore, the relative occurrence of planets above and below the valley cannot be compared with the observations.

3.4.2 Changes in planet size distribution with stellar mass

Figure 3.4 shows the resulting distribution of planet size as a function of stellar mass from our core-powered mass-loss model (left-panel) and observations from Fulton & Petigura (2018, right-panel). We find that core-powered mass-loss causes the location of the radius valley and the super-Earth and sub-Neptune populations to increase in planet size with increasing stellar mass. This is consistent with observational results from Fulton & Petigura (2018) and Wu (2019). In addition, we find that the slope of the valley in this parameter space is $\mathrm{d}\log R_p/\mathrm{d}\log M_* \sim 0.35$, which is also in excellent agreement with the values obtained from observations (Fulton & Petigura, 2018; Wu, 2019). For example, the dashed line in the right panel of Figure 3.4 from observations by Fulton & Petigura (2018) corresponds to a slope of $\mathrm{d}\log R_p/\mathrm{d}\log M_* \sim 0.35$ and Wu (2019) reports a slope of $\mathrm{d}\log R_p/\mathrm{d}\log M_* \simeq 0.24 - 0.35$ and finds that it extends to M-dwarfs of masses as low as $0.2 M_\odot$. We demonstrate in Section 3.5 that this slope is, to first order, due to the dependence of the core-powered mass-loss mechanism on the bolometric luminosity of the host star as this dictates the outer boundary condition for atmospheric mass-loss.

Dependence on stellar mass as a function of orbital period and insolation flux

Figure 3.5 displays the planet size distribution as a function of period (first row) and insolation (second row) for three stellar mass bins. The observations from Fulton & Petigura (2018) are shown for comparison in rows three and four. Our core-powered mass-loss results (displayed in the first and second row) clearly show that the radius valley moves to larger planet sizes for more massive stars as already shown in Figure 3.4. In addition, we find that the super-Earth and sub-Neptune populations move to higher stellar insolation for more massive stars. This is due to the fact that the exoplanet period distribution is, motivated

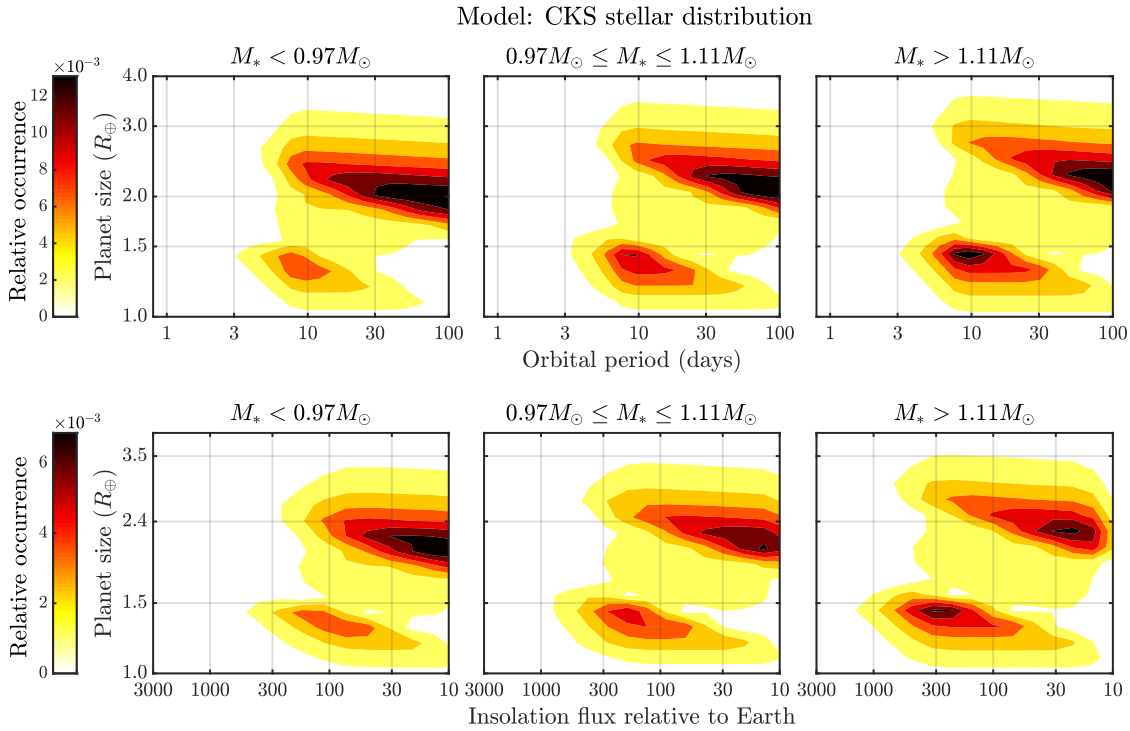

Figure 3.5: Comparison of core-powered mass-loss results (first and second rows: the two rows on this page) with completeness-corrected observations (third and fourth rows: the two rows on the next page) from Fulton & Petigura (2018, reproduced with permission). The planet size distribution is shown for three stellar mass bins as a function of orbital period (first and third row) and stellar insolation flux (second and fourth row). Our core-powered mass-loss results clearly show that the radius valley moves to larger planet sizes for more massive stars (see also Figure 3.4). In addition, we find that the super-Earth and sub-Neptune populations move to higher stellar insolation for more massive stars, which is due to the fact that the exoplanet period distribution is approximately independent of stellar mass. *Figure continued next page*.

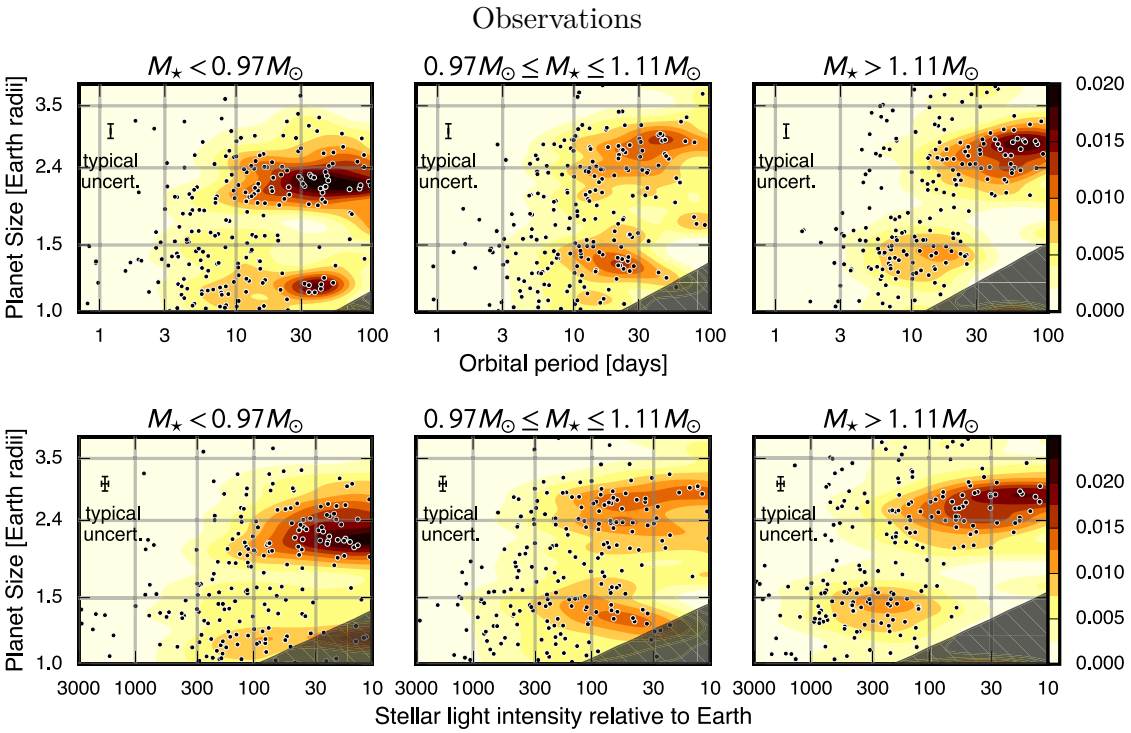

Figure 3.5: *Continued from previous page.*

by observations (see Fulton & Petigura, 2018), assumed to be independent of stellar mass. As a result, planets with the same orbital period move to higher insolation fluxes around higher mass, i.e. more luminous, stars. For a constant period distribution, insolation flux scales with stellar mass as $S \propto M_*^{\alpha-2/3}$, where α is the power-law index of the stellar mass-luminosity relation (see Section 3.5.1 for details). Overall, we find very good agreement between the core-powered mass-loss results and observations. Based on the observational results shown in rows three and four of Figure 3.5, Fulton & Petigura (2018) reported that the planet size distribution shifts to higher stellar insolation flux around more massive stars and interpret this as a signature of photoevaporation. We question this interpretation based on the core-powered mass-loss results shown in rows one and two of the same figure. As discussed, the shift of the planet size distribution to higher stellar insolation flux around more massive stars is a direct result of the fact that the period distribution is approximately independent of stellar mass. In addition, one needs to be cautious with such claims until the effect of all stellar properties on the results are considered collectively since stellar age and metallicity conspire together such that sub-Neptunes are larger for younger and higher metallicity stars, both of which are correlated with stellar mass in the CKS dataset (see Section 3.5 for details).

In addition, a shift in the exoplanet distribution to higher insolation as a function of stellar type has also been observed around M-dwarfs. Hirano et al. (2018) reported that around early, less XUV active M-dwarfs, planets are located at higher insolation flux in comparison to mid-to-late, more XUV active M-dwarfs; see their Figures 18 and 19. Hirano et al. (2018) interpret this as a signature of photoevaporation. However, if this is indeed a signature of photoevaporation transforming sub-Neptunes into super-Earths, then Hirano et al. (2018) should also have found rocky super-Earths at higher insolation around the more active M-dwarfs, as they are the remnants of the stripped sub-Neptunes. However,

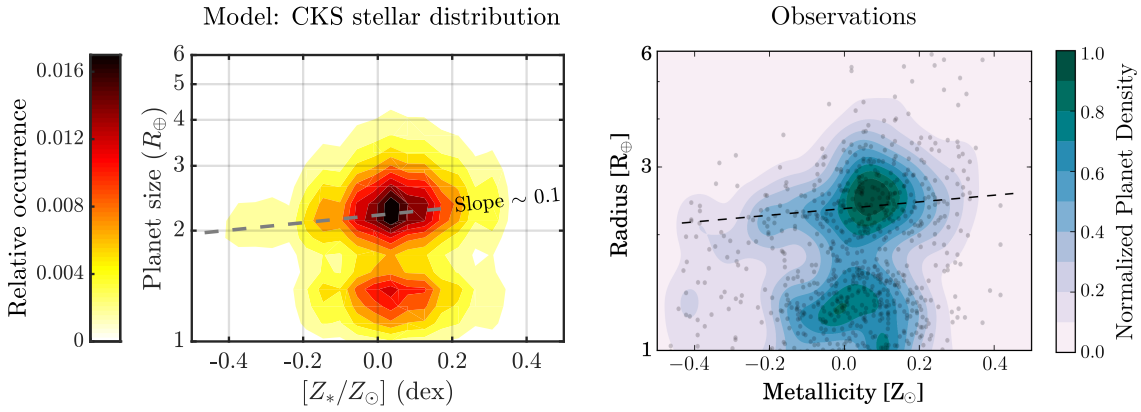

Figure 3.6: Comparison of core-powered mass-loss results as a function of metallicity, $[Z_*/Z_\odot]$ (left panel), with completeness-corrected observations from Owen & Murray-Clay (2018) (right panel). The dashed lines in both panels indicate the increase in the size of sub-Neptunes with metallicity with a slope of $\mathrm{d}\log R_p/\mathrm{d}\log Z_* \sim 0.1$. Sub-Neptunes are on average larger around metal-rich stars, since higher atmospheric opacities result in longer thermal contraction and cooling timescales. In contrast, the location and slope of the radius valley, as well as the average sizes of super-Earths are, to first order, independent of metallicity; see Section 3.5.2 for details.

no such population is detected. Therefore, this observed shift in insolation is unlikely a signature of an atmospheric mass-loss mechanism. Instead, Figures 18 and 19 from Hirano et al. (2018) might be evidence of protoplanetary disk truncation around M-dwarfs which could be caused by disk-photoevaporation, or some other process.

3.4.3 Changes in planet size distribution with stellar metallicity

The left panel of Figure 3.6 shows core-powered mass-loss results as a function of stellar metallicity. We find that the size of sub-Neptunes increases with increasing stellar metal-

licity whereas neither the radius valley nor population of super-Earths show any visually discernible dependence on stellar metallicity. Specifically, we find that the average size of sub-Neptunes increases with stellar metallicity (represented by the inclination of the contours of the sub-Neptune population) such that $\mathrm{d}\log R_p/\mathrm{d}\log Z_* \sim 0.1$. These finding are consistent with observations by Petigura et al. (2018), Dong et al. (2018) and Owen & Murray-Clay (2018). The right panel of Figure 3.6 shows observations from Owen & Murray-Clay (2018) based on the CKS dataset (Johnson et al., 2017; Fulton et al., 2017). The dashed line, roughly drawn to indicate the observational trend of planet size with stellar metallicity for the sub-Neptune population, has a slope of $\mathrm{d}\log R_p/\mathrm{d}\log Z_* \sim 0.1$. We note here that observations show hardly any change in the location of the valley as a function of stellar metallicity. This suggests that, to first order, changes in metallicity predominately impact the sizes of sub-Neptunes but not the super-Earth population. As we show in the next section (see Section 3.5.2), these observations are consistent with results from our core-powered mass-loss model, which predicts no metallicity dependence of the radius valley and the super-Earth population. The observed planet size-metallicity trend displayed in the sub-Neptune population is also consistent with the results in Section 3.5.2. However, as the trend in the sub-Neptune population is predominately due to that fact that the thermal contraction timescales are prolonged for higher envelop opacities/metallicities, the observed planet size-metallicity trend is not a unique signature of the core-powered mass-loss mechanism.

3.4.4 Changes in planet size distribution with stellar age

Figure 3.7 shows core-powered mass-loss results vary as a function of age for a population of planets with host stars modeled after the CKS dataset (Johnson et al., 2017; Fulton et al.,

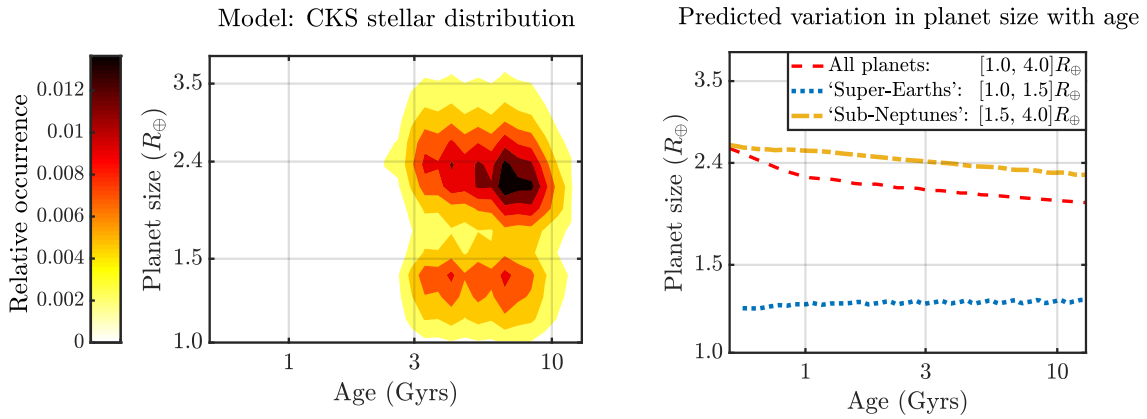

Figure 3.7: Core-powered mass-loss results as a function of age. The left panel shows theoretical results for a planet population around a distribution of host stars modeled after the CKS dataset (Johnson et al., 2017; Fulton et al., 2017); the right panel shows our predicted average planet size with age. These results demonstrate that the average size of sub-Neptunes decreases significantly while the average size of super-Earths increases slightly with age. In addition, we predict that the relative occurrence of sub-Neptunes with respect to super-Earths decreases with age over Gyr timescales. These trends are due to the fact that typical mass-loss timescales are on the order of 0.5-1 Gyrs, which leads to an increase of super-Earths with respect to sub-Neptunes over these timescales. In addition the envelopes of sub-Neptunes will have had more time to cool and contract resulting in a decrease in the average sub-Neptune size with age; see Section 3.5.3 and Figure 3.10 for details.

2017). We predict that sub-Neptunes are visibly smaller around older stars since their envelopes had more time for thermal contraction in older systems, whereas super-Earths have similar but slightly larger sizes as a function of age. We note here, no observations are shown in Figure 3.7. Given the small range in stellar ages and their relatively larger uncertainties, no direct statistical comparison between core-powered mass-loss results and observations is currently possible (but see discussion in Section 3.5.3 for details).

In this section, we discussed our core-powered mass-loss results for a population of planets with host stars modeled after the CKS dataset and showed that the core-powered mass-loss mechanism can reproduce and explain a multitude of observational trends (e.g., Fulton & Petigura, 2018; Owen & Murray-Clay, 2018; Petigura et al., 2018; Dong et al., 2018; Wu, 2019). In the next section, we explain the key physical properties of the core-powered mass-loss mechanism that lead to the results presented here and make observational predictions for the core-powered mass-loss mechanism as a function of stellar properties.

3.5 Results: Analytical scalings and dependence on stellar properties

In this section, we explore and explain, analytically and numerically, the dependence of the core-powered mass-loss mechanism on stellar mass, metallicity and age by only varying one of these stellar parameters at a time.

We assume, with the exception of Section 3.5.4, the same planet mass and orbital period distribution for all host stars such that any changes in the resulting planet size distribution can be unambiguously attributed to changes in the host star properties. Unlike in Section 3.4, where we modeled the host stars after the CKS dataset, here we assume a uniform

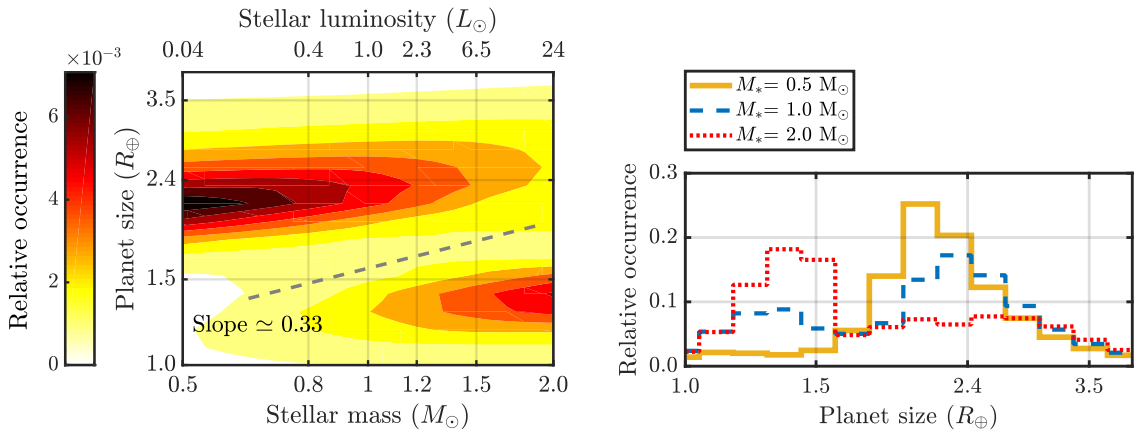

Figure 3.8: Core-powered mass-loss results as a function of stellar mass (luminosity) for planets around solar metallicity stars after 3 Gyrs of thermal evolution and mass-loss. Here, only the stellar mass is varied while keeping all other parameters the same. The left panel shows the two-dimensional distribution of planet size as a function of stellar mass (luminosity); the right panel displays the corresponding histograms of planet sizes for stellar masses of $0.5M_\odot$ (yellow-solid line), $1M_\odot$ (blue-dashed line), and $2M_\odot$ (red-dotted line), respectively. The dashed line in the left panel corresponds to the slope of the radius valley, $\mathrm{d}\log R_p/\mathrm{d}\log M_* \simeq 0.33$, derived analytically in Equation (3.18).

distribution for the single stellar parameter that we are varying. For the parameters that are held constant, we assume solar values for metallicity and mass, and an age of 3 Gyrs.

3.5.1 Dependence on stellar mass

Stellar mass plays a role when modelling atmospheric loss driven by the core-powered mass-loss mechanism in two ways: (i) it relates the orbital period distribution of the planet population to the semi-major axis and (ii) it dictates the equilibrium temperature $T_{\rm eq}$ for each planet given its distance from the host star. The equilibrium temperature depends

on the bolometric luminosity L_* and the semi-major axis a such that $T_{\rm eq} \propto L_*^{1/4} a^{-1/2}$. The bolometric luminosity, in turn, can be expressed as $L_* \propto T_{\rm eff}^4 R_*^{-2}$, where $T_{\rm eff}$ is the effective temperature of the star and R_* the stellar radius. The CKS dataset provides both, stellar radii and effective temperatures. However, the bolometric luminosity is also strongly correlated with the stellar mass M_* such that

$$L_*/L_\odot = (M_*/M_\odot)^\alpha. \tag{3.16}$$

The dependence of the core-powered mass-loss mechanism on stellar mass is, to first order, driven by the stellar mass-luminosity relation, since more massive stars have higher luminosity which leads to higher $T_{\rm eq}$ and hence more mass loss from the planet.

While we directly use stellar radius and effective temperature to derive a star's luminosity for the numerical simulation results discussed in Section 3.4, in this section we use the stellar mass-luminosity relation to isolate the effect of stellar mass on the resulting radius valley and planet size distribution. Given the stellar mass-luminosity relation, for a fixed period distribution we get $T_{\rm eq} \propto M_*^{(\alpha/4)-(1/6)}$, which sets the temperature at a planet's Bondi radius. Gupta & Schlichting (2019) showed that the slope and location of the valley in the planet distribution is set by the condition $t_{loss} = t_{cool}$. Furthermore, they showed that this condition is very well approximated by $GM_p/c_s^2 R_{rcb} = $ constant, due to the exponential dependence of t_{loss}^B (see Section 3.2). Substituting for the speed of sound, the mass-radius relation of the core, and using the fact that $R_{rcb} = R_p \simeq 2R_c$ yields

$$R_p^3 T_{\rm eq}^{-1} \simeq \text{constant}. \tag{3.17}$$

Substituting for $T_{\rm eq}$ using the stellar mass-luminosity relation we find

$$\frac{\mathrm{d}\log R_p}{\mathrm{d}\log M_*} = \frac{3\alpha - 2}{36} = 0.33 \text{ for } \alpha = 4.6. \tag{3.18}$$

Here we evaluated the last equality for $\alpha = 4.6$, which is the best-fit value we measured from the CKS dataset. This analytical estimate of the slope is in good agreement with the observations based on the CKS dataset which find $\mathrm{d}\log R_p/\mathrm{d}\log M_* \sim 0.35$ (e.g., Fulton & Petigura, 2018; Wu, 2019), with the results of our numerical simulations discussed in Section 3.4 and with the numerical results based on the mass-luminosity relation, which is only used in Section 3.5.1, as shown in Figure 3.8. In addition, we predict that, if planetary evolution is dominated by core-powered mass-loss, the radius valley will have a slope $\mathrm{d}\log R_p/\mathrm{d}\log M_* = (3\alpha - 2)/36$ and hence will be steeper for planets around host star populations with larger α and vice-versa (e.g., Eker et al., 2018). This trend would be weakened if photoevaporation or other mass-loss processes also play a significant role in shaping the exoplanet radius distribution.

We note here, while the value of α that we measure directly from the CKS dataset is somewhat larger than what is predicted by simple theoretical models, it is in agreement with observational measurements of the mass-luminosity relation for stars in the solar neighbourhood (Eker et al., 2018). For example, Eker et al. (2018) find values of α ranging from 4.3 to 5.7 for the relevant stellar masses in the CKS dataset. Furthermore, the CKS dataset is a magnitude-limited rather than a volume-limited sample thereby including more high luminosity/mass stars.

Figure 3.8 displays the planet size distribution as a function of stellar mass (luminosity) assuming that all host stars are 3 Gyrs old and have solar metallicity. The left panel of Figure 3.8 shows the location of the valley and that the size of super-Earths and sub-Neptunes increases with increasing stellar mass (or luminosity) as derived analytically in Equation (3.18) and as shown by the black-dashed line in the figure. In other words, planets around more massive stars are, on average, bigger in size. In addition, the relative abundance of sub-Neptunes decreases and that of super-Earths increases with increasing

stellar mass. This is because planets around more massive or luminous stars are more susceptible to losing their atmospheres as they have higher equilibrium temperatures which result in shorter mass-loss timescales and thus a higher fraction of sub-Neptunes become super-Earths around more massive stars. These two results are also evident from the right panel of Figure 3.8 which shows the radius distribution for host star masses corresponding to $0.5M_{\odot}$, $1.0M_{\odot}$ and $2.0M_{\odot}$, respectively. These results explain observations reported by Fulton & Petigura (2018) and Wu (2019) who find that the radius valley increases in planet size with increasing stellar mass.

Assuming that the orbital period distribution is independent of stellar mass, this observation seems surprising under a basic framework of photoevaporation since the XUV flux roughly remains constant as a function of stellar mass and hence should yield an approximately flat radius valley as a function of host star mass; see also Wu (2019). This is because the ratio of XUV to bolometric flux decreases with stellar mass (e.g., Jackson et al., 2012; Tu et al., 2015) while the bolometric flux increases. These two trends roughly cancel each other (Owen & Murray-Clay, 2018). Therefore, in order to explain radius valley's dependence on stellar mass with photoevaporation models, Wu (2019) invoked a linear correlation between the planet mass distribution and host star mass and thereby is able to match the observations.

As shown above and in Section 3.4, the core-powered mass-loss mechanism yields a shift in the radius valley to larger planet sizes around more massive stars with a slope given by $\mathrm{d}\log R_p/\mathrm{d}\log M_* \simeq 0.33$, in agreement with observations. We therefore find, in contrast to photoevaporation models, no evidence for a linear correlation between planet and stellar mass. We nonetheless investigate the imprint that a linear correlation between planet and stellar mass would have on the observed planet size distribution in the context of the core-powered mass-loss mechanism in Section 3.5.4.

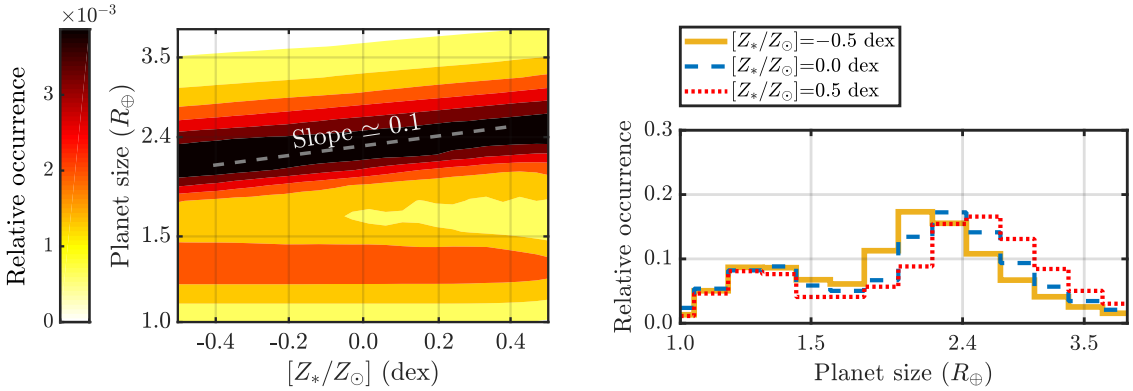

Figure 3.9: Core-powered mass-loss results as a function of stellar metallicity for planets around solar mass stars after 3 Gyrs of thermal evolution and mass-loss. The left panel shows the distribution of planet size as a function of metallicity $\equiv [Z_*/Z_\odot]$; the right panel displays the corresponding histograms of planet size for metallicities of -0.5 dex (yellow-solid line), 0.0 dex (blue-dashed line), and 0.5 dex (red-dotted line), respectively. The gray-dashed line in the left-panel shows the increase in the size of sub-Neptunes with metallicity, i.e., $\mathrm{d}\log R_p/\mathrm{d}\log Z_* \simeq 0.1$, derived analytically in Equation (3.20). In contrast to the sub-Neptune population, the location of the valley, specifically the lower edge of the valley defining the upper envelope of the super-Earth population, shows no significant dependence on metallicity. Furthermore, this figure also shows that the relative occurrence of sub-Neptunes with respect to super-Earths increases with increasing metallicity.

3.5.2 Dependence on stellar metallicity

The rate at which planets cool and contract depends on the opacity of the envelope, κ, as this sets the rate of radiative diffusion through the radiative-convective boundary (see Equations (3.6) and (3.8)). If the opacity at the radiative-convective boundary is proportional to the stellar metallicity, Z_*, as we assume in Section 3.2, then the planetary cooling timescale is directly proportional to the stellar metallicity such that $t_{cool} \propto Z_*$. In other words, a planet around a metal-poor star, i.e., a planet with lower atmospheric opacity, loses its energy on a shorter timescale than around a higher metallicity star. As a result, sub-Neptunes will be larger around higher metallicity stars than metal poor stars when comparing systems of the same age. We can derive an analytical estimate for the size of sub-Neptunes as a function of metallicity by assuming that atmospheric mass-loss can be neglected such that M_{atm} = constant and thus cooling and contraction due to mass-loss can be ignored. In this case, Equations (3.1), (3.2) and (3.5) to (3.7) can be combined to yield

$$t \propto Z_* \Delta R^{-\frac{\beta\gamma+1}{\gamma-1}}, \tag{3.19}$$

where t is the age of the system and where we used Equation (3.1) and the assumption that M_{atm} = constant to eliminate the dependence on the density at the R_{rcb}. Hence, from Equation (3.19) we have that at a given time $\Delta R \propto Z_*^{(\gamma-1)/(\beta\gamma+1)}$ such that

$$\frac{\mathrm{d}\log R_p}{\mathrm{d}\log Z_*} = \frac{\Delta R}{R_p}\left(\frac{\gamma-1}{\beta\gamma+1}\right) \simeq \frac{5}{46}, \tag{3.20}$$

where we substitute $\gamma = 7/5$, $\beta = 0.6$ (see Equation 3.7) and $\Delta R/R_p \simeq 1/2$ in the last step. We note here that approximating $\Delta R/R_p$ as $\simeq 1/2$, which is essentially our initial condition, results in the maximum slope possible and since $\Delta R/R_p$ decreases over time as the envelope cools and contracts. The value calculated in Equation (3.20) is therefore an

overestimate of the slope for a planet population with an age of 3 Gyrs.

The left panel of Figure 3.9 shows the planet size distribution as a function of metallicity, where we assume that the planet's opacity scales linearly with stellar metallicity (see Equation (3.7)). The size trend with metallicity and slope of the sub-Neptune population from our numerically evolved planet population agrees well with the simple analytical estimate derived in Equation (3.20) above. In addition, this analytical scaling matches the observations (Owen & Murray-Clay, 2018) and our numerical results discussed in Section 3.4 where $\mathrm{d}\log R_p/\mathrm{d}\log Z_* \sim 0.1$; see also Figure 3.6. Our results are also consistent with observations reported by Dong et al. (2018), Owen & Murray-Clay (2018) and Petigura et al. (2018) who all find that sub-Neptunes are larger around more metal-rich stars. Our results similarly apply to M-dwarfs and can explain observations that find that planets, on average, are larger around higher metallicity M-dwarfs (Hirano et al., 2018). These results are also evident from the right panel of Figure 3.9 which shows the planet size distribution for host star metallicities of -0.5, 0.0 and 0.5 dex, respectively.

In contrast to the sub-Neptune population, core-powered mass-loss predicts a negligible dependence of the location of the radius valley and sizes of super-Earths as a function of metallicity. This is because, as shown in Gupta & Schlichting (2019) and summarized in Section 3.5.1, the slope of the radius valley is, to first order, given by $GM_p/c_s^2 R_{rcb} =$ constant. Therefore, as long as the spontaneous mass-loss phase (boil-off phase) results in initial planet sizes $R_{rcb} = R_p \simeq 2R_c$ independent of envelope metallicity, we find that the slope of the valley, especially the lower edge that marks the upper envelope of the super-Earth population, does not depend on metallicity. This explains the almost flat contours of the super-Earth population shown in Figure 3.9 and the flat valley shown in Figure 3.6 and is the reason why, to first order, only the sizes of sub-Neptunes depend on stellar metallicity but not the location of the valley or the sizes of super-Earths.

In reality, there is a weak dependence of the radius valley and super-Earth sizes on metallicity because the atmospheric mass-loss timescales increase with stellar metallicity such that at a given time, planets with higher atmospheric opacities will have lost less of their envelopes than those with lower envelope opacities. This leads, for a given age, to smaller cores (super-Earths) around metal-rich stars compared to metal poor ones. This in addition implies that, at a given time, the relative abundance of super-Earths to sub-Neptunes should be higher around lower metallicity stars, as can be seen in Figure 3.9. These results offer an explanation as to why the relative occurrence of sub-Neptunes increases with increasing metallicity as found observationally by Petigura et al. (2018) and Dong et al. (2018).

3.5.3 Dependence on stellar age

Atmospheric mass-loss driven by the cooling of the underlying core depends on the age of the system as mass-loss and thermal evolution extend, in contrast to photoevaporation, over Gyr timescales (see Section 3.2 for details). This implies that sub-Neptunes around older stars will be smaller than those around younger stars since the former will have had more time to cool and contract. Moreover, planets that eventually become super-Earths have had more time to complete their mass loss in older systems. Thus, older stars will have a higher abundance of super-Earths relative to sub-Neptunes compared to younger stars. Specifically, we expect a drastic change in the planet size distribution between stars that are younger and older than the typical core-powered mass-loss timescale, which is of the order of a Gyr. Due to these long mass-loss timescales, we predict the transformation of sub-Neptunes into super-Earths to continue over Gyr timescales.

Assuming a constant metallicity, we have from Equation (3.19) that the radii of the

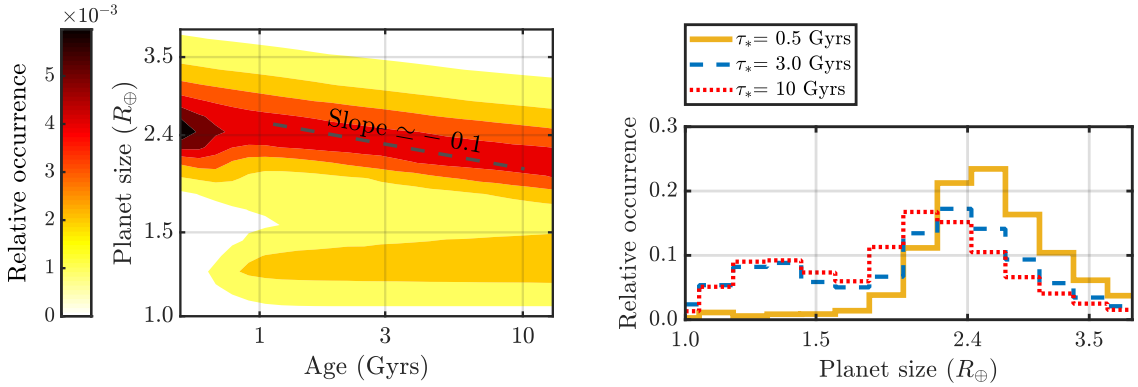

Figure 3.10: Core-powered mass-loss results as a function of stellar age for planets with solar mass and solar metallicity host stars. The left panel shows the distribution of planet sizes as a function of age; the right panel displays the corresponding histograms of planet size for ages of 0.5 Gyrs (yellow-solid line), 3.0 Gyrs (blue-dashed line), and 10 Gyrs (red-dotted line), respectively. The dashed line in the left panel shows the decrease in the size of sub-Neptunes with age, i.e., $\mathrm{d}\log R_p/\mathrm{d}\log\tau_* \simeq -0.1$, derived analytically in Equation (3.21). In contrast to the sub-Neptunes, the average size of super-Earths increases with age. In addition, this figure shows that the relative abundance of super-Earths to sub-Neptunes increases over time, as expected.

sub-Neptune population vary with age as

$$\frac{\mathrm{d}\log R_p}{\mathrm{d}\log \tau_*} = -\frac{\Delta R}{R_p}\left(\frac{\gamma - 1}{\beta\gamma + 1}\right) \simeq -\frac{5}{46}, \tag{3.21}$$

where we again substitute $\gamma = 7/5$, $\beta = 0.6$ and $\Delta R/R_p \simeq 1/2$ in the last step. Just like for the metallicity dependence, the value calculated in Equation (3.21) is an overestimate of the slope for a planet population with an age of 3 Gyrs (see discussion following Equation (3.20) for details). Nonetheless, this analytical estimate agrees with our numerical results shown in Figure 3.10.

The left panel of Figure 3.10 shows the changes in planet size as a function of age for solar mass and solar metallicity host stars. As expected, sub-Neptunes decrease in size with increasing stellar age as their envelopes cool and contract. Moreover, we find an increase in the average size of super-Earths with age as larger (more massive) cores are being stripped of their envelopes over time. This, in addition, leads to an increase in the number of super-Earths relative to sub-Neptunes with time. These results are displayed in the right panel of Figure 3.10 which shows the planet size distribution for host stars with ages of 0.5, 3.0 and 10.0 Gyrs. The core-powered mass-loss mechanism therefore predicts that sub-Neptunes decrease in size, while the average size of super-Earths increases with stellar age and that the relative abundance of super-Earths with respect to sub-Neptunes increases with time, especially over periods from 500 Myrs to 3 Gyrs.

The relatively large uncertainties in most stellar ages currently do not allow for a detailed comparison between predictions from the core-powered mass-loss mechanism and observations. However, according to Mann et al. (2016) and other ZEIT studies, younger planets (in stellar clusters $\sim$ 10-650 Myrs old) are on average bigger than the older *Kepler* planets ($\gtrsim$ 1 Gyr old); see Figure 12 in Rizzuto et al. (2018). According to these studies, close-in planets likely lose significant portions of their atmospheres even after the

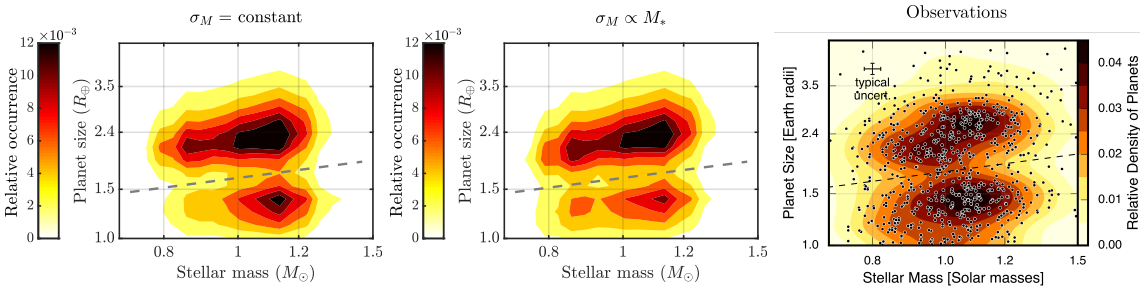

Figure 3.11: Comparison of core-powered mass-loss results (left and middle panel) with observations (right-panel) from Fulton & Petigura (2018, *continued next page*).

first few hundred million years. If correct, these observations directly confirm predictions from core-powered mass-loss with its Gyr-long mass-loss timescales (see also Ginzburg et al., 2016) and would be challenging to explain with photoevaporation which mostly occurs over the first 100 Myrs.

3.5.4 Investigating proposed correlations between the planet- and stellar-mass distributions

As mentioned above, to reconcile the observed correlation between the location of the radius valley with stellar mass considering only atmospheric-loss due to photoevaporation, Wu (2019) had to invoke a linear correlation between the planet- and stellar-mass distributions. Specifically, she inferred that the peak of the planet mass distribution, i.e., σ_M (see Equation (3.15)), scales linearly with the mass of the host star.

In Sections 3.4 and 3.5.1, we demonstrate that no such correlation is required when accounting for planetary evolution and atmospheric loss driven by the core-powered mass-loss mechanism. In other words, we find that in order to explain the observations we don't need to impose a linear correlation between the planet- and stellar-mass distribution as

Figure 3.11: Comparison of core-powered mass-loss results (left and middle panel) with observations (right-panel) from Fulton & Petigura (2018). The left and middle panel show the resulting planet size distribution assuming no correlation between planet- and stellar-mass (left-panel) and for a linear correlation between the planet- and stellar-mass distributions (middle-panel), respectively. σ_M corresponds to the peak in the planet mass distribution (see Equation (3.15) for details). The dashed lines indicate the slopes of the radius valley which are given by $\mathrm{d}\log R_p/\mathrm{d}\log M_* \simeq 0.35$. Comparing the left and middle panels with the observations (right-panel) shows that assuming a linear-scaling between the planet- and stellar-mass distributions (middle-panel) and no-scaling (left-panel) both yield similar slopes which are both consistent with observations (left-panel). Core-powered mass-loss models only yield a slightly steeper slope when assuming a linear-scaling between the planet- and stellar-mass distributions compared to no-scaling because, to first order, the location of the radius valley is independent of the underlying planet mass distribution (see Section 3.4 of Gupta & Schlichting, 2019, for details). As evident when comparing the left and middle panels, the intensities of the peaks above and below the valley are sensitive to the details of the planet mass distribution, but we are currently not able to favour one model over the other on this basis as the observations from Fulton & Petigura (2018) that we are comparing to, in the right panel, have not been completeness-corrected. As before, the ages, metallicities and masses of the host stars are modeled after the stellar distribution from the CKS dataset (Johnson et al., 2017; Fulton et al., 2017).

inferred by Wu (2019) for their photoevaporation model. Nevertheless, in this section we investigate how our core-powered mass-loss results would change if we impose a linear relation between the planet- and stellar-mass distribution. Specifically, we assume that $\sigma_M/3M_\oplus = M_*/M_\odot$ (see Equation (3.15) for details).

Figure 3.11 demonstrates that the slope of the valley is similar when assuming no correlation between the planet- and stellar-mass distributions (left-panel) or a linear correlation between the planet- and stellar-mass distributions (middle-panel). Furthermore, both models yield a good fit to observations from Fulton & Petigura (2018) (right-panel) and both match a slope of $\mathrm{d}\log R_p/\mathrm{d}\log M_* \simeq 0.35$ given by the dashed line in all three panels. Core-powered mass-loss models only yield a slightly steeper slope when assuming a linear-scaling between the planet- and stellar-mass distributions compared to no-scaling because, to first order, the location of the radius valley is independent of the underlying planet mass distribution (see Section 3.4 of Gupta & Schlichting (2019) for details). As evident when comparing the left and middle panels, the intensities of the peaks above and below the valley are sensitive to the details of the planet mass distribution. However, we are currently not able to favour one model over the other on this basis because the observations from Fulton & Petigura (2018) that we are comparing to in the right panel have not been completeness corrected for the relative intensities of the two peaks above and below the valley.

In summary, since the slope of the radius valley is, to first order, not sensitive to the planet-mass distribution for the core-powered mass-loss mechanism, we do not find evidence for a linear correlation between the stellar- and planet-mass distributions, but we cannot rule it out either.

3.6 Discussion and Conclusions

In this paper we extended previous work on the core-powered mass-loss mechanism (Ginzburg et al., 2018; Gupta & Schlichting, 2019), and investigated how stellar mass, metallicity and age impact the resulting planet size distribution.

We first investigated the evolution of planets around a population of host stars modeled after the CKS dataset (Johnson et al., 2017; Fulton et al., 2017). This allows for a direct comparison between our core-powered mass-loss results and observations based on the CKS data set. We find that, to first order, the resulting planet size distribution as a function of period and/or stellar insolation is very similar to that obtained by Gupta & Schlichting (2019), who only considered 'Sun-like' host stars. However, modeling the actual host star properties yields, as expected, an even higher degree of agreement between core-powered mass-loss results and the observations (Fulton & Petigura, 2018). In addition, we find that our core-powered mass-loss results are in excellent agreement with the observed planet size distribution as a function of both stellar mass (e.g., Fulton & Petigura, 2018; Wu, 2019) and metallicity (e.g., Owen & Murray-Clay, 2018; Petigura et al., 2018; Dong et al., 2018; Hirano et al., 2018). Furthermore, our results also explain the shift in the planet size distribution to higher insolation flux as a function of stellar mass, as observed by Fulton & Petigura (2018).

In addition, we investigated how our core-powered mass-loss results depend on stellar mass, metallicity and age separately. This enabled us not only to understand the key physical processes responsible for the agreement of our results with observations, but also enables us to make predictions for the planet size distribution and its dependence on a wide rage of stellar parameters.

We find that the planet size distribution varies with stellar mass because core-powered

mass-loss depends on the bolometric luminosity which, in turn, is strongly correlated with stellar mass. Thus, more massive stars host planets with higher equilibrium temperature, making even more massive planets susceptible to complete atmospheric loss. We derived an analytical estimate for the slope of the valley in planet size and stellar mass parameter space and show that $\mathrm{d}\log R_p/\mathrm{d}\log M_* \simeq (3\alpha - 2)/36$, where α is the power-low index relating stellar mass and luminosity, such that $L_*/L_\odot = (M_*/M_\odot)^\alpha$. We find that $\alpha \simeq 4.6$ for the host stars in the CKS dataset and use this to calculate that $\mathrm{d}\log R_p/\mathrm{d}\log M_* \simeq 0.33$. This analytical estimate is in good agreement with our numerical results and the observations (Fulton & Petigura, 2018; Wu, 2019).

In contrast to stellar mass, we find that, to first order, that the core-powered mass-loss mechanism predicts a negligible dependence of the location of the radius valley as a function of metallicity and age. This is because, as shown in Gupta & Schlichting (2019) and summarized in Section 3.5.1, the slope of the radius valley is, to first order, given by $GM_p/c_s^2 R_{rcb}$ = constant, which has no explicit dependence on metallicity or age. Therefore, as long as the spontaneous mass-loss phase (boil-off phase) results in initial planet sizes $R_{rcb} = R_p \simeq 2R_c$ independent of envelope metallicity or age, we have that the slope of the valley, especially the lower edge that marks the upper contour of the super-Earth population, does not depend on metallicity or age. In reality, there is a weak dependence on age and metallicity resulting in slightly larger cores that are stripped as a function of time (see Figure 3.10) and slightly smaller cores that are stripped of their atmospheres as a function of metallicity (see Figure 3.9). This dependence is due to the metallicity's effect on the mass-loss timescale. However, since this metallicity dependence does not appear in the exponent of the mass-loss timescales, the metallicity and hence age dependence is only a second-order effect and hence weak.

Unlike the location and slope of the radius valley, the size distribution of the sub-

Neptune population does display a visible dependence on both metallicity and age. This is because the rate at which the envelope cools and contracts is related to its opacity. The size of sub-Neptunes therefore depends on both the opacity of the envelope and the age of the system. Assuming that the envelope opacity is proportional to the stellar metallicity, the cooling timescale is directly proportional to the stellar metallicity. As a result, sub-Neptunes will be larger around higher metallicity and/or younger stars than metal poor and/or older stars. We derived an analytical estimate for the size of sub-Neptunes as a function of metallicity and age and showed that $\mathrm{d}\log R_p/\mathrm{d}\log Z_* \simeq 0.1$ and $\mathrm{d}\log R_p/\mathrm{d}\log \tau_* \simeq -0.1$, respectively. Both of these analytical estimates are in agreement with our numerical results. In addition, the former is in good agreement with the observations of sub-Neptunes around metal-rich FGK stars (Owen & Murray-Clay, 2018; Dong et al., 2018; Petigura et al., 2018) and M-dwarfs (Hirano et al., 2018); no direct comparison with observations can yet be made for the latter.

Although we just discussed here the dependence of the core-powered mass-loss mechanism on stellar mass, metallicity and age in isolation, some of these trends can be more pronounced in the observations because, for example, in the CKS dataset more massive stars are on average younger and more metal-rich.

3.6.1 Observational test: Distinguishing between core-powered mass-loss and photoevaporation signatures

Although both photoevaporation and core-powered mass-loss can explain the observed radius valley in the exoplanet size distribution and both mechanisms are likely to operate in conjunction in many systems, their different timescales and different dependencies on stellar properties provide a set of observational predictions that allow for the determination

of their relative importance. Specifically, we make the following observational predictions:

3.6.1.1 Correlations between planet- and stellar-mass

According to our core-powered mass-loss results, we find no evidence for a linear correlation between the host star and planet mass distributions. However, we cannot rule out such a linear correlation either, because the location of the radius valley in the core-powered mass-loss scenario does not strongly depend on planet mass (see Section 3.4 from Gupta & Schlichting, 2019, for details).

3.6.1.2 Slope of the radius valley as a function of stellar mass (or luminosity)

Since the positive correlation between the location of the radius valley with stellar mass is mainly due to the stellar mass-luminosity relation, the core-powered mass-loss model can be tested by examining the slope of the radius valley for different stellar masses. For example, as shown above, the slope of the radius valley as a function of stellar mass is given by $\mathrm{d}\log R_p/\mathrm{d}\log M_* = (3\alpha - 2)/36$, where $L_*/L_\odot = (M_*/M_\odot)^\alpha$. The slope will therefore be steeper for planets around host stars with larger α and vice-versa. Best of all, one can examine planets around two host star populations with different α (α can be directly determined from the host stars in the sample) and check for the predicted change in slope of the radius valley as a function of stellar mass (or luminosity).

3.6.1.3 Relative abundance of super-Earths and sub-Neptunes as a function of age

Since atmospheric mass-loss driven by the core-powered mass-loss mechanism proceeds over Gyr timescales, we predict that the relative abundance of super-Earths with respect to

sub-Neptunes increases with age. Specifically, we expect the abundance of super-Earths to continue to increases significantly after 500 Myrs, since typical atmospheric mass-loss timescales are of the order of a Gyr. In contrast, since photoevaporation is driven by the X-ray and EUV radiation from the host star, which declines drastically after the first 100 Myrs, the relative abundance of super-Earths should remain constant after the first 100 Myrs. Photoevaporation models therefore predict no significant increase in the super-Earth population after the first 100-200 Myrs.

3.6.1.4 Planets in the gap

Since planets continue to lose mass over Gyr timescales, the core-powered mass-loss mechanism predicts that some planets will be still be losing mass today. Observationally these planets can be caught as they cross the radius valley, i.e. they maybe found inside the gap. In addition, atmospheric mass-loss may be directly detectable observationally.

3.6.2 Outlook

In this work we have shown how planetary evolution under the core-powered mass-loss mechanism can explain many of the observed features of the distribution of small, short-period exoplanets and their dependence on stellar properties. Although we have just summarized a list of observational test that should be able to distinguish between signatures imprinted on the exoplanet population by photoevaporation and core-powered mass-loss, we would like to emphasize that it appears almost inevitable that both processes take place to some extent. We therefore suspect that they both play a role in shaping the observed super-Earth and sub-Neptune populations. To that end, we plan to combine photoevaporation and core-powered mass-loss models in future work. Combining both of these mass-loss

mechanisms may turn out to be crucial for correctly inferring physical properties (e.g., core densities) of the exoplanet population from the observations.

CHAPTER 4

Caught in the Act: Core-powered Mass-loss Predictions for Observing Atmospheric Escape

[1]Past studies have demonstrated that atmospheric escape by the core-powered mass-loss mechanism can explain a multitude of observations associated with the radius valley that separates the super-Earth and sub-Neptune planet populations. Complementing such studies, in this work, we present a shortlist of planets that could be losing their atmospheres today if their evolution is indeed primarily dictated by core-powered mass-loss. We use Bayesian inference analysis on our planet evolution and mass-loss model to estimate the posteriors of the parameters that encapsulate the current state of a given planet, given their published masses, radii and host star properties. Our models predict that the following planets could be losing their atmospheres today at a rate $\gtrsim 10^7$ g/s at 50% confidence level: pi Men c, Kepler-60 d, Kepler-60 b, HD 86226 c, EPIC 249893012 b, Kepler-107 c, HD 219134 b, Kepler-80 e, Kepler-138 d and GJ 9827 d. As a by-product of our Bayesian inference analysis, we were also able to identify planets that most-likely harbor either secondary atmospheres abundant with high mean-molecular weight species, low-density interiors abundant with ices, or both. The planets belonging to this second category are WASP-47 e, Kepler-78 b, Kepler-10 b, CoRoT-7 b, HD 80653 b, 55 Cnc e and Kepler-36

[1]This chapter was previously published in similar form as Gupta, A. and Schlichting, H. E. 2021, MNRAS, 504, 4634-4648.

b. While the aforementioned lists are by no means exhaustive, we believe that candidates presented here can serve as useful input for target selection for future surveys and for testing the importance of core-powered mass-loss in individual planetary systems.

4.1 Introduction

Observational studies in the last decade have given us the opportunity to gain unprecedented insight into the origin of small exoplanets. Results from NASA's *Kepler* mission have revealed that around FGK stars, close-in planets between the sizes of Earth and Neptune are not just common (e.g. Fressin et al., 2013; Petigura et al., 2013), but that there are very few planets of intermediate sizes between 1.5 to 2.0 Earth radii ($R_\oplus$; e.g. Owen & Wu, 2013; Fulton et al., 2017).

This lack of intermediate sized planets or the bimodality in the size distribution of small planets, referred to as the 'radius valley' or 'radius gap', has since been corroborated by several studies (e.g. Van Eylen et al., 2018; Fulton & Petigura, 2018; Berger et al., 2018; Martinez et al., 2019; Berger et al., 2020a). Furthermore, the radius valley has now even been observed in the *K2* data (e.g. Zink et al., 2020) and for low mass stars (e.g. Cloutier & Menou, 2020; Van Eylen et al., 2021). Follow-up surveys seeking masses of these small planets have further revealed that there is an overlapping bimodality in their compositions as well (e.g. Marcy et al., 2014a; Rogers, 2015). Planets smaller than $\sim 1.6\ R_\oplus$ have higher densities that are consistent with rocky, Earth-like compositions (e.g. Dressing et al., 2015; Dorn et al., 2019; Bower et al., 2019) whereas planets larger than ~2 $R_\oplus$ have lower densities which suggests that these planets are Neptune-like and engulfed in H/He envelopes (e.g. Jontof-Hutter et al., 2016). It has thus been suggested that the radius valley is a transition regime from smaller, rocky planets, i.e. 'super-Earths' to the larger

planets with significant H/He envelopes, i.e. 'sub-Neptunes' (e.g. Rogers, 2015).

A multitude of mechanisms have been proposed to explain the radius valley (e.g. Owen & Wu, 2013; Ginzburg et al., 2018; Zeng et al., 2019; Lee & Connors, 2020) but only a few can explain the numerous observations pertinent to it (e.g. Fulton & Petigura, 2018; Van Eylen et al., 2018; Owen & Murray-Clay, 2018; Loyd et al., 2020; Berger et al., 2020a). Currently, the leading theory is that atmospheric mass-loss due to mechanisms such as photoevaporation and/or core-powered mass-loss leads to the observed bimodality in planet sizes and compositions (e.g. Owen & Wu, 2013; Lopez & Fortney, 2013; Ginzburg et al., 2018, Gupta & Schlichting 2019). Assuming that planets are typically born in protoplanetary gas disks and thus accrete H/He envelopes, photoevaporation and core-powered mass-loss studies argue that planets that subsequently lose their entire atmospheres are today's super-Earths whereas sub-Neptunes are those that survived with significant atmospheres.

Interestingly, studies have detected active atmospheric mass-loss from planets by looking for absorption signatures of different atomic and molecular species in their spectra. One of such signatures is the Lyman-alpha (Lyα) line which probes the presence of neutral hydrogen. This spectral line (doublet) corresponds to a wavelength of 121.6 nm and is due to excitation of an electron from the n=1 orbital to n=2 orbital (a Lyman series transition), where n is the principal quantum state of an atom. Vidal-Madjar et al. (2003) were the first to use this line to report the presence of an extended atmosphere around a planet - HD 209458 b - based on the fact that the transit depth they observed in Lyα was several times deeper than what was observed for an optical transit. Since excess absorption in Lyα has even been observed around smaller exoplanets such as GJ 436 b (Kulow et al., 2014; Ehrenreich et al., 2015; Lavie et al., 2017), GJ 3470 b (Bourrier et al., 2018), K2-18 b (dos Santos et al., 2020), Kepler-444 e and f (Bourrier et al., 2018) and GJ 9827 b (Carleo et al.,

2021). On the other hand, non-detections in Lyα have been reported for small exoplanets such as 55 Cnc e (Ehrenreich et al., 2012), HD 97658 b (Bourrier et al., 2017), GJ 1132 b (Waalkes et al., 2019) and pi Men c (García Muñoz et al., 2020). Similarly, studies have also looked for the H-alpha (Hα) line as a signature of extended atmospheres (e.g. Jensen et al., 2012). This 656.3 nm spectral line corresponds to the first Balmer series transition in hydrogen. So far, the Hα line has only been detected around giant planets such as HD 209458 b, HD 189733 b and WASP-33 b (e.g. Jensen et al., 2012; Yan & Henning, 2018). Among small exoplanets, a non-detection has been reported for GJ 9827 b (Carleo et al., 2021). Another excellent probe for atmospheric escape is the He 1083 nm triplet absorption feature (Seager & Sasselov, 2000; Oklopčić & Hirata, 2018). It has gained significant traction in the exoplanet community because it can overcome the primary shortcomings of the hydrogen lines such as absorption in the ISM and contamination from geocoronal emission. This spectral line is a consequence of a transition from the metastable 2^3S state - one of the spin states for helium electrons - to the 2^3P state by absorption at 1083 nm wavelength. Beginning with detection of atmospheric escape from WASP-107 b (Spake et al., 2018), it has already been used to detect mass-loss from various other planets including the warm Neptune GJ 3470 b (Ninan et al., 2020). To this date, however, the He 1083 nm line has not been detected around a planet less massive than GJ 4370 b. The small exoplanets for which non-detections have been reported include GJ 436 b (Nortmann et al., 2018), K2-100 b (Gaidos et al., 2020), GJ 1214 b (Kasper et al., 2020), HD 97658 b (Kasper et al., 2020), GJ 9827 d (Kasper et al., 2020; Carleo et al., 2021), GJ 9827 b (Carleo et al., 2021) and 55 Cnc e (Zhang et al., 2020).

As mentioned previously, if a planet's transit depths near the aforementioned wavelengths are much larger than what is observed in an optical transit, indicates that the planet has an extended atmosphere surrounding it. In other words, this implies that there are

a significant number of neutral hydrogen or metastable helium atoms at distances much greater than the photospheric radius of the planet. This is only plausible if the planet is losing its atmosphere. The depth of a transit primarily depends on the atmospheric profile or more specifically, the radial number density profile of the species being observed (e.g., neutral hydrogen for the Lyα line and metastable helium for the 1083 nm line), assuming reasonable knowledge of the cross-section of the absorbing species and the amount of stellar emission near the respective wavelengths. Inversely, if we know the transit depth of a planet, using an atmosphere profile model, we can estimate the number density profile of the species in question and thus, the mass-loss rate for the planet. A non-detection of excess absorption, however, doesn't necessarily imply that a planet is not undergoing atmospheric escape. Rather, it implies that the number density of the species being observed is below the detection limits and therefore, simply puts a constraint on the maximum mass-loss rate the planet could be undergoing.

Furthermore, while it is certainly the absorption of high energy stellar radiation by numerous hydrogen and helium atoms in the extended atmosphere that leads to the observed larger transit depths in Lyα, Hα and the Helium 1083 nm line - it is not clear if this atmospheric escape from small exoplanets is driven by photoevaporation or by core-powered mass-loss. In other words, even if a planet's evolution is dominated by core-powered mass-loss, it is certainly also subject to high energy radiation from its host star and the pertinent photochemistry.

To help elucidate which process may dominate the atmospheric mass-loss from small exoplanets and to help inform further observational surveys, we identify a set of ten planets that could be undergoing considerable atmospheric mass-loss today, if their evolution was dominated by core-powered mass-loss. To arrive at this list of candidates, we utilize the open-source code `dynesty` (Speagle, 2020) to construct a Bayesian inference model

around our core-powered mass-loss planet evolution code, previously used in Gupta & Schlichting (2019, 2020). This way, we are able to estimate planets' physical properties, such as bulk core compositions, atmospheric masses and mass-loss rates, that best explain their observed radii and masses, given their age and the bolometric flux they receives from their host stars.

This paper is structured as follows: In Section 4.2, we discuss our methodology for this work. We first give a review of how planets evolve under the core-powered mass-loss model, followed by a description of our Bayesian inference model and finally, we discuss the selection criteria for our sample of planets. Subsequently, we discuss our results in Section 4.3 that includes our list of planets which we recommend for follow-up observations and also discuss our results in the context of past observational and theoretical studies. We finally conclude this work in Section 4.4.

4.2 Methodology

In this section, we discuss our approach for estimating which of the observed planets could be undergoing significant mass-loss today under the core-powered mass-loss mechanism. To this end, we first discuss the core-powered mass-loss model in Section 4.2.1 and then our Bayesian inference model in Section 4.2.2. Finally, we lay out our sample selection criteria in Section 4.2.3.

4.2.1 Planet Evolution Model: Core-Powered Mass-Loss Mechanism

In the early phases of planet formation, as a core forms and grows by accreting solids, the gravitational binding energy of the accreting material gets converted into thermal energy.

This energy can be efficiently radiated away if the core forms after the protoplanetary gas disk has dispersed. However, if the accretion occurs in the presence of the gas disk, the core will accrete a H/He envelope from the surrounding nebula once its Bondi radius becomes larger than its physical radius. Once this envelope becomes optically thick, it will act as a 'thermal blanket' for the planet because the loss of heat from the core will then be limited by the thermal diffusion across the radiative-convective boundary of the envelope (e.g. Lee & Chiang, 2015; Ginzburg et al., 2016) - significantly increasing the cooling timescales of the underlying core. In other words, if a planet forms in the presence of a protoplanetary gas disk, it retains a significant fraction of its primordial energy from formation. In fact, the core temperature is likely set by the maximum temperature that permits the accretion of a H/He envelope which is roughly given by $T_c \sim GM_c\mu/k_BR_c$, where μ is the mean molecular mass of the atmosphere, k_B is the Boltzmann constant, G is the gravitational constant and M_c and R_c are the mass and radius of the planetary core, respectively. This implies typical core temperatures of 10^4 - 10^5 K for core masses ranging from the mass of Earth to Neptune.

Eventually, after the dispersal of the protoplanetary gas disk and the end of the spontaneous mass-loss phase/boil-off phase (Ginzburg et al., 2016; Owen & Wu, 2016), it is this primordial energy from planet formation together with the bolometric luminosity from the host star that can drive a Parker-type hydrodynamic outflow of the atmosphere (e.g. Parker, 1958) for small, close-in planets (Ginzburg et al., 2016, 2018; Gupta & Schlichting, 2019, 2020). We refer to this atmospheric mass-loss mechanism as core-powered mass-loss.

To model the evolution of a planet undergoing core-powered mass-loss, we assume that a typical planet with mass M_p and radius R_p consists of a molten and isothermal 'core' (mass M_c, radius R_c) that is surrounded by a H_2 atmosphere (mass M_{atm}, thickness ΔR). We assume that these planets have most of their mass in their cores such that $M_p \sim M_c$ and

that their cores and envelopes are thermally well coupled at the core-envelope interface. As in previous works, we adopt a two-layer model for the surrounding atmosphere with an inner convective and an outer radiative region (e.g. Piso & Youdin, 2014; Inamdar & Schlichting, 2015; Lee & Chiang, 2015). We model the convective region as adiabatic and the radiative region as isothermal, and refer to their interface as the radiative-convective boundary (R_{rcb}). Since the radiative region is close to isothermal, the atmospheric density decreases exponentially with radial distance and most of the atmospheric mass is thus contained in the convective region. Therefore, we assume that the observed radius of a planet, or its photospheric radius, $R_p \sim R_{rcb}$.

Since we are only modelling the atmospheric loss after the spontaneous mass-loss/boil-off phase (Owen & Wu, 2016; Ginzburg et al., 2016), we assume, following previous studies, $R_{rcb} \sim 2R_c$ as initial condition.

We account for gravitational compression of the planetary cores by assuming that their mass-radius relation is given by

$$M_c/M_\oplus = (R_c/R_\oplus)^4(\rho_{c*}/\rho_\oplus)^{4/3} \tag{4.1}$$

where ρ_{c*} is the density of a planet's core when scaled to Earth mass (e.g. Valencia et al., 2006; Seager et al., 2007; Fortney et al., 2007).

To track the evolution of such a planet undergoing core-powered mass-loss, we simultaneously evolve the total energy a planet has available for cooling (E_{cool}) and its atmospheric mass (M_{atm}) as a function of time by numerically solving the following equations:

$$E_{cool}(t + \mathrm{d}t) = E_{cool}(t) - L_{rcb}(t)\ \mathrm{d}t \text{ and} \tag{4.2}$$

$$M_{atm}(t + \mathrm{d}t) = M_{atm}(t) - \dot{M}_{atm}(t)\ \mathrm{d}t. \tag{4.3}$$

Here L_{rcb} is the luminosity of the planet at the radiative-convective boundary and $\dot{M}_{atm}$ is

the rate at which the planet is losing atmospheric mass. The former can be expressed as

$$L_{rcb} = \frac{64\pi}{3} \frac{\sigma T_{rcb}^4 R'_B}{\kappa \rho_{rcb}}, \tag{4.4}$$

where κ, T_{rcb} and ρ_{rcb} are the opacity, temperature and density at the radiative-convective boundary, σ is the Stefan-Boltzmann constant and $R'_B \equiv \frac{\gamma-1}{\gamma} G M_c \mu / (k_B T_{rcb})$, where γ and μ are the adiabatic index and molecular weight of the atmosphere and k_B is the Boltzmann constant. The mass-loss rate ($\dot{M}_{atm}$) that a planet experiences is assumed to be the smaller of the

1. the energy-limited rate ($\dot{M}^E_{atm}$), i.e., the mass-loss rate given by assuming all the cooling luminosity goes into driving atmospheric mass-loss,

$$\dot{M}^E_{atm} \simeq \frac{L_{int}(t)}{g R_c}, \tag{4.5}$$

   where $g = G M_c / R_c^2$ is the acceleration due to gravity evaluated at the core-atmosphere boundary, and

2. the Bondi-limited rate ($\dot{M}^B_{atm}$), i.e., the mass-loss rate that is dictated by the thermal velocity of the gas molecules at the Bondi radius,

$$\dot{M}^B_{atm} = 4\pi R_s^2 c_s \rho_{rcb} \exp\left(-\frac{G M_p}{c_s^2 R_{rcb}}\right), \tag{4.6}$$

   where $R_s = G M_p / 2c_s^2$ is the radius where the atmospheric outflow reaches sonic velocity and $c_s = (k_B T_{\rm eq}/\mu)^{1/2}$ is the isothermal speed of sound.

Due to this evolution, planets ultimately either lose all their atmospheres and become essentially naked cores and constitute the population of smaller planets below the radius valley, i.e. super-Earths, or retain some of their primordial H/He atmosphere and remain part the population of larger planets above the radius valley, i.e. sub-Neptunes (see, for

example, Figure 3 from Gupta & Schlichting (2020) and for further details Ginzburg et al. (2018) and Gupta & Schlichting (2019)).

4.2.2 Bayesian Inference Model

We use Bayesian inference analysis to estimate if a planet, given its mass, radius and its host star's properties, could be undergoing significant mass-loss today. Under the Bayesian framework, Bayes' theorem is used to estimate the posterior distribution $P(\mathbf{\Phi}|\mathbf{D}, M)$ of a set of parameters $\mathbf{\Phi}$ for a model M, given some data $\mathbf{D}$ and our prior knowledge of $\mathbf{\Phi}$, i.e.

$$P(\mathbf{\Phi}|\mathbf{D}, M) = \frac{P(\mathbf{D}|\mathbf{\Phi}, M) \times P(\mathbf{\Phi}|M)}{P(\mathbf{D}|M)}, \tag{4.7}$$

where $P(\mathbf{D}|\mathbf{\Phi}, M)$ quantifies the likelihood of observing the data $\boldsymbol{D}$ given the model M and the parameters $\mathbf{\Phi}$, i.e. it's the likelihood distribution. $P(\mathbf{\Phi}|M)$ is known as the prior distribution and signifies our prior knowledge of the parameters $\mathbf{\Phi}$ that we input in the model M. $P(\mathbf{D}|M)$, which can be expressed as

$$P(\mathbf{D}|M) = \int_{\forall \mathbf{\Phi}} P(\mathbf{D}|\mathbf{\Phi}, M) \times P(\mathbf{\Phi}|M)\ \mathrm{d}\mathbf{\Phi}, \tag{4.8}$$

embodies our confidence in the model M given the observations.

In the context of this work,

1. M is our planet evolution model based on the core-powered mass-loss mechanism as discussed in Section 4.2.1,

2. $\mathbf{D} = \{..., \mathrm{D}_i, ...\}$ corresponds to the observed properties of a planet and its host star, namely, the observed radius (R_p), mass (M_p) and insolation flux (S_p) of a given planet and the estimated age of its host star (τ_*), and

3. $\mathbf{\Phi} = \{..., \Phi_i, ...\}$ includes all the input parameters for our model M such as a planet's primordial atmosphere mass fraction ($f_{\rm initial}$), bulk density of the core scaled to an Earth mass (ρ_{c*}), M_p, R_p, S_p and τ_*.

For any observed property D_i, we assume that its uncertainties and thus its likelihood are Gaussian in nature, centered at μ_i (= the nominal or measured value) with a standard deviation σ_i (= (upper error limit + lower error limit)/2). The total likelihood, given $\mathbf{\Phi}$, is then the product of the individual likelihoods corresponding to each D_i. For all parameters $\in \mathbf{\Phi}$, except for ρ_{c*}, we assume uniform priors. For ρ_{c*}, we assume a Gaussian distribution centered at $\mu_{\rho_{c*}} = 5$ g/cm^3 with a $\sigma_{\rho_{c*}} = 1$ g/cm^3. This is motivated by recent mass and radius measurements of rocky planets (e.g. Dressing et al., 2015; Bower et al., 2019; Dorn et al., 2019), geochemical studies of white-dwarf pollution (e.g. Doyle et al., 2019) and previous planet population studies involving evolution under core-powered mass-loss (Gupta & Schlichting, 2020). In addition, this assumption is also consistent with the results of photoevaporation studies (e.g. Rogers & Owen, 2020). Nevertheless, we experiment with other values for $\{\mu_{\rho_{c*}}, \sigma_{\rho_{c*}}\}$ too and discuss this later in Section 4.3.1.

To compute the resulting $P(\mathbf{\Phi}|\mathbf{D}, M)$, we use the open-source code `dynesty` (Speagle, 2020) which uses a Dynamic Nested Sampling algorithm to estimate posteriors and evidences (Skilling, 2004, 2006; Higson et al., 2019; Feroz et al., 2009). Therefore, given the planet and host star observations $\mathbf{D}$ and our evolution model M, `dynesty` allows us use the Bayes' theorem to estimate the distribution of the most likely values that planet parameters, $\mathbf{\Phi} = \{f_{\rm initial}, \rho_{c*}, ...\}$, can have and their co-variances (see for e.g. Figure 4.2). Knowledge of planet parameters such as the primordial atmospheric mass-fraction ($f_{\rm initial}$) and bulk composition (ρ_{c*}) allows us to then determine the planet's current atmospheric mass-fraction (f_{final}) and thus its current atmospheric mass-loss rate ($\dot{M}_{\rm atm}$).

4.2.3 Sample Selection

On August 12, 2020, we collected all the planets from the NASA Exoplanet Archive that have masses below $20M_{\oplus}$ at 2σ confidence level and an age estimate for their host stars. We then further restricted the sample to planets for which mass measurements have uncertainties lower than 30%.

Furthermore, we removed planets with host star masses below 0.5 $M_{\odot}$, because to accurately model the evolution of planets around such low-mass host stars one needs to take into account their Gyr-long pre-main-sequence evolution and the related bolometric luminosity changes (e.g. Ramirez & Kaltenegger, 2014), which is beyond the scope of this paper. After all these cuts, we were left with a sample of 78 planets.

Most of the Kepler planets from this sample are also present in a recently published *Gaia-Kepler* Stellar Catalogue by Berger et al. (2020b,a) that has homogeneously-derived stellar and planetary properties. For the common *Kepler* planets, we thus updated all the stellar and planetary properties, except planet mass, from Berger et al. (2020b,a).

4.3 Results

Below we identify planetary candidates for which we predict that their atmospheric loss could be observable today if their evolution has been dominated by core-powered mass-loss. In addition, we provide a list of planetary candidates that likely either have secondary atmospheres or interiors with significant ice-fraction by mass, or both.

In our numerical simulations, we assume that a planet has become a super-Earth when $f_{\rm final} = M_{atm}/M_c < 10^{-10}$ or $\Delta R/R_c < 10^{-3}$.[2] For these planets, we set $f_{final} = 0$,

[2]Note that the typical uncertainties in planet radii measurements are much larger at $\sim$ 5% (Fulton &

$\Delta R/R_c = 0$ and $\dot{M}_{atm} = 10^{-10}$ g/s. Giving super-Earths a tiny, but none-zero, mass-loss rate allows us to include it in the mass-loss rate posterior plots which have logarithmic scaling. We confirmed that our results do not depend on the exact choice of our chosen cut-offs.

4.3.1 Core-powered Mass-loss Predictions for Atmospheric escape observations

We run our hybrid planet evolution-Bayesian inference model, for each of the 78 planets in our sample. Our planet evolution model neglects an atmosphere's self-gravity which is an appropriate assumption only for atmosphere mass-fractions $\lesssim 0.2$ (e.g. Piso & Youdin, 2014; Ginzburg et al., 2016). We therefore exclude from our list all 34 planets for which our evolution model predicts median initial atmosphere mass fractions > 0.2. Since we are trying to determine which planets might be undergoing significant mass-loss today, we also exclude all planets for which we predict current median mass-loss rates of $\lesssim 10^7$ g/s. Finally, we decided not to include Kepler-99 b because, even though it satisfies the above two criteria, it is very sensitive to the prior we choose for ρ_{c*}. We are thus left with a list of ten planets consisting of: pi Men c, Kepler-60 d, Kepler-60 b, HD 86226 c, EPIC 249893012 b, Kepler-107 c, HD 219134 b, Kepler-80 e, Kepler-138 d, and GJ 9827 d. We show these planets as blue circles in planet size-orbital period space and planet size-insolation flux space in Figure 4.1. In addition, we present the relevant planet and host star parameters in Table 4.1 and our estimated mass-loss rates in Table 4.2. We now discuss our results for each listed planet in detail.

pi Men c: As evident from Table 4.2, pi Men c is one of the top planetary candidates

Petigura, 2018)

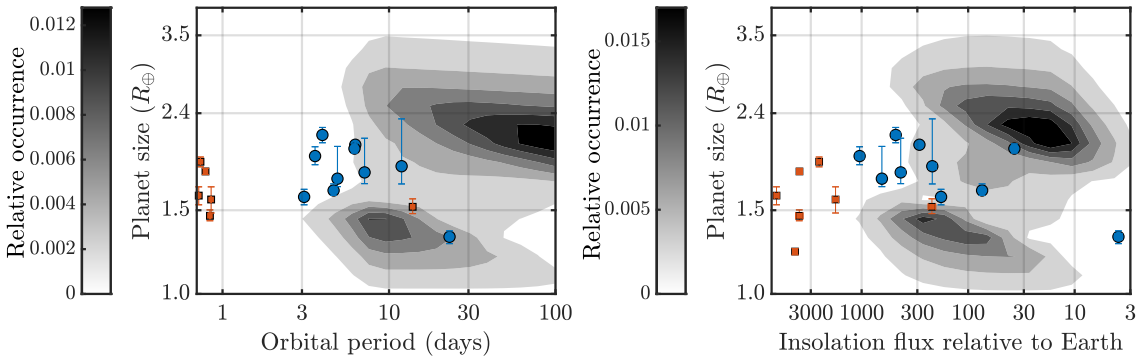

Figure 4.1: Location of planets for which we predict that they could be undergoing considerable atmospheric mass-loss today (●) in the planet size-orbital period space (left) and the planet size-insolation flux space (right). In addition, we also show planets which we identified to likely have interiors with a significant ice-fraction, or a secondary atmosphere, or both (■). The planet size occurrence contours are from a previous core-powered mass-loss study (Gupta & Schlichting, 2020) which reproduced the radius valley observed around FGK stars (Fulton & Petigura, 2018). These plots show that the planets that could be losing their atmospheres today (shown in blue) lie in the radius valley.

Planet	τ_* (Gyr)	M_* ($M_\odot$)	S_p ($S_\oplus$)	R_p ($R_\oplus$)	M_p ($M_\oplus$)	References
pi Men c	$5.20^{+1.10}_{-1.10}$	$1.02^{0.03}_{0.03}$	$282.66^{-12.42}_{+12.42}$	$2.06^{+0.03}_{-0.03}$	$4.52^{+0.81}_{-0.81}$	Gandolfi et al. (2018)
Kepler-60 d	$4.80^{+2.02}_{-1.37}$	$1.13^{+0.07}_{-0.08}$	$217.11^{-18.63}_{+16.64}$	$1.86^{+0.48}_{-0.15}$	$3.90^{+0.70\dagger}_{-0.60}$	Berger et al. (2020b,a)
Kepler-60 b	$4.80^{+2.02}_{-1.37}$	$1.13^{+0.07}_{-0.08}$	$429.50^{-36.87}_{+32.93}$	$1.80^{+0.32}_{-0.10}$	$3.70^{+0.60\dagger}_{-0.60}$	Berger et al. (2020b,a)
HD 86226 c	$4.60^{+3.70}_{-2.70}$	$1.02^{+0.06}_{-0.07}$	$481.92^{-42.20}_{+42.20}$	$2.16^{+0.08}_{-0.08}$	$7.25^{+1.19}_{-1.12}$	Teske et al. (2020)
EPIC 249893012 b	$9.00^{+0.50}_{-0.60}$	$1.05^{+0.05}_{-0.05}$	$1044.23^{-88.10}_{+88.10}$	$1.95^{+0.09}_{-0.08}$	$8.75^{+1.09}_{-1.08}$	Hidalgo et al. (2020)
Kepler-107 c	$3.23^{+1.27}_{-0.94}$	$1.25^{+0.05}_{-0.06}$	$645.38^{-46.28}_{+48.35}$	$1.75^{+0.30}_{-0.07}$	$9.39^{+1.77*}_{-1.77}$	Berger et al. (2020b,a)
HD 219134 b	$11.00^{+2.20}_{-2.20}$	$0.81^{+0.03}_{-0.03}$	$179.59^{-5.51}_{+5.51}$	$1.60^{+0.06}_{-0.06}$	$4.74^{+0.19}_{-0.19}$	Gillon et al. (2017)
Kepler-80 e	$10.74^{+6.09}_{-6.70}$	$0.71^{+0.03}_{-0.03}$	$73.96^{-4.86}_{+5.36}$	$1.65^{+0.05}_{-0.04}$	$4.13^{+0.81\P}_{-0.95}$	Berger et al. (2020b,a)
Kepler-138 d	$10.81^{+6.16}_{-6.96}$	$0.54^{+0.01}_{-0.01}$	$3.88^{-0.32}_{+0.34}$	$1.32^{+0.04}_{-0.04}$	$1.17^{+0.30\S}_{-0.30}$	Berger et al. (2020b,a)
GJ 9827 d	$10.00^{+2.00}_{-5.00}$	$0.61^{+0.02}_{-0.02}$	$36.83^{-1.86}_{+1.86}$	$2.02^{+0.05}_{-0.04}$	$4.04^{+0.82}_{-0.84}$	Rice et al. (2019)

Table 4.1: List of planets that could be undergoing mass-loss today and their observed parameters: host star's age (τ_*) and mass (M_*), planet's insolation flux (S_p), radius (R_p), mass (M_p) and density when scaled to an Earth mass (ρ_{p*}). Values are reported with 1 σ errors. The last column lists the references from where all the planet and host-star properties are taken from, unless noted otherwise below. Mass estimates for the Kepler planets were taken from †Hadden & Lithwick (2017), *Bonomo et al. (2019), ¶MacDonald et al. (2016) and §Almenara et al. (2018).).

Planet	$\dot{M}_{atm}$ [$\log_{10}$(g/s)]		
	$\mu_{1/2}$ (50^{th}-percentile)	$[\mu_{1/2}-\sigma, \mu_{1/2}+\sigma]$	$[\mu_{1/2}-2\sigma, \mu_{1/2}+2\sigma]$
pi Men c	9.40	[8.98, 9.69]	[7.96, 9.90]
Kepler-60 d	8.85	[-10, 9.77]	[-10, 10.18]
Kepler-60 b	8.83	[-10, 9.52]	[-10, 9.96]
HD 86226 c	8.21	[7.14, 9.20]	[4.76, 9.80]
EPIC 249893012 b	8.08	[5.51, 8.54]	[-10, 9.02]
Kepler-107 c	7.69	[-10, 8.45]	[-10, 9.13]
HD 219134 b	7.59	[-10, 7.94]	[-10, 8.22]
Kepler-80 e	7.44	[5.99, 8.15]	[-10, 8.83]
Kepler-138 d	7.24	[6.21, 8.21]	[-10, 8.71]
GJ 9827 d	6.72	[3.33, 8.23]	[-0.25, 9.57]

Table 4.2: Core-powered mass loss predictions for planets undergoing mass-loss today. The three columns of mass-loss rates correspond to the median (50^{th}-percentile, $\mu_{1/2}$) and the range spanning 1 σ and 2 σ around $\mu_{1/2}$, respectively.

that could be undergoing mass-loss today. Figure 4.2 is a corner plot for pi Men c generated using our hybrid planet evolution-Bayesian inference model described in Section 4.2. It shows posterior distributions of the different parameters that characterize the evolution of this planet given our model. Specifically, the sub-plots in Figure 4.2 show the covariance and one-dimensional posterior distributions of planet mass (M_p), age (τ_*), initial and final atmosphere mass fractions ($f_{initial}$ and f_{final}), planet radius (R_p), mass-loss rate ($\dot{M}_{atm}$), density of the planet's core when scaled to Earth mass (ρ_{c*}) and insolation flux with respect to Earth (S_p).

Situated only 18 parsecs away, pi Men c has a bright G0 V host star with an apparent magnitude (V) = 5.65 mag which makes it especially suitable for follow up observations (Gandolfi et al., 2018). This planet has thus already been a subject of several studies and proposals. García Muñoz et al. (2020) recently reported non-detection of Lyα absorption for this planet. These authors also used a photoevaporation model to compute mass-loss rates for pi Men c and found estimates of $(4 \times 10^9 - 10^{10})$ g/s (see also, Shaikhislamov et al., 2020). This is a higher mass-loss rate than estimated for GJ 436b which does show Lyα absorption (e.g. Kulow et al., 2014). García Muñoz et al. (2020) thus argued that the atmosphere is likely not hydrogen-dominated and should rather have substantial amounts of heavier molecules like CO_2 and H_2O. An atmosphere that is not hydrogen-dominated, however, is unlikely to be consistent with pi Men c's low density.

As shown in Figure 4.2, our core-powered mass-loss model predicts mass-loss rates of 9×10^7 g/s to 8×10^9 at 95% confidence level. Since our mass-loss rates span a lower range than the predictions from photo-evaporation models, they may offer an explanation for the non-detection of Lyα absorption. In addition, our results imply that current observations do not necessarily preclude the possibility of pi Men c having a hydrogen-dominated atmosphere.

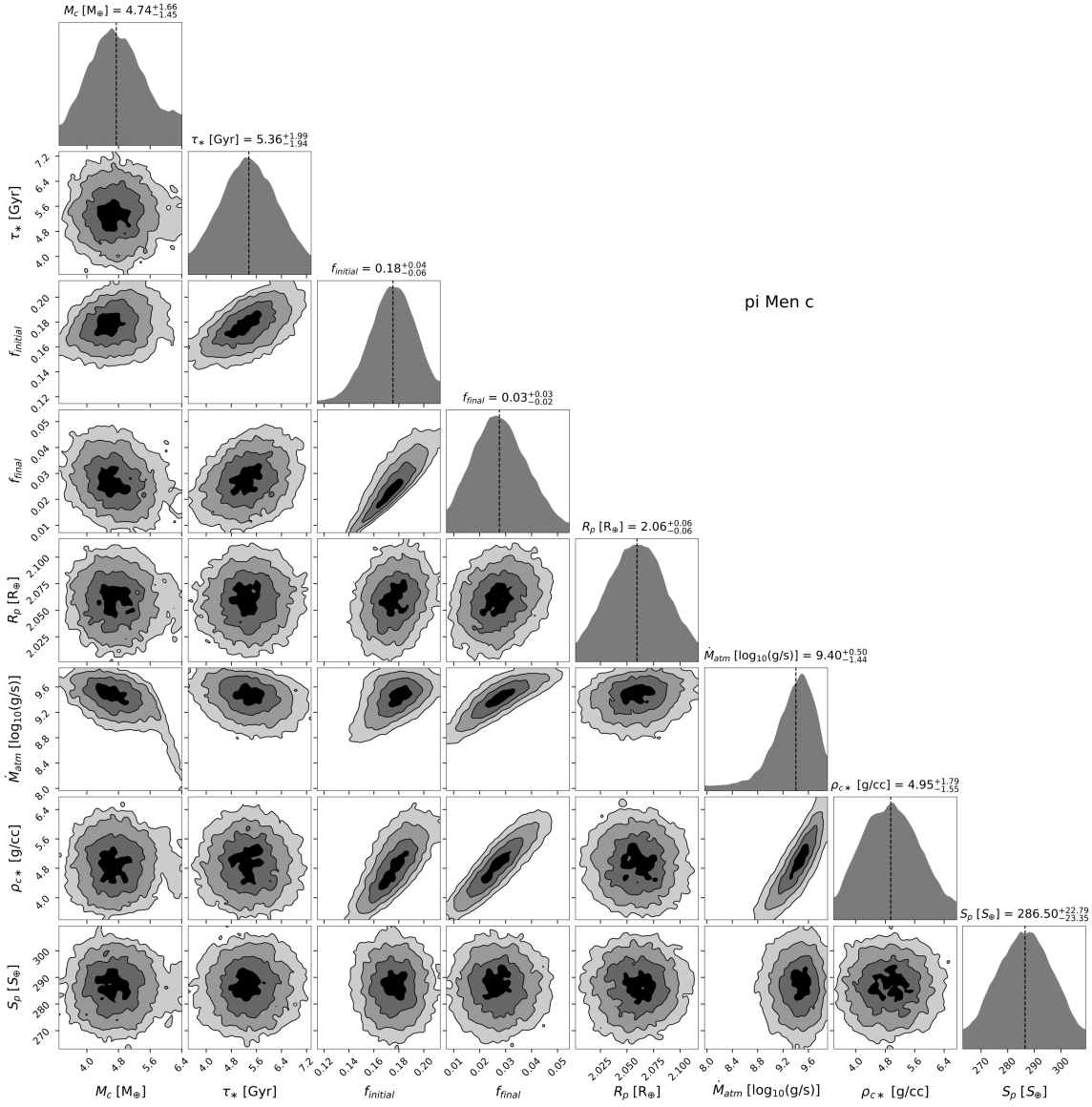

Figure 4.2: Corner plot for pi Men c generated using our hybrid planet evolution-Bayesian inference model (*continued next page*).

Figure 4.2: Corner plot for pi Men c generated using our hybrid planet evolution-Bayesian inference model. This figure shows one-dimensional posterior probability distributions of different parameters that characterize the evolution of pi Men c and their covariances. The parameters shown are planet mass (M_p), age (τ_*), initial and final atmosphere mass fractions ($f_{initial}$ and f_{final}), planet radius (R_p), mass-loss rate ($\dot{M}_{atm}$), density of the planet's core when scaled to Earth mass (ρ_{c*}) and insolation flux received by the planet scaled to Earth (S_p). All parameters are reported with 2 σ errors and vertical dashed lines denote the median values. The mass-loss rate posterior distributions show that this planet has a median mass-loss rate of $\sim 2.5 \times 10^9$ g/s. Our analysis thus places pi Men c in the list of planets that could be losing their atmospheres today at a considerable rate.

Similar to Figure 4.2, Figures 4.3 to 4.5 show the corner plots GJ 9827 d, HD 219134 b and HD 86226 c. In addition, Figure 4.6 shows the mass-loss rate posteriors for all the other planets mentioned in Table 4.2. Among the listed planets, apart from pi Men c, atmospheric observations have only been published for GJ 9827 d. There are, however, multiple theoretical studies that have investigated the existence and nature of atmospheres on GJ 9827 d and HD 219134 b.

GJ 9827 d: Part of a three planet system situated 30 parsecs away and orbiting a K6 V star with V = 10.4 mag, GJ 9827 d is another suitable target for atmospheric mass-loss observations (Niraula et al., 2017; Rodriguez et al., 2018). Recent studies by Kasper et al. (2020) and Carleo et al. (2021) have reported non-detection of helium in the upper atmospheres of GJ 9827 d. Carleo et al. (2021) also reported a non-detection in Hα. Using a MESA-based planet evolution model that includes mass-loss via photoevaporation (e.g.

Malsky & Rogers, 2020), Kasper et al. (2020) found that this non-detection is inconsistent with predicted mass-loss rate estimates of the order of $\sim 10^9$ g/s from photoevaporation. Similarly, Carleo et al. (2021) predicted even higher mass-loss rates from photoevaporation of about 5.1×10^{10} g/s.

In contrast, assuming planet evolution and atmospheric loss is dominated by core-powered mass-loss, we predict that the mass-loss rate could be much lower. Specifically, we find a median mass-loss rate of 5×10^6 g/s with a 95% confidence interval of ranging from close to zero to $\sim 4 \times 10^9$ g/s (for details, see Table 4.2 or Figure 4.3). The non-detection of the He 1083 nm triplet feature or Hα absorption is therefore consistent with predictions from our core-powered mass-loss model.

It is important to note that, as shown in Figures 4.2 to 4.5, atmospheric mass-loss rates are especially sensitive to the uncertainties in planet mass measurements. This is particularly apparent in the covariance plot showing the correlation between mass-loss rate and planet mass for GJ 9827 d. In this specific example, mass-loss rates vary by ~ 10 orders-of-magnitude for planet masses within 2σ of the median (see Figure 4.3). This extreme sensitivity of the mass-loss rate on planet mass is a consequence of the fact that, given the mass, radius, age and insolation flux received by GJ 9827 d and others, the mass-loss rates are in the Bondi-limited regime (see Section 4.2.1). In this regime, the mass-loss rate has an exponential dependence on planet mass (see Equation (4.6)) and scales as

$$\dot{M}_{atm} \propto \exp\left(-\frac{GM_p}{c_s^2 R_p}\right) \propto \exp\left(-\zeta M_c S_p^{-1/4} R_p^{-1}\right), \tag{4.9}$$

where ζ is a constant. The last expression shows that the mass-loss rate, for a given insolation flux and planet size, decreases exponentially with increasing planet mass and thus explains the trends in the relevant covariance plots in Figures 4.2 to 4.5. Therefore, one of the best ways to improve mass-loss estimates for any of the prime candidate planets, is to

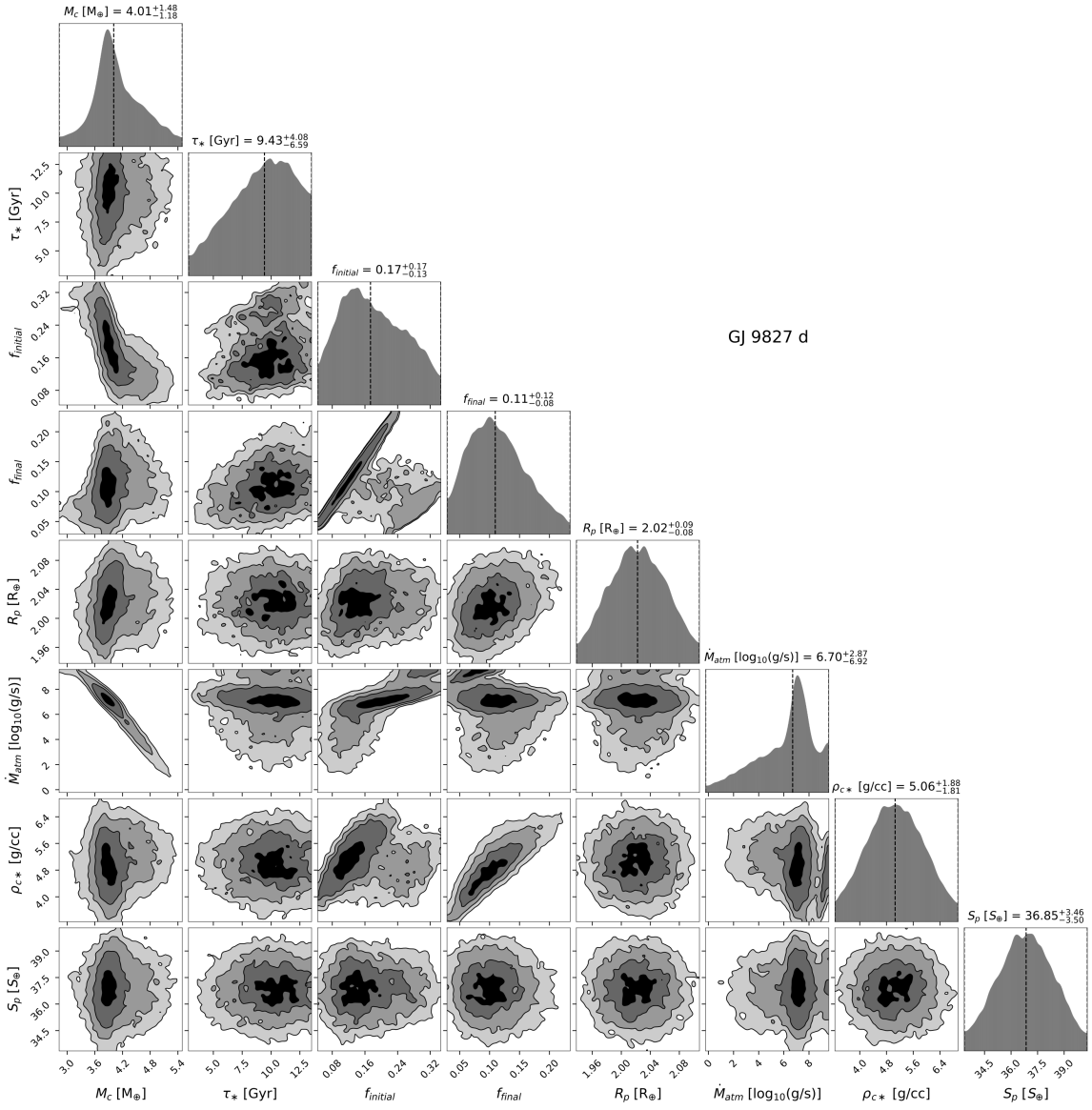

Figure 4.3: Corner plot for GJ 9827 d generated using our hybrid planet evolution-Bayesian inference model; similar to Figure 4.2 (*continued next page*).

Figure 4.3: Corner plot for GJ 9827 d generated using our hybrid planet evolution-Bayesian inference model; similar to Figure 4.2. All parameters are reported with 2 σ errors and vertical dashed lines denote the median values. The mass-loss rate posterior shows that the 95% confidence interval for mass-loss rate is $\sim[0, 4 \times 10^9]$ g/s with a median at $\sim 5 \times 10^6$ g/s. Our analysis thus places GJ 9827 d among planets that make interesting targets for observing atmospheric mass-loss. The covariance plot of mass-loss rate and planet mass shows how sensitive the atmospheric mass-loss rate is to the uncertainties in the planet mass measurements. Mass-loss rate estimates for GJ 9827 d vary by $\sim$ 10 orders of magnitude for planet masses within 2σ of the median.

get better constraints on their masses.

HD 219134 b: This planet is part of a six planet system orbiting a bright (V = 5.57 mag) K3 V star that is six parsecs away (Vogt et al., 2015; Motalebi et al., 2015). With host star characteristics suitable for observations (e.g. Gillon et al., 2017) and a high likelihood for undergoing mass-loss, according to our analysis, this planet is another excellent target for atmospheric mass-loss observations with a predicted mass-loss rate of $\gtrsim 10^8$ g/s at 50^{th}-percentile.

Interestingly, our analysis finds that mass-loss rate posteriors for HD 219134 b, and a number of other planets, are double-peaked, i.e. they peak at $\sim$ 0 g/s and $\gtrsim 10^7$ g/s. While for pi Men c we estimate a mass-loss rate that is $\gtrsim 10^8$ g/s at 95% confidence level, the same can't be said for most of the other candidates; see Figures 4.4 and 4.6. Even though all the candidates are robust to our choice of ρ_{c*}, as we later discuss, the double-peaked distribution signifies that, although much less probable, there is another

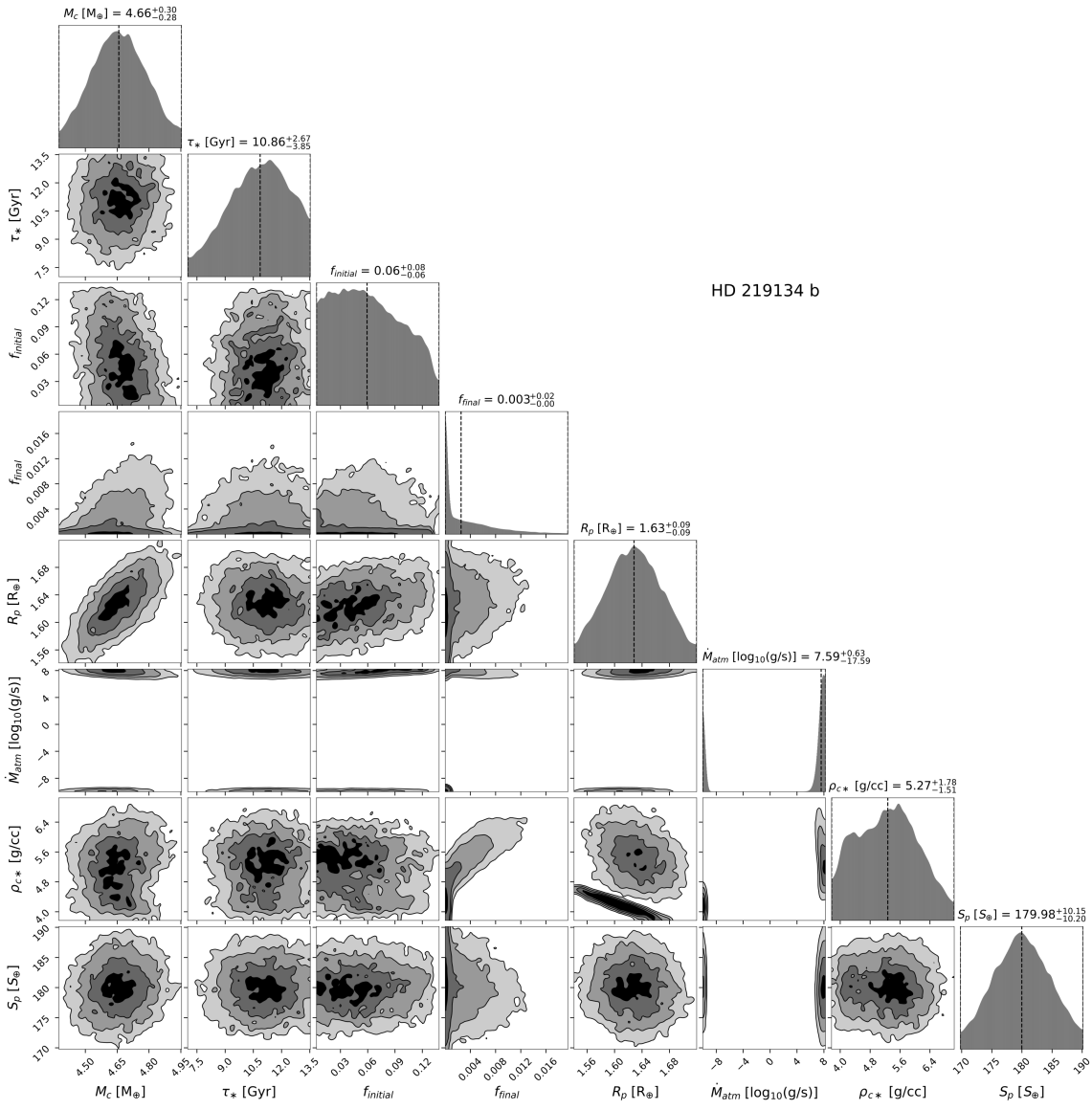

Figure 4.4: Corner plot for HD 219134 b generated using our hybrid planet evolution-Bayesian inference model; similar to Figures 4.2 and 4.3 (*continued next page*).

Figure 4.4: Corner plot for HD 219134 b generated using our hybrid planet evolution-Bayesian inference model; similar to Figures 4.2 and 4.3. All parameters are reported with 2σ errors and vertical dashed lines denote the median values. As with pi Men c and GJ 9827 d, our analysis places HD 219134 b in the category of planets that could be undergoing considerable atmospheric escape today but, unlike these planets, HD 219134 b has a double-peaked mass-loss posterior distribution with local maxima at $\sim$ 0 g/s and $\gtrsim 10^7$ g/s. The peak in the mass-loss rate at $\gtrsim 10^7$ g/s is consistent with GJ 9827 d having an Earth-like core with a significant hydrogen envelope. On the other hand, the peak at $\sim$ 0 g/s signifies that there is a $\sim$21% likelihood that the planet is not losing any atmosphere and rather has a secondary, high-mean molecular weight atmosphere, a low density, icy interior, or both (see ρ_{c*} posteriors which show two peaks roughly centered at 4 and 5.5 g/cm^3).

physically motivated solution for the composition of some of the listed planets, with bulk core densities significantly lower than Earth and/or a higher mean-molecular weight envelope (see Figures 4.4 and 4.6). That this second solution corresponds to low core densities in our model can be seen in the ρ_{c*} posteriors in Figure 4.4, which show peaks around 4 and 5.5 g/cm^3. Planets that exhibit this behavior, like HD 219134 b, are typically near the lower edge of the radius valley.

Our results therefore indicate that HD 219134 b's current state is consistent with both - having a hydrogen atmosphere and with having a low density interior (e.g. significant ice-fraction by mass or a secondary atmosphere, or both). Despite these two distinct solutions, we find that it is much more likely that HD 219134 b has a hydrogen envelope and that it therefore should be undergoing atmospheric mass-loss today with predicted rates of $\gtrsim 10^8$ g/s at 50^{th}-percentile

Past theoretical studies that examine mass-loss due to photoevaporation have concluded that HD 219134 b is most likely not hydrogen-dominated because it should have lost its atmosphere by this day and therefore, should rather have a secondary atmosphere, an icy interior or a magma ocean (Dorn & Heng, 2018; Kubyshkina et al., 2018; Ligi et al., 2019). While no published study has yet attempted observing atmospheric mass-loss from HD 219134 b, it appears to be an especially interesting target because photoevaporation and core-powered mass-loss studies make opposite predictions for this planet. Specifically, detecting atmospheric loss from HD 219134 b would provide direct evidence for core-powered mass-loss driving this out-flow.

HD 86226 c: A recent discovery around a nearby, bright G1V star with V = 7.93 mag, HD 86226 c is another excellent target for observing atmospheric escape (Teske et al.,

2020). As shown in Figure 4.5, our core-powered mass-loss model predicts mass-loss rates between 6×10^4 g/s to 6×10^9 g/s (95% confidence interval).

Kepler-60 d, Kepler-60 b, EPIC 249893012 b, Kepler-107 c, Kepler-80 e, and Kepler-138 d: At the time of writing, to the best of our knowledge, there are no published studies that perform theoretical or observational analysis to determine atmospheric mass-loss from these planets. As shown in Figure 4.6 and Table 4.2, our results predict that these planets are likely undergoing considerable atmospheric mass-loss. Host stars of these planets are unfortunately dimmer: EPIC 249893012 with V = 11.4 mag (Hidalgo et al., 2020), Kepler-107 c (Rowe et al., 2014), Kepler-138 with V = 12.9 mag (Rowe et al., 2014), Kepler-60 with V = 14.5 mag (Steffen et al., 2013; Hadden & Lithwick, 2014) and Kepler-80 with V = 15.0 mag (Muirhead et al., 2012). Nonetheless, for completeness, we give the mass-loss rates of this set of planets in Table 4.2 and Figure 4.6 with the hope that their characterization may come within reach one day with future facilities.

4.3.1.1 Sensitivity of mass-loss results to the choice of the exact ρ_{c*} prior

To estimate the posterior distributions of planet and stellar properties that characterize a planet's evolution and mass-loss, we assumed that the prior for ρ_{c*} is a Gaussian distribution with a mean $\mu_{\rho_{c*}}$ = 5 g/cm^3 and a standard deviation $\sigma_{\rho_{c*}}$ = 1 g/cm^3. This assumption is motivated by previous observational and theoretical studies (e.g. Bower et al., 2019; Doyle et al., 2019; Gupta & Schlichting, 2020; Rogers & Owen, 2020). Furthermore, our Bayesian inference model lets us account for the modelling degeneracy between the density of a planet's core and (non-)existence of a hydrogen atmosphere (e.g. Rogers & Seager, 2010; Zeng et al., 2019; Mousis et al., 2020). Nevertheless, to check if our best planetary

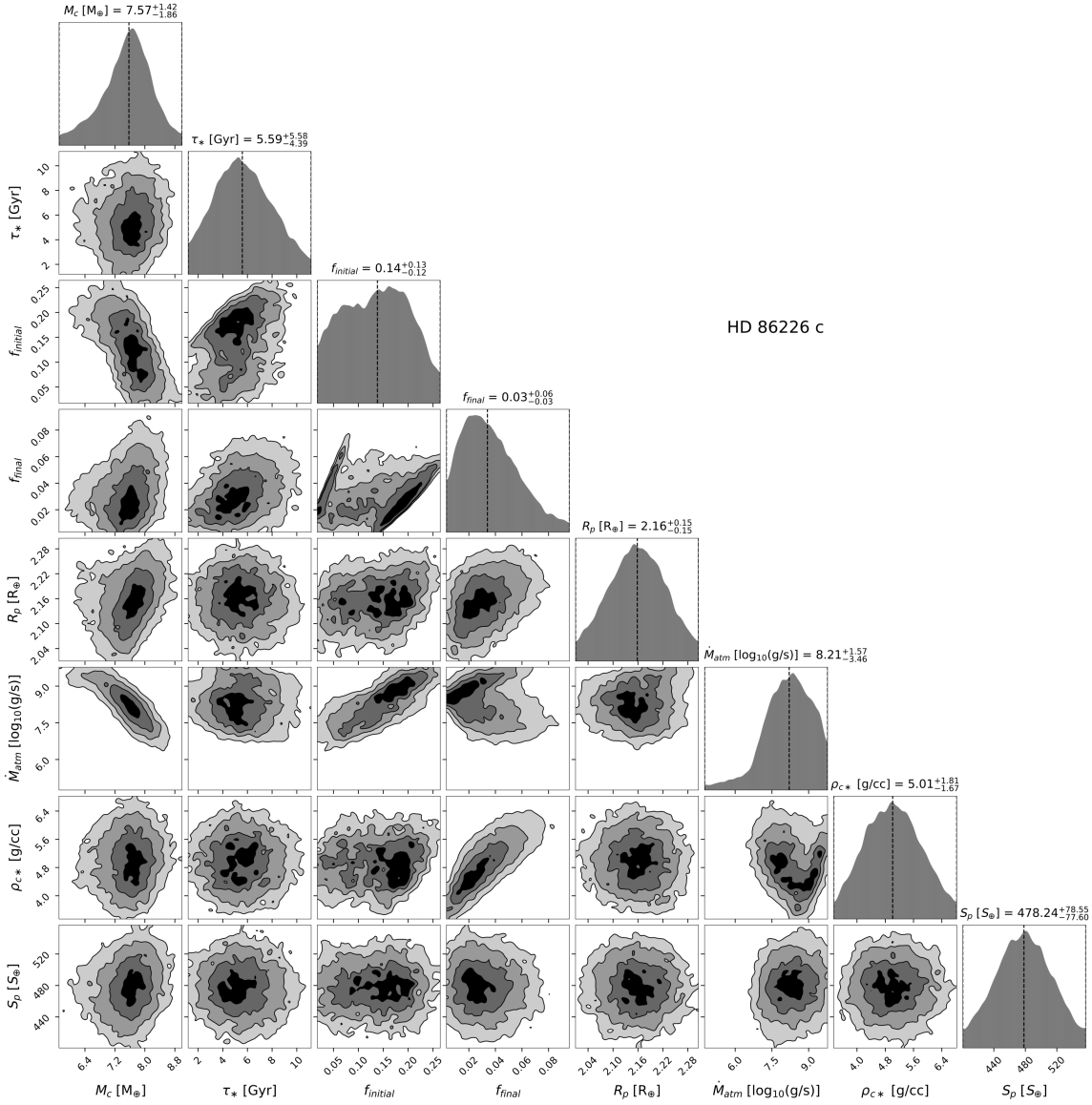

Figure 4.5: Corner plot for HD 86226 c generated using our hybrid planet evolution-Bayesian inference model; similar to Figures 4.2 to 4.4. All parameters are reported with 2 σ errors and vertical dashed lines denote the median values. The mass-loss rate posterior shows that the planet has a median mass-loss rate of $\sim 1.6 \times 10^8$ g/s and thus, HD 86226 c is another excellent candidate for observing atmospheric mass-loss today.

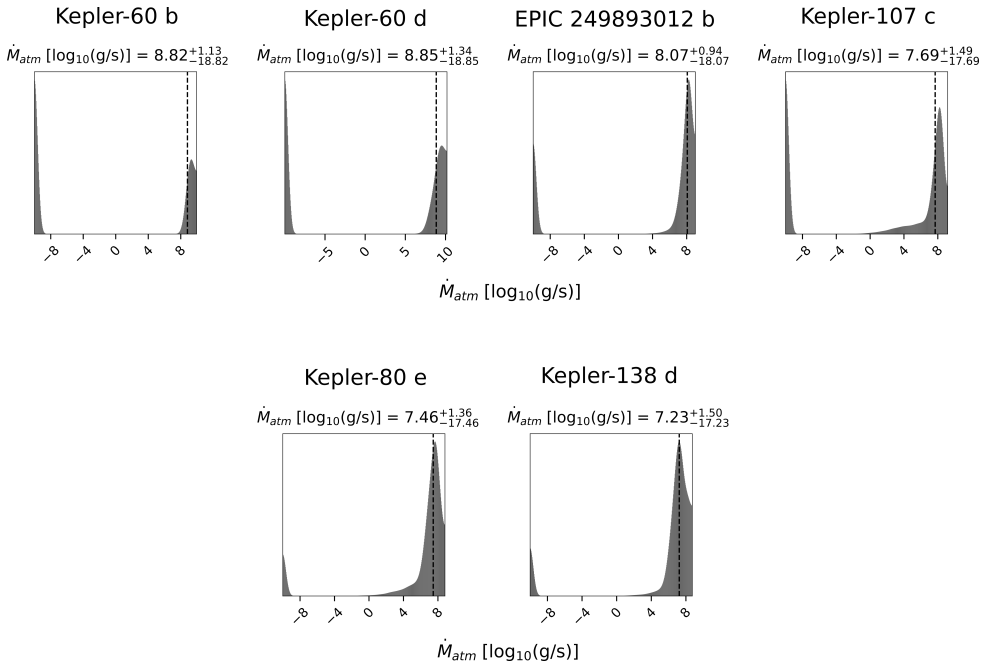

Figure 4.6: Mass-loss rate posterior distributions for planets that, in addition to pi Men c, GJ 9827 d, HD 219134 b and HD 86226 c, could be experiencing considerable atmospheric escape at this moment: $\gtrsim 10^7$ g/s at 50^{th}-percentile. Mass-loss rates are reported with 2 σ errors and vertical dashed lines denote the median values. The two-peaked nature of mass-loss rate distributions for these planets suggests that, like HD 219134 b, there is a small likelihood that these planets might not be undergoing atmospheric escape and instead, have an atmosphere abundant with heavy molecular weight species, interiors with a significant amount of ices, or both. We find that the probability of this alternate scenario is $\sim$ 32% for Kepler-60 d, $\sim$ 42% for Kepler-60 b, $\sim$ 1% for EPIC 249893012 b, $\sim$ 14% for Kepler-107 c, $\sim$ 5% for Kepler-80 e and $\sim$ 6% for Kepler-138 d.

candidates for mass-loss are sensitive to the exact choice of prior for ρ_{c*}, we repeated our analysis assuming that this prior is a Gaussian distribution with $\mu_{\rho_{c*}}$ = 4, 5 and 5.5 g/cm^3 and with standard deviations $\sigma_{\rho_{c*}}$ equal to 1 and 2 g/cm^3. We find that except for Kepler-60 b, all the listed planets yield mass-loss rates similar to those reported in Table 4.2. For Kepler-60 b, when $\mu_{\rho_{c*}}$ = 4 g/cm^3, the posterior for ρ_{c*} indicates that the planet is more likely to have a significant ice-fraction by mass and/or a secondary atmosphere abundant with high molecular weight gases. Planets that are highly likely to fall into this category are discussed in the next section.

4.3.1.2 Consequence of mass-fractionation on estimating mass-loss rates

In this work, while we do not explicitly account for any mass-fractionation during atmospheric escape, we did repeat our analysis to gauge its impact on the evolution of our top planet candidates. Photoevaporation studies have shown that mass-fractionation can be significant for planets that have been losing their atmospheres for several Gyr (e.g. Hu et al., 2015; Malsky & Rogers, 2020). Using the mass-fractionation prescription described in Biersteker & Schlichting (2021), we find that, for our top planet candidates, the mean molecular weight of the atmospheres only increases by $\sim$ 0.1 to 1% at 97.5th-percentile by the end of their evolution. The reason for this small increase comes from the fact that these planets have not yet lost enough atmospheric mass at sufficiently low rates to lead to significantly fractionated residual envelopes. These results thus suggest that for the planets in question, mass-fractionation has likely not played a crucial role in their evolution to date. Furthermore, while we do find that these planets should be experiencing considerable mass-fractionation today - leading to an escape flux of heavier species that is lower by $\sim$ 10% in comparison to the case with no mass-fractionation - it is reasonable to neglect

this because a 10% decrease in escape flux, even with a bulk mass-loss rate of 10^9 g/s, is well within measurement uncertainties.

Furthermore, in our simulations, we did not account for any opacity changes with composition. As a planet gets more enriched in metals due to mass fractionation, its atmospheric opacity should increase. This will make it harder for the planet to cool and it will thus stay inflated for a longer time. As apparent from Equation (4.6), a larger radiative-convective boundary will result in a higher mass-loss rate which, in turn, will lead to lower mass-fractionation (e.g. Zahnle et al., 1990). This suggests that any increase in atmospheric opacity due to mass-fractionation should simply slow down the rate of fractionation itself. Therefore, our estimate of a $\sim$ 0.1 to 1% (97.5^{th}-percentile) increase in the mean molecular weight of the atmosphere could in reality be even lower and accounting for mass-fractionation in the atmosphere could, in fact, lead to even higher mass-loss rates at later times. We thus conclude that it is reasonable to neglect mass-fractionation for the purpose of this work.

4.3.2 Planet candidates that are best modeled with secondary atmospheres, low density interiors, or both

Among the 78 planets we analyze, we find that several could not have retained their primordial hydrogen atmospheres to this day. Among these super-Earths, we find that a few of them have observed bulk densities that are much lower than that of the Earth. These relatively low-density super-Earths include 55 Cnc e, WASP-47 e, Kepler-78 b, Kepler-10 b, CoRoT-7 b, HD 80653 b, and Kepler-36 b (see Table **??**). There is, however, a very low but non-zero likelihood that two of these planets, 55 Cnc e and Kepler-36 b, have indeed hydrogen atmospheres and are losing it rapidly today. All of them, except Kepler-36 b,

have ultra-short orbital periods and experience high insolation flux (see Figure 4.1).

Figure 4.7 shows the posterior distributions for ρ_{c*} for the planets in Table **??**. Since our analysis shows that there is a very low likelihood that any of these planets are left with their primordial hydrogen atmospheres today, these plots simply tell us what the bulk compositions of the respective planets could be. It is then surprising that a subset of super-Earths, which are the focus of this sub-section, have low bulk densities of ρ_{c*} $\lesssim$ 5 g/cm^3. A possible explanation for this is that the planets listed in Table **??** harbor a secondary atmosphere dominated by high molecular weight species, an interior with significant ice-fraction by mass ($\gtrsim$ 10-20%), or both.

A source for a high mean molecular weight atmosphere could be outgassing from a planet's interior/magma oceans (e.g. Elkins-Tanton & Seager, 2008; Bower et al., 2019; Chachan & Stevenson, 2018; Kite & Barnett, 2020) or delivery of volatiles by impactors such as comets (e.g. Raymond et al., 2004; Schlichting et al., 2015; Kral et al., 2020). Once a planet has such a high molecular weight secondary atmosphere, it is typically not possible to lose it through hydrodynamic escape.

On the other hand, a significant amount of ice in a planet's core could also explain a lower ρ_{c*}, even if the planet has lost all its primordial atmosphere (e.g. Rogers & Seager, 2010; Dorn et al., 2017b; Zeng et al., 2019; Mousis et al., 2020). Such planets would likely have formed and migrated from outside the ice-line. As shown in Figure 4.1, most of these planets are on ultra-short orbital periods and experience $\sim$ 1000 times more insolation than Earth. It is thus likely that these planets also have steam atmospheres (e.g. Mousis et al., 2020; Marounina & Rogers, 2020). Furthermore, studies have also hypothesized that low bulk densities could be an artifact of planets having exotic interior compositions, for instance, certain super-Earths might not have a core and could instead be enriched in

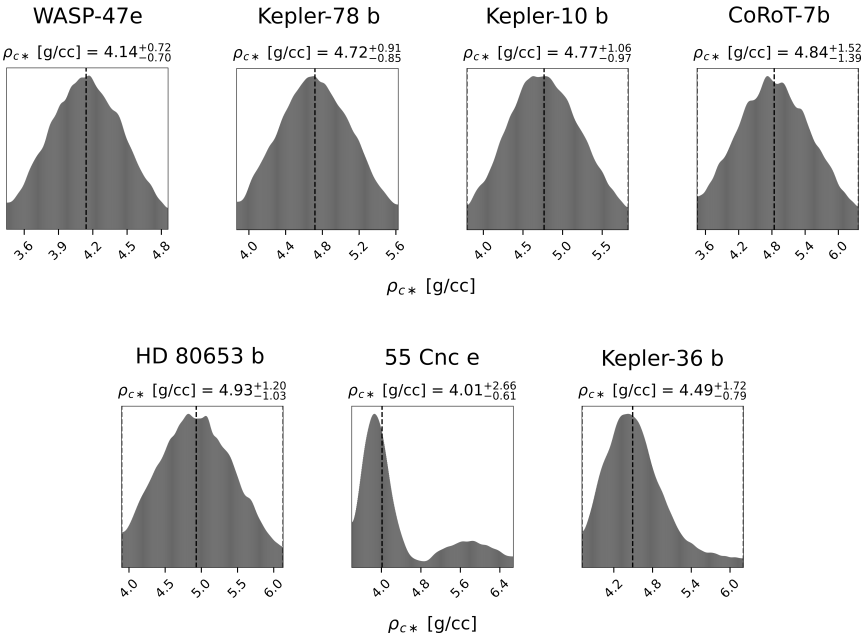

Figure 4.7: Posterior distributions of ρ_{c*} for planets that are likely to have lost their primordial hydrogen atmospheres by today and have bulk densities $\rho_{c*} \lesssim 5$ g/cm^3. Values are reported with 2 σ errors and vertical dashed lines denote the median values. Since these planets have bulk densities much lower than that for Earth, it is likely that they either have secondary atmospheres abundant with heavy molecular weight volatiles, interiors with significant ice-fractions by mass, or both. In addition, we find that 55 Cnc e and Kepler-36 b could also be consistent with having a hydrogen-dominated atmosphere today with a probability of 26% and 10%, respectively.

Ca and Al minerals (Dorn et al., 2017a). Specifically targeting these planets in future surveys could help us to better understand the wide-variety of possible super-Earths and to constrain the role of migration in sculpting the planetary architectures we observe today.

Among the listed planets, 55 Cnc e, WASP-47 e, Kepler-78 b, Kepler-10 b, CoRot-7 b and Kepler 36-b have been a focus of several theoretical studies. However, to the best of our knowledge, attempts have only been published to detect and characterize an envelope around 55 Cnc e. Below, we discuss these past studies in the context of this work.

55 Cnc e: Among the planets that likely lost their primordial atmospheres, and even otherwise, 55 Cnc e is perhaps the most studied small exoplanet to date. It was first detected almost two decades ago by McArthur et al. (2004) and because it orbits a bright Sun-like star with V = 5.95 mag, it has not just been subject of theoretical work but also of numerous observations.

While multiple studies have reported a detection of an atmosphere of 55 Cnc e (e.g. Ridden-Harper et al., 2016; Tsiaras et al., 2016; Demory et al., 2016b), their interpretation of the atmosphere's composition differ significantly (e.g. Ehrenreich et al., 2012; Tsiaras et al., 2016; Esteves et al., 2017; Zhang et al., 2020; Tabernero et al., 2020). For instance, Ehrenreich et al. (2012) and Zhang et al. (2020) have reported non-detections of hydrogen Lyα and helium 1083 nm triplet absorptions, respectively. These studies thus conclude that it is likely that the planet's atmosphere is not hydrogen-dominated today. This however doesn't preclude that the atmosphere might have a mass-loss rate lower than what can be detected, which is estimated by the authors to be $\sim 3 \times 10^8 - 10^9$ g/s. Alternatively, the atmosphere might have high latitude clouds. Using infrared phase curves collected by Spitzer, Demory et al. (2016b) found a large day-night temperature contrast and an off-set of the hottest spot towards east of the sub-stellar point. Based on analysis of such

observations, Demory et al. (2016b) and Angelo & Hu (2017) have argued that 55 Cnc e should have a substantial atmosphere of heavy molecular weight species. Angelo & Hu (2017) further argued that these Spitzer phase curve observations can't be explained if the planet had a magma ocean or a tenuous mineral atmosphere because heat cannot be transferred fast enough (e.g. Kite et al., 2016). In addition, Tsiaras et al. (2016), Esteves et al. (2017) and Jindal et al. (2020) have ruled out the presence of a water dominated atmosphere - based on their analysis of high resolution spectral data collected for the planet. There is also the inexplicable variability in thermal emission from 55 Cnc e which is hard to explain with a simple secondary atmosphere model (Demory et al., 2016a). On the other hand, Tsiaras et al. (2016) reported strong absorption features at 1.42 and 1.54 μm. HCN is identified as the cause of these absorption features and their study finds that these features are strongly suggestive of a hydrogen rich atmosphere.

Our results, unfortunately, do not help in resolving the debate over a hydrogen dominated v.s. secondary atmosphere of 55 Cnc e. Specifically, we find a 74% probability that $\rho_{c*} < 4.8$ g/cc (i.e., solutions that require a low-density interior and/or secondary atmosphere) and a 26% probability that 55 Cnc e still has a hydrogen atmosphere (see bimodality in the ρ_{c*} posterior distribution in Figure 4.7). If the latter is true, 55 Cnc e should be losing its atmosphere at a considerable rate. While the 50^{th}-percentile or median mass-loss rate for 55 Cnc e is ~ 0 g/s, the 84^{th}-percentile and 97.5^{th}-percentile mass-loss rates are 5×10^8 g/s and 1×10^9 g/s, respectively. Interestingly, these estimates are comparable to the threshold mass-loss rates for detection of an escaping atmosphere from 55 Cnc e (Ehrenreich et al., 2012; Zhang et al., 2020).

WASP-47 e, Kepler-78 b, Kepler-10 b, CoRot-7 b, and Kepler-36 b: These planets have been the focus of several theoretical studies that conjecture - in agreement with our

analysis - that they should either have secondary atmospheres (and magma oceans) or/and low density interiors (e.g. Schaefer & Fegley, 2009; Ito et al., 2015; Dorn et al., 2017a; Dai et al., 2019; Chao et al., 2020). Unfortunately, their host stars are much dimmer than 55 Cnc with V $\sim$ 11 to 12 mag (Léger et al., 2009; Queloz et al., 2009; Howard et al., 2013; Becker et al., 2015; Batalha et al., 2011).

There is more to Kepler-36 b, however, as it is also compatible with having a hydrogen atmosphere today. Although this is very unlikely according to our analysis, Kepler-36 b could have a mass-loss rate of 3.5×10^8 g/s at 97.5^{th} percentile. Kepler-36 b is also peculiar in receiving an order-of magnitude lower insolation flux than all the other planets that likely do not have a primordial hydrogen atmosphere today.

HD 80653 b: Recently discovered by Frustagli et al. (2020), HD 80653 b is a small planet around a relatively bright G2 star with V = 9.5 mag. Frustagli et al. speculate that the planet is likely to have lost its hydrogen atmosphere because it is highly irradiated - more than 6000 times than Earth. Our results show that this is indeed the case if the planet's evolution was dominated by core-powered mass-loss. In addition, it has a low bulk density for its size and mass. These factors make it yet another interesting target for further investigations.

4.4 Conclusion

In this paper, we investigate which planets could be undergoing considerable atmospheric mass-loss today if their evolution was dominated by core-powered mass-loss. Of the 78 planets in our sample, we find ten planets with median mass-loss rates of $\gtrsim 10^7$ g/s: pi Men c, Kepler-60 d, Kepler-60 b, HD 86226 c, EPIC 249893012 b, Kepler-107 c, HD

219134 b, Kepler-80 e, Kepler-138 d and GJ 9827 d.

The covariance plots for these targets, unsurprisingly, show correlations between different planetary parameters. Notably, we find that the estimated mass-loss rates are especially sensitive to the uncertainties in a planet's mass measurements. This is especially apparent for planets such as HD 86226c and GJ 9827 d for which our mass-loss estimates vary over $\sim$ 5-10 orders of magnitude for planet masses within 2σ of the median. Furthermore, our results show a two-peaked posterior mass-loss distribution for several planets - peaking at $\sim$ 0 g/s and at $\gtrsim 10^7$ g/s. This indicates that a number of planets from this category, such as HD 219134 b and EPIC 249893012 b, have a low - but non-zero - probability of not losing any atmosphere at all and could rather have a secondary atmosphere and/or low density interiors. While the likelihood of this is typically lower than 10%, Kepler-60 d and Kepler-60 b are only 2 and 1.5 times more likely to have hydrogen-dominated atmospheres, respectively.

Among these planets, HD 219134 b is a especially interesting target because while our analysis suggests that it is likely to have a hydrogen dominated atmosphere, photo-evaporation studies predict the opposite (Dorn & Heng, 2018; Kubyshkina et al., 2018). Detecting atmospheric mass-loss from HD 219134 b could therefore directly confirm that core-powered mass-loss is driving its evolution.

Finally, even though all the planets in this category are likely undergoing fairly rapid atmospheric escape, their 95^{th}-percentile mass-loss rates are still lower than $\sim 9 \times 10^9$ g/s. These lower mass-loss rates might therefore explain the non-detection of Lyα absorption or the He 1083 nm triplet feature for planets such as pi Men c (García Muñoz et al., 2020) and GJ 9827 b (Kasper et al., 2020; Carleo et al., 2021).

In addition, we also identify seven planets for which our core-powered mass-loss model

predicts no residual hydrogen envelopes today, and whose mass and radius measurements thus suggest that they likely have have secondary atmospheres and/or low density interiors. The planets in this list are 55 Cnc e, WASP-47 e, Kepler-78 b, Kepler-10 b, CoRoT-7 b, HD 80653 b, and Kepler-36 b. Among these, our results are somewhat ambiguous for 55 Cnc e and Kepler-36 b because they are also compatible, at a lower probability, with having hydrogen-dominated atmospheres. For instance, 55 Cnc e is only about three times more likely to have a secondary atmosphere and/or low density interior than having a hydrogen dominated envelope according to our analysis.

4.4.1 Future Work

Studies on core-powered mass-loss and photoevaporation have shown that both mechanisms can, independently, explain a multitude of observations associated with the observed radius valley (e.g. Owen & Wu, 2017; Ginzburg et al., 2018; Wu, 2019; Gupta & Schlichting, 2019, 2020; Rogers & Owen, 2020). We assume in this paper that core-powered mass-loss dominates planet evolution. It is however likely that both mechanisms take place simultaneously to a certain degree. Moreover, it is possible that the two processes dictate the atmospheric mass-loss to varying degrees in different parts of the parameter space of the relevant planet and stellar properties. In future studies, we therefore plan to tackle this by combining the two mechanisms to develop a more comprehensive understanding of how planet atmospheres evolve.

4.4.2 Outlook

In this work, we have identified ten planets that could be undergoing atmospheric mass-loss today, as well as, a list of seven planets that likely have secondary atmospheres, ice

rich/iron poor interiors, or both. We hope that the results from this work will aid in the target selection process for future observations. As alluded to earlier, remarkable efforts are continually being made in this direction (e.g. Ehrenreich et al., 2012; Demory et al., 2016b; Ridden-Harper et al., 2016; Benneke et al., 2019; Vissapragada et al., 2020; Kasper et al., 2020; Zhang et al., 2020). The larger sensitivity and spectral range offered by the *James Webb Space Telescope* (e.g. Greene et al., 2016; Allart et al., 2018), scheduled for a launch later this year, and the next-generation ground-based telescopes (e.g. Hood et al., 2020; Vissapragada et al., 2020) should provide us with new data and new insights in the near future.

CHAPTER 5

Properties of the radius valley around low mass stars: Predictions from the core-powered mass-loss mechanism

[1]In recent years, analyzing the bimodality in the size distribution of small planets, i.e., the 'radius valley', has given us unprecedented insight into the planet formation process. Here we explore the properties of the radius valley for low mass stars, assuming that the core-powered mass-loss is the dominant process shaping the small exoplanet population. We show that the slope of radius valley in the planet size-orbital period space, to first-order, does not vary with stellar mass and has a negative slope of $\mathrm{d}\log R_p/\mathrm{d}\log P \simeq -0.11$ even for stars as small as 0.1 $M_\odot$, as observed in latest studies. Furthermore, we find that the slope of the radius valley in the planet size-stellar mass space is $\mathrm{d}\log R_p/\mathrm{d}\log M_* \simeq (3\zeta - 2)/36$ where ζ is given by the stellar mass-luminosity relation $L_* \propto M_*^{\zeta}$. Because ζ is $\gtrsim 2$ and increases with stellar mass, we predict that the radius valley has a positive slope in the planet size-stellar mass space across FGKM dwarfs. This slope, however, decreases (increases) in magnitude towards lower (higher) mass stars, due to the variation of ζ with stellar mass. While around 1.0 $M_\odot$ stars the slope is $\mathrm{d}\log R_p/\mathrm{d}\log M_* \sim 0.37$, it is as low as ~ 0.13 around 0.1 $M_\odot$ stars. In addition, we find that the radius valley is narrower and less empty around lower mass stars. Finally, we show that predictions for the radius valley

[1]This chapter was previously published in similar form as Gupta, A., Nicholson, L. and Schlichting, H. E. 2022, MNRAS, 516, 4585-4593.

for core-powered mass-loss and photoevaporation become increasingly distinct for lower mass stars.

5.1 Introduction

The field of planetary sciences has witnessed a revolution over the last two decades during which over 5000 planets have been discovered. These discoveries have given us unprecedented insight into the formation and evolution of planets. Today we know that planets are quite common in our galactic neighborhood, especially small planets such as those smaller than the size of Neptune ($\sim 4R_\oplus$). Roughly every other star hosts one such planet inside an orbital period of a 100 days (e.g., Borucki et al., 2010; Batalha et al., 2011). Furthermore, among the population of small planets, it has been noted that, surprisingly, there are very few planets of intermediate sizes $\sim$ 1.5 to 2.0 Earth radii (e.g., Owen & Wu, 2013; Fulton et al., 2017; Fulton & Petigura, 2018; Van Eylen et al., 2018). In addition, planets smaller than 1.5 Earth radii ('super-Earths') have been observed to have high densities based on which, models of planetary structure infer that they should have Earth-like composition (e.g., Marcy et al., 2014b; Rogers, 2015; Dressing et al., 2015). Whereas, planets larger than $\sim$ 1.6 Earth radii ('sub-Neptunes') have been observed to have much lower bulk densities which are consistent with large (few % by mass) H/He atmospheres or significant fractions of ices (e.g. Lopez & Fortney, 2014; Jontof-Hutter et al., 2016). This bimodality in the size and composition distribution of small exoplanets has come to be known as the radius valley.

There are two schools of thought on the origin of the radius valley (e.g. Bean et al., 2021). According to one set of theories, namely, photoevaporation and core-powered mass-loss, most of the planets we observe today formed in the presence of a protoplanetary

disk and thus accreted primordial H/He envelopes (Owen & Wu, 2013; Lopez & Fortney, 2013; Jin et al., 2014; Owen & Wu, 2017; Ginzburg et al., 2018; Gupta & Schlichting, 2019, 2020, 2021). Some of these planets however lost their atmospheres entirely over time and became super-Earths. In contrast, planets that were able to retain their atmospheres are today's sub-Neptunes. In the case of photoevaporation, atmospheric mass-loss is driven by the high-energy radiation (e.g., XUV) from the host stars, whereas in core-powered mass-loss model, energy from the planet's formation process together with the host star's bolometric luminosity drives the atmospheric escape.

Alternatively, studies have also suggested that the radius valley could be primordial (e.g., Zeng et al., 2019; Mousis et al., 2020; Lee & Connors, 2020). For instance, Lee & Connors (2020) suggest that super-Earths are planets that never accreted any significant atmosphere, whereas Zeng et al. (2019) suggest that sub-Neptunes are predominantly icy planets with $\sim$ 50% ice-fraction by mass thereby explaining their larger radii. The latter theory, however, cannot yet explain radius valley features such as trends with orbital period and/or stellar mass.

In this work, we solely focus on the implications of the core-powered mass-loss theory which can explain a multitude of observations pertinent to the radius valley such as the location of the radius valley in planet size, the relative occurrences of super-Earths and sub-Neptunes, the timescales on which super-Earths form, and the slopes in the planet size-orbital period space and planet size-stellar mass space (e.g. Fulton & Petigura, 2018; Van Eylen et al., 2018; Martinez et al., 2019; Berger et al., 2020a). In addition, the pertinent studies also inferred that the primordial core-mass distribution likely peaks around 4 $M_{\oplus}$ and that the majority of planets have cores with rocky, Earth-like composition Ginzburg et al. (2018); Gupta & Schlichting (2019).

Previously, core-powered mass-loss studies explored the role of this mechanism in the evolution of planets around FGK dwarfs only. The motivation for these studies were the unprecedented observations from the *Kepler* space observatory. A lot of the recent work in the exoplanet community has however been put into observing planets around M-dwarfs and thus also on studying the planet demographics around such stars (e.g., Wu, 2019; Cloutier & Menou, 2020; Van Eylen et al., 2021; Petigura et al., 2022). There are a multitude of reasons for this. To list a few, not only are M-dwarfs the most abundant stars in the Universe, accounting for an estimated three-quarters of the stars in our Milky Way galaxy, but they are estimated to have the highest small-planet occurrence rate among FGKM dwarfs for a given range of orbital periods (e.g. Hsu et al., 2020). Furthermore, it is easier to observe small planets around these smaller stars, and many of them could in fact be in the habitable zones as these stars are much cooler (e.g. Scalo et al., 2007). The TRAPPIST-1 system is an ideal example of a planetary system around an ultra-low mass star (0.089 $M_{\odot}$) that hosts several planets in the habitable zone (Gillon et al., 2016, 2017). Furthermore, as alluded to in Rogers et al. (2021), looking at a wider range of stellar masses will facilitate our efforts towards distinguishing between the expected signatures of photoevaporation and core-powered mass-loss imprinted on the exoplanet population. Given these reasons, in this paper, we investigate the evolution of sub-Neptunes and super-Earths around low-mass stars with masses as low as 0.08 $M_{\odot}$.

Recent observational studies on planet demographics around such low mass stars show that the radius valley extends at least to early-M dwarfs (e.g., Cloutier & Menou, 2020; Van Eylen et al., 2021; Petigura et al., 2022). To characterize the radius valley, studies have tried to estimate its location in planet size and slope in different parameter spaces such as planet size-orbital period and planet size-stellar mass. Van Eylen et al. (2021) and Petigura et al. (2022) recently analyzed the distribution of planets around M and K dwarfs

with masses $\sim$ 0.15-0.6 $M_{\odot}$ and 0.5-0.7 $M_{\odot}$, respectively. They found that the radius valley in the planet size-orbital period space has a negative slope of -0.11$^{+0.05}_{-0.04}$ and -0.12$^{+0.02}_{-0.04}$, respectively. These values are consistent with those reported previously for FGK dwarfs $\sim$ 0.8-1.2 $M_{\odot}$ (e.g. Fulton & Petigura, 2018; Van Eylen et al., 2018; Martinez et al., 2019). Theories based on atmospheric escape show that they can explain this slope. For instance, using simple analytical arguments and numerical simulations, Gupta & Schlichting (2019) showed that if atmospheric loss is dominated by core-powered mass-loss, the radius valley slope for planets around FGK stars in the planet size-orbital period space should be -0.11. Contrary to the observational studies mentioned above, Cloutier & Menou (2020) measured a positive slope of 0.058$\pm$0.022 for the radius valley in the same parameter space for M dwarfs ranging 0.08-0.6 $M_{\odot}$. The authors attributed this to an increasing role of gas-poor accretion around lower mass stars (Lee & Chiang, 2016; Lopez & Rice, 2018).

In this study, we simulate planets around these lower stellar masses and show that if planet evolution is indeed dictated by core-powered mass-loss, the slope of the radius valley in the planet size-orbital period space should remain negative and close to -0.11 as predicted previously for Sun-like stars in Gupta & Schlichting (2019).

Furthermore, while it has been already known that the radius valley around dwarfs has a positive slope in the planet size-stellar mass space (Fulton & Petigura, 2018), recent observational studies on planets around early M to FGK dwarfs have tried to quantify this slope. Petigura et al. (2022) looked at 0.5-1.4 $M_{\odot}$ stars and estimated a slope of 0.18$^{+0.08}_{-0.07}$ whereas Berger et al. (2020a) found a slope of 0.26$^{+0.21}_{-0.16}$ for a similar stellar mass range but a distinct dataset. These studies have then compared these measurements with theoretical predictions from photoevaporation and core-powered mass-loss models and have noted how with the current precision, both theories are consistent within 1-2 σ. There are however caveats with making such comparisons. For instance, the predicted radius valley slope in

the planet size-stellar mass space of 0.33 reported in Gupta & Schlichting (2020) was for a specific subset of the *California-Kepler Survey* (CKS) dataset then available that consisted of FGK dwarfs only. This is important because this slope depends on how strongly or weakly the stellar mass and luminosity are correlated due to the dependence of mass-loss rate on planetary equilibrium temperature and thus stellar luminosity, and this correlation itself depends on stellar mass (e.g., Salaris & Cassisi, 2005; Eker et al., 2018; Berger et al., 2020a). For a unique dataset of stars, the estimated slope will thus be unique. In this work, we show how this correlation between the stellar mass and luminosity changes with stellar mass, and ultimately, present predictions for how the radius valley changes towards lower stellar masses.

This paper is structured as follows: In Section 5.2, we review how we model the structure of a planet and its evolution over time under the core-powered mass-loss mechanism. Following this, we describe the changes in our planet evolution model in comparison to previous studies and how we model the exoplanet population. We then discuss our results in Section 5.3 and show how the radius valley around M dwarfs differs from that around FGK dwarfs. Finally, we present our conclusions in Section 5.4.

5.2 Methods

In this section, we provide a brief overview of how a planet evolves after the dispersal of the protoplanetary gas disk, and the accompanying atmospheric mass-loss via the 'boil-off' or 'spontaneous mass-loss' process (e.g. Owen & Wu, 2016; Ginzburg et al., 2016). While multiple theories have been put forth in this regard, we assume that any subsequent evolution is solely driven by the thermal evolution and atmospheric escape driven by the core-powered mass-loss mechanism as previously explored in Ginzburg et al. (2018); Gupta

& Schlichting (2019, 2020).

During the formation of a planet, as solids accrete to form a planetary core, the gravitational energy resulting from this process gets converted into thermal energy. If this happens after the protoplanetary gas disk has dispersed, this energy can get radiated away on extremely short timescales. However, if this occurs during the presence of a gas disk, the planet will, once it has cooled to temperatures sufficiently low such that gas can become gravitationally bound, also accrete an H/He envelope. Once this planetary envelope becomes optically thick, any energy exchange between the surroundings and the planet will be regulated by the radiative diffusion across the radiative-convective boundary leading to much longer cooling timescales than if the planet had an optically thin or no atmosphere (e.g. Rafikov, 2006; Lee & Chiang, 2015; Ginzburg et al., 2016). Effectively, such an atmosphere will act as a thermal blanket for the planet allowing a significant fraction of the formation energy to be trapped within. As the protoplanetary gas disk then disperses, the decrease in the pressure support outside a planet's atmosphere will lead to atmospheric escape. This mass-loss phase is known as the boil-off or the spontaneous mass-loss process and sets the initial conditions for both core-powered mass-loss and photoevaporation. The idea behind core-powered mass-loss is that the remnant primordial formation energy can eventually unbind the planet's atmosphere via a Parker-type hydrodynamic wind in the outer regions of the atmosphere where the temperature is set by the host star's bolometric luminosity (e.g. Parker, 1958). Planets that eventually lose their entire atmospheres are today's super-Earths whereas those that are able to retain some of their primordial H/He atmospheres are the sub-Neptunes we see today. This results in a bimodal planet size distribution and thus, a radius valley.

5.2.1 Planet Structure and Evolution

For our planet evolution model, we use the same framework as described in Ginzburg et al. (2018) and Gupta & Schlichting (2019) unless specified otherwise. We assume that post-disk dispersal and boil-off/spontaneous mass-loss, a typical planet with mass M_p and radius R_p, has a core with an Earth-like composition that is surrounded by an H_2 atmosphere of mass M_{atm}. The core here refers to the non-gaseous part of the planet that has a mass M_c and radius R_c and the core is assumed to account for most of the mass of the planet such that $M_c \sim M_p$. For the atmosphere, we model it to have an inner convective and an outer radiative region (e.g. Piso & Youdin, 2014; Lee & Chiang, 2015). It is thus assumed that the inner region has an adiabatic profile whereas the radiative region is nearly isothermal with a temperature equal to the planetary equilibrium temperature T_{eq}. The radius at which such an atmosphere transitions from the convective to the radiative region is the radiative-convective boundary R_{rcb}. The atmosphere's density decreases exponentially with radius in the radiative region, and thus most of the mass of the atmosphere, M_{atm}, resides within the convective region. Consequently, the photospheric radius of the planet R_p is approximately equal to R_{rcb} which, in turn, is assumed to be roughly twice the core radius after the disk dispersal, based on previous work (Ginzburg et al., 2016).

Given this structural model for a planet, we can now discuss how its atmospheric mass fraction $f = M_{atm}/M_c$ and cooling energy E_{cool}, i.e. the energy that a planet can lose, evolve over time. We assume that given some initial f, a planet loses this atmosphere in either an energy-limited regime or a Bondi-limited regime. The energy limited regime corresponds to the absolute upper limit on atmospheric escape where all the luminosity from a cooling planet goes into driving mass loss. This mass-loss rate $\dot{M}^E_{atm}$ can be written

as

$$\dot{M}^{E}_{atm} \simeq \frac{L_{rcb}}{gR_c}, \tag{5.1}$$

where L_{rcb} is the luminosity of the planet at the radiative-convective boundary and g is the acceleration due to gravity at R_{rcb}. In reality, the efficiency with which a planet's cooling luminosity can drive mass should be <100%, but note that the contribution from the host star's bolometric luminosity, that we don't model in detail here, also plays a supporting role in driving this mass-loss, as it contributes to maintaining the radiative-convective profile of the planet. Ideally, detailed radiative-hydrodynamic calculations are needed to solve for atmospheric escape with incoming and outgoing radiation due to the host star and planet. This is unfortunately beyond the scope of this work. Nevertheless, as discussed previously in Gupta & Schlichting (2019) and in this manuscript, the shape of the radius valley, i.e., its slope and depth, is primarily dictated by the balance of the planetary cooling and mass-loss timescales. Thus, we do not expect the assumption of a maximum mass-loss efficiency to have a significant implication for the slope of the radius valley and note that there is also likely a significant degeneracy between the mass-loss efficiency and a planet's assumed initial atmosphere mass-fraction, which remains highly uncertain.

Alternatively, the Bondi-limited mass-loss rate $\dot{M}^{B}_{atm}$ is the maximum mass-loss rate physically possible given the finite thermal velocities of the gas molecules at the Bondi radius which, in turn, is dictated by the bolometric luminosity of the host star and the planet's semi-major axis. In this regime, the mass-loss rate $\dot{M}^{B}_{atm}$, can be written as

$$\dot{M}^{B}_{atm} = 4\pi R_s^2 c_s \rho_s = 4\pi R_s^2 c_s \rho_{rcb} \exp\left(-\frac{GM_p}{c_s^2 R_{rcb}}\right), \tag{5.2}$$

where $R_s = GM_c/2c_s^2$ is the sonic radius, i.e., the radius at which the escaping atmosphere reaches sonic velocities, $c_s = (k_B T_{eq}/\mu)^{1/2}$ is the isothermal speed of sound with Boltzmann constant k_B and mean molecular weight μ, and ρ_s and ρ_{rcb} are the atmospheric densities

at R_s and R_{rcb}. The exponential dependence of the mass-loss rate on M_p, R_{rcb} and T_{eq} stems from the isothermal nature of the outer regions of the atmosphere which requires an exponential decline in the atmosphere's density with radius. Ultimately, the mass-loss rate a planet experiences at a particular time in its evolution is the smaller of the Bondi- and energy-limited mass-loss rates, i.e., $\dot{M}_{atm} = min\{\dot{M}^E_{atm}, \dot{M}^B_{atm}\}$. We can thus express the mass-loss timescale, t_{loss}, of a planet as

$$t_{loss} = \frac{M_{atm}}{|\mathrm{d}M_{atm}/\mathrm{d}t|} = \frac{1}{\min\left\{\dot{M}^E_{atm}/M_{atm},\ \dot{M}^B_{atm}/M_{atm}\right\}}. \tag{5.3}$$

On the other hand, the cooling timescale for a planet can be written as

$$t_{cool} = \frac{E_{cool}}{|\mathrm{d}E_{cool}/\mathrm{d}t|} = \frac{E_{cool}}{L_{rcb}}. \tag{5.4}$$

Together, Equations 5.3 and 5.4 determine how a planet evolves in our model. We thus numerically solve these equations over time to ultimately track how a planet's size and atmosphere mass-fraction evolve.

5.2.2 Accounting for evolution of a host star's luminosity

Previously in Ginzburg et al. (2018) and Gupta & Schlichting (2019, 2020), we did not account for the evolution in the luminosity of the host stars, but this change can be significant for low mass stars. This is apparent in Figure 5.1 where we show the luminosity evolution tracks for a range of stellar masses. This figure begins at 3 Myr of age, assuming that to be the approximate time of disk dispersal (e.g. Mamajek, 2009). We see that for a Sun-like 1 $M_\odot$ star, the luminosity undergoes a negligible change after the dispersal of its protoplanetary disk. We do note that the luminosity of such a star increases continually over the time period shown in Figure 5.1, but as we will see later in Section 5.3, this has no significant impact on the core-powered atmospheric mass-loss results. On the other end of

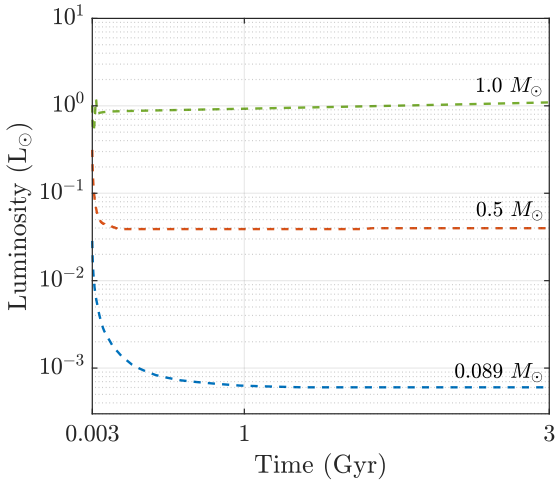

Figure 5.1: Evolution in the luminosities of stars of different masses from an age of 3 Myr to 3 Gyr. The plot shows that while there is an no significant change in the luminosity of a Sun-like 1.0 $M_\odot$ star, the luminosity of a star such as TRAPPIST-1 with a mass of 0.089 $M_\odot$ undergoes a change in luminosity of one-to-two orders in magnitude during the first Gyr of its lifetime.

the spectrum, for a TRAPPIST-1 like ultra-low mass star, the luminosity changes by one to two orders-of-magnitude during the first Gyr of evolution. The stellar luminosity L_* plays a key role in a planet's evolution as it sets its equilibrium temperature

$$T_{eq} = \left(\frac{1}{16\pi\sigma} \frac{L_*}{a^2} \right)^{\frac{1}{4}}, \tag{5.5}$$

where σ is the Stefan-Boltzmann constant and a is the planet's semi-major axis. As mentioned in the preceding paragraph, the mass-loss rate of a planet has an exponential dependence on T_{eq}. As a consequence, the mass-loss rate or mass-loss timescale, t_{loss}, is sensitive to changes in T_{eq}.

Therefore, to track planet evolution around low-mass stars, we explicitly include the evolution of the stellar luminosity with time in our core-powered mass-loss model as follows: For stars more massive than 0.1 $M_\odot$, we use the MIST stellar evolutionary tracks (version 1.2; Dotter, 2016; Choi et al., 2016) that are computed with the Modules for Experiments in Stellar Astrophysics (MESA) code (Paxton et al., 2011, 2013, 2015, 2018, 2019). For stars less massive than 0.1 $M_\odot$, we directly use the MESA code (version: mesa-r21.12.1) to compute stellar evolution tracks as data for such ultra-low mass stars are not available as part of the MIST database. In addition, we assume all the stars have a metallicity of $Z = 0.014$.

5.2.3 Modeling planet population

In this subsection, we describe how we model the distribution of atmosphere mass fractions f, core masses M_c and orbital periods P.

Following previous studies (e.g., Ginzburg et al., 2018; Gupta & Schlichting, 2019),

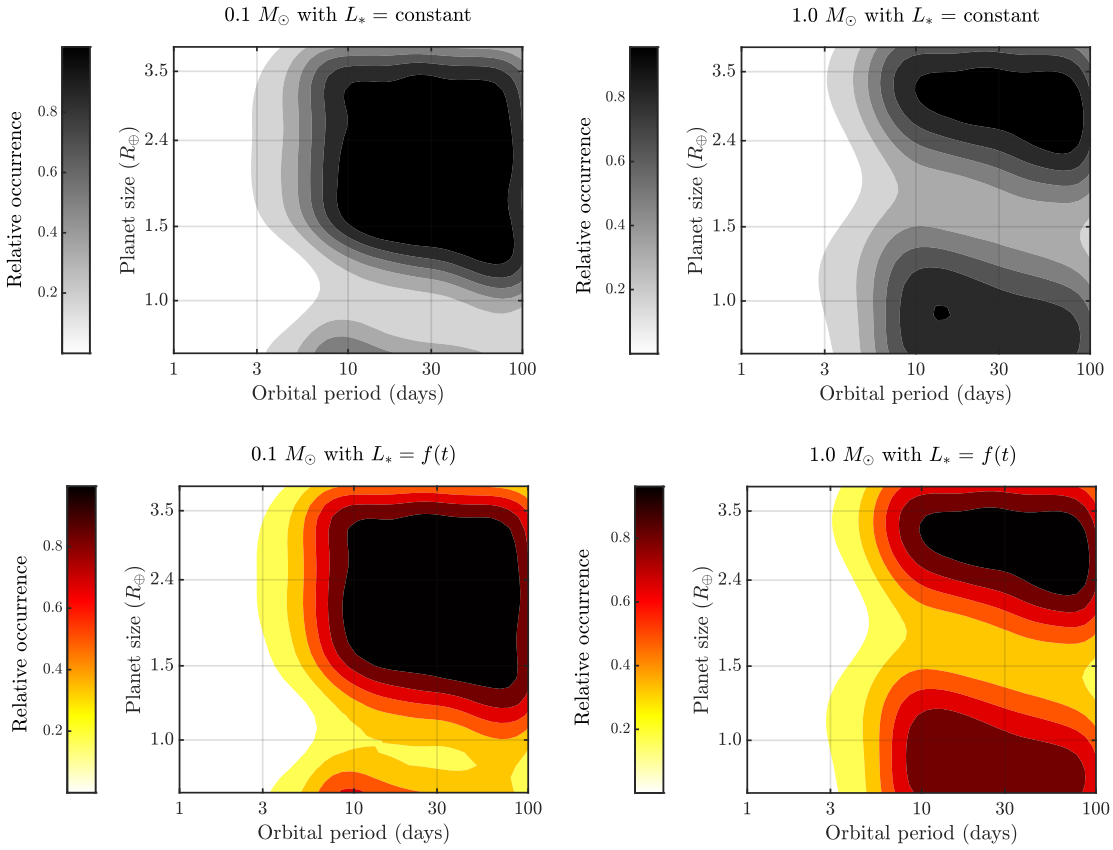

Figure 5.2: Distribution of planets in the planet size-orbital period space. The left and right panels show planet populations around a 0.1 and 1.0 $M_\odot$ star, respectively (*continued next page*).

Figure 5.2: Distribution of planets in the planet size-orbital period space. The left and right panels show planet populations around a 0.1 and 1.0 $M_\odot$ star, respectively. While the gray plots in the top row represent the case where planets were evolved around stars of constant luminosity (taken to be the luminosity at 3 Gyr), the bottom row shows the final planet size distributions when the luminosity evolution of the host stars is accounted for. Comparing the top and bottom rows shows that, unsurprisingly, the impact of the host star's luminosity evolution is negligible for 1.0 $M_\odot$ stars. On the other hand, for 0.1 $M_\odot$ stars the host star's luminosity evolution results in a narrower and less empty radius valley but, at the same time, does not lead to a change in its location or slope. These plots also show that the radius valley slope is the same around both 0.1 and 1.0 $M_\odot$ stars: $\mathrm{d}\log R_p / \mathrm{d}\log P$ = -0.11, which is consistent with observational results reported by Van Eylen et al. (2021) and Petigura et al. (2022).

we assume that planets have an initial atmospheric mass-fraction of

$$f = \frac{M_{atm}}{M_c} \simeq 0.05(M_c/M_\oplus)^{1/2}. \tag{5.6}$$

This is motivated by past studies of gas accretion and the atmosphere loss that follows the disk dispersal, i.e. the boil-off or spontaneous mass-loss process (e.g. Owen & Wu, 2016; Ginzburg et al., 2016). We do note however that such a one-to-one relation between f and M_c is not expected in nature due to the stochasticity inherent in the process of planet formation even if the correlation is physically motivated. To check if this approximation has an impact on the radius valley, we tested our evolution models with a wider distribution of atmospheric mass-fractions. Specifically, we implemented a log-normal distribution with a mean given by Equation (5.6) and a standard deviation of 0.25, which encompasses about a factor of 2 variations in f. We find that the results with the log-normal distribution are essentially indistinguishable from the ones presented in this paper. Furthermore, in Gupta & Schlichting (2019) we demonstrated that even for a log-uniform distribution of initial-envelope mass-factions, as assumed in Owen & Wu (2017), the radius valley is still a robust outcome although the exact shape, especially of the sub-Neptune population, is slightly different.

The period distribution has been observed to be fairly constant across a significant range of stellar masses, 0.5 $M_\odot$ to 1.4 $M_\odot$ (see Petigura et al., 2022). In this work, we assume that the same observed period distribution

$$\frac{\mathrm{d}N}{\mathrm{d}\log P} \propto \begin{cases} P^2, & P < 8 \text{ days} \\ \text{constant}, & P > 8 \text{ days, and} \end{cases} \tag{5.7}$$

applies to the entire range of stellar masses explored here.

Finally, we assume that the planetary masses are distributed uniformly in log-space. This allows us to share predictions in this paper that are agnostic to the yet unknown 'true'

planet mass distribution and how it depends on stellar properties such as stellar mass; see Teske et al. (2020).

5.3 Results & Discussion

In this section, we explore the changes in the planet demographics around lower mass stars. This includes investigating the location and slope of the radius valley in planet size-orbital period and planet size-stellar mass space. Finally, we discuss how focusing on lower stellar masses can make it easier to distinguish between the signatures of core-powered mass-loss and other mechanisms that have been put forth to explain the radius valley.

5.3.1 Radius valley as a function of orbital period around low mass stars

As discussed in Section 5.2.2, in past core-powered mass-loss studies the evolution of the host star's luminosity was not included, but this change can be significant for low mass stars; see Figure 5.1. In Figure 5.2, we show the impact of this luminosity evolution for a Sun-like 1.0 $M_{\odot}$ star and an ultra-cool M dwarf with a mass of 0.1 $M_{\odot}$. This figure shows the planet size distribution in the planet size-orbital period ($R_p - P$) space after 3 Gyr of evolution given our initial conditions. For plots in the bottom row, we accounted for evolution in the stellar luminosities whereas for the top row we did not and evolved the planets at a fixed luminosity - the star's luminosity at the age of 3 Gyr. Comparing the top and bottom rows for the 1.0 $M_{\odot}$ case shows that the two cases are practically identical - reinforcing that it is reasonable to ignore the luminosity evolution for FGK stars in this context, as assumed in previous core-powered mass-loss studies (e.g. Gupta & Schlichting, 2020). Comparing the top and bottom rows for the 0.1 $M_{\odot}$ case shows however that for

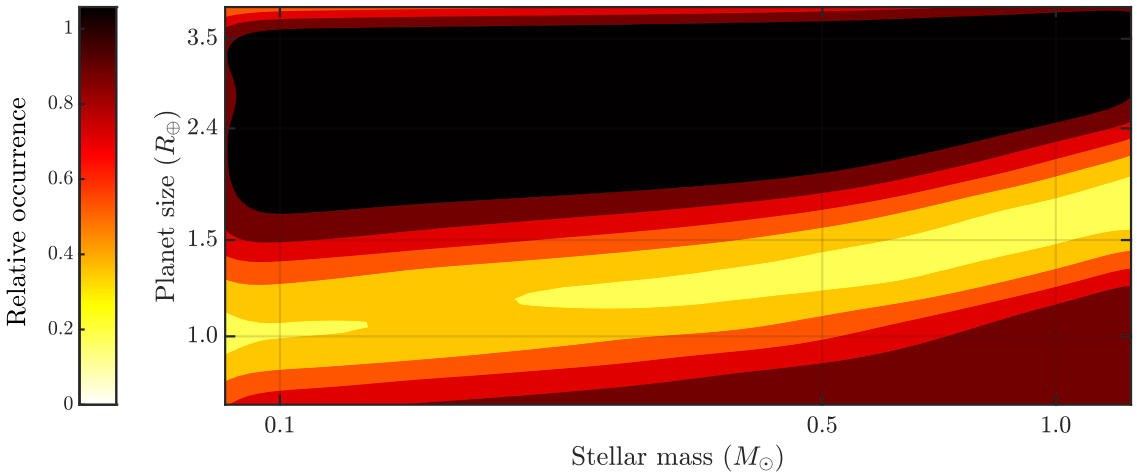

Figure 5.3: Distribution of planets in the planet size-stellar mass space for stellar masses ranging over 0.08 to 1.25 $M_\odot$. Plot shows how the radius valley decreases in planet size with decreasing stellar masses and becomes relatively narrower and less empty. We also find that the slope of the radius valley d logR_p/d logM_* is not constant and becomes shallower towards lower mass stars. As discussed in the main text, the radius valley slope is positive because at a given orbital period, planets around more massive stars have higher equilibrium temperatures as more massive stars are more luminuous. Therefore, a planet around a relatively massive star is more susceptible to complete atmospheric loss and the valley moves up in planet size with increasing stellar mass. This slope however changes with stellar mass because the degree of correlation between stellar mass and stellar luminosity, encapsulated in ζ, itself changes with stellar mass. This change in slope is even more apparent in Figure 5.4.

such low mass stars the radius valley is narrower and less empty when the luminosity evolution is included. Nevertheless, the planet distributions are not drastically different, and we can thus exploit this to make analytical estimates for the slopes of radius valley in different parameter spaces down to very low stellar masses.

It is evident from Figure 5.2 that core-powered mass-loss predicts a negative slope for the radius valley in the $R_p - P$ parameter space even around ultra-low mass stars. As previously derived in Gupta & Schlichting (2019, 2020), the slope of the radius valley can be estimated by realizing that sub-Neptunes are planets that reached a point in their evolution where they cool and shrink faster than they lose mass while they still have substantial envelopes. Whereas super-Earths were able to lose most or all of their envelopes before cooling could catch up with the mass-loss. Therefore, the slope of the radius valley can be estimated by equating the mass loss and cooling timescales, which yields

$$\frac{GM_p}{c_s^2 R_{rcb}} \simeq \text{constant}. \tag{5.8}$$

as shown in Gupta & Schlichting (2019, 2020). Substituting for the speed of sound, the mass-radius relation for the core $M_c \propto R_c^4 \rho_{c*}^{4/3}$ where ρ_{c*} is the density of the core scaled to an Earth mass, and using the fact that $R_{rcb} = R_p \sim 2R_c$, simplifies Equation (5.8) to

$$R_p^3 T_{eq}^{-1} \rho_{c*}^{4/3} \sim \text{constant}. \tag{5.9}$$

By definition, planetary equilibrium temperature depends on stellar luminosity and semi-major axis such that $T_{eq}^4 \propto L_*/a^2$. Using the law of gravitation, we know that a planet's orbital period $P^2 \propto a^3/M_*$. Putting these two relations together gives that $T_{eq} \propto P^{-1/3} L_*^{1/4} M_*^{-1/6}$. In addition, it is also known that the stellar mass and luminosity are positively correlated, i.e. $L_* \propto M_*^{\zeta}$, where ζ (e.g. Salaris & Cassisi, 2005; Eker et al., 2018; Berger et al., 2020a). We thus find that equilibrium temperature, orbital

period and stellar mass are correlated such that $T_{eq}^{-1} \propto P^{1/3} M_*^{-(\zeta/4)+(1/6)}$. Substituting this in Equation (5.9) gives us

$$R_p^3 P^{1/3} M_*^{-(\zeta/4)+(1/6)} \rho_{c*}^{4/3} \sim \text{constant}. \tag{5.10}$$

Assuming that planets across orbital periods of 1-100 days have, on average, similar core composition, the slope in the $R_p - P$ space around a star of a particular mass is simply $\mathrm{d}\log R_p / \mathrm{d}\log P = -1/9 \simeq$ -0.11, i.e. independent of the mass of the host star. In other words, the susceptibility to atmospheric loss strongly depends on the planetary equilibrium temperature T_{eq}. Around any star, T_{eq} decreases with increasing orbital period such that $T_{eq} \propto P^{-1/3}$. A planet at longer orbital periods is thus less susceptible to significant atmospheric loss and the location of the radius valley moves to smaller planet sizes with increasing orbital period, i.e. it has a negative slope in the $R_p - P$ space.

This result is consistent with the observations of slope across FGKM dwarfs. Recently, Van Eylen et al. (2021) and Petigura et al. (2022) reported negative slopes for the radius valley around low-mass stars: $\mathrm{d}\log R_p / \mathrm{d}\log P = -0.11^{+0.05}_{-0.04}$ for stars in the range $\sim$ 0.15-0.6 $M_\odot$ and $-0.12^{+0.02}_{-0.04}$, for stars in the range 0.5-0.8 $M_\odot$, respectively. Previously, studies such as Van Eylen et al. (2018) and Martinez et al. (2019) have reported negative slopes of $\mathrm{d}\log R_p / \mathrm{d}\log P = -0.09^{+0.04}_{-0.02}$ and $-0.11^{+0.03}_{-0.03}$, respectively, for the radius valley around FGK dwarfs.

5.3.2 Radius valley as a function of stellar mass around low mass stars

Figure 5.2 also demonstrates how the location of the radius valley changes with stellar mass. When comparing the bottom panels for the two stellar masses, we can see that the radius valley around the less massive star moves to smaller planet sizes. This shift in the location of the radius valley is even more apparent in Figure 5.3 where we show the planet

size distribution as a function of planet size and stellar mass. This plot shows not just that the radius valley shifts to lower planet sizes with decreasing stellar mass, i.e., the slope of the radius valley is positive in the planet size-stellar mass space, but predicts that towards lower mass stars the slope of the radius valley becomes shallower. In Figure 5.4, we focus on three stellar mass bins that have an equivalent span in logarithmic space: 0.1 - 0.15 $M_{\odot}$, 0.4 - 0.6 $M_{\odot}$, and 0.8 - 1.2 $M_{\odot}$ (from left to right).

The positive slope of the radius valley in the $R_p - M_*$ space can be understood by same physics that we used to explain the radius valley slope in the $R_p - P$ space. As shown earlier, there is a positive correlation between stellar mass and planetary equilibrium temperature/insolation flux for a given orbital period $T_{eq} \propto M_*^{(\zeta/4)-(1/6)}$ (e.g. Salaris & Cassisi, 2005; Eker et al., 2018; Berger et al., 2020a). Therefore, at a particular orbital period, a planet around a low mass star is at a lower T_{eq} as it receives less bolometric insolation flux ($S_p \propto T_{eq}^{1/4}$) in comparison to a planet at the same orbital period around a high mass star. In other words, a planet at a particular orbital period around a more massive star is more susceptible to a complete atmospheric loss. This explains why the radius valley moves to larger planet sizes around more massive stars, resulting in a positive slope in the $R_p - M_*$ space.

We can obtain an analytical estimate for $\mathrm{d}\log R_p/\mathrm{d}\log M_*$ using Equation (5.10) by assuming that the orbital period distribution is independent of stellar mass (e.g. Fulton & Petigura, 2018; Petigura et al., 2022) and that the short-period planets typically have similar core compositions, such that ρ_* is independent of P and M_*, (e.g. Gupta & Schlichting, 2019; Doyle et al., 2019; Bower et al., 2019; Rogers et al., 2021), which yields

$$\frac{\mathrm{d}\log R_p}{\mathrm{d}\log M_*} = \frac{3\zeta - 2}{36}. \tag{5.11}$$

ζ has been observed to be $\gtrsim 2$ for stars more massive than 0.179 $M_{\odot}$ (e.g. Salaris & Cassisi,

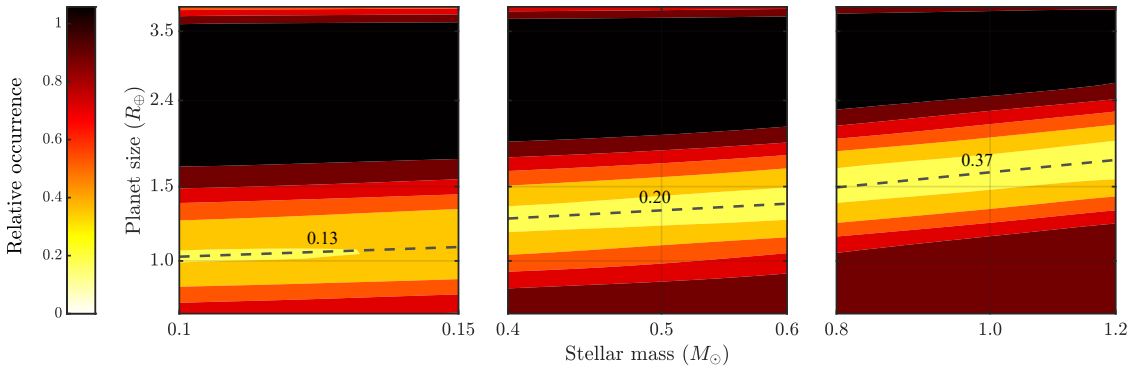

Figure 5.4: Same as Figure 5.3 but presenting an expanded view of the radius valley in three narrower stellar mass bins that span (from left to right) 0.1 to 0.15 $M_\odot$, 0.4 to 0.6 $M_\odot$ and 0.8 to 1.2 $M_\odot$. This plot clearly shows how the radius valley slope decreases with decreasing stellar mass. Dashed lines are based on our analytical estimate for the slope of the radius valley and show an excellent match with the simulation results. These slopes $\mathrm{d}\log R_p/\mathrm{d}\log M_* = 0.13$, 0.20 and 0.37 for the three stellar mass bins as depicted in the figure.

2005; Eker et al., 2018). Equation (5.11) thus shows that for typical values of ζ, the radius value has a positive slope. Furthermore, this equation encapsulates how the slope of the radius valley in the $R_p - M_*$ space depends on the correlation between stellar mass and luminosity ($L_*/L_\odot = (M_*/M_\odot)^\zeta$.). For a larger (smaller) ζ, the slope is larger (smaller).

It is commonly assumed that for zero-age main-sequence stars $\zeta \sim 3.5$, as can be shown using order-of-magnitude arguments. However, this is not accurate for actual stars - especially those in the mass range of 0.1 to 1.5 $M_\odot$. Even though this is a good approximation as it is within a factor of 2-3 of observed values, a change in ζ from 2 to 6 is equivalent to changing the radius valley slope estimate in the $R_p - M_*$ space from $\mathrm{d}\log R_p/\mathrm{d}\log M_* = 0.11$ to 0.44. This is a significant change. In fact, ζ does vary in

Stellar mass bins ($M_\odot$)	ζ ($L_* \propto M_*^\zeta$)	d logR_p/d logM_*
0.1 - 0.15	2.2	0.13
0.4 - 0.6	3.1	0.20
0.8 - 1.2	5.1	0.37

Table 5.1: Summary of how the slope of the radius valley in planet size-stellar mass space, d logR_p/d logM_*, (last column) and the stellar mass-luminosity relation, ζ, (middle column) change with stellar mass, for three stellar mass bins (first column).

the aforementioned range as has been noted in past studies (e.g. Salaris & Cassisi, 2005; Berger et al., 2020a). For instance, in Eker et al. (2018), the authors investigated the stellar mass-luminosity relation for a sample of 509 main-sequence stars within the mass range $0.179 \leq M_*/M_\odot \leq 31$. For stars with masses in the range $0.179 \leq M_*/M_\odot \leq 0.45$, $0.45 < M_*/M_\odot \leq 0.72$, and $0.72 < M_*/M_\odot \leq 1.05$, they found that $\zeta \simeq 2.0$, 4.6 and 5.7, respectively.

To track the luminosity evolution of stars included in Figure 5.4, we used MIST tracks. We find that ζ values for 3 Gyr old stars in the mass ranges shown in Figure 5.4, i.e., 0.1-0.15 $M_\odot$, 0.4-0.6 $M_\odot$ and 0.8-1.2 $M_\odot$ are $\sim$ 2.2, 3.1 and 5.1, respectively. Unsurprisingly, these values encompass the same range as found in Eker et al. (2018). This is expected as the MIST datasets are derived from the stellar evolution code MESA, which is, in turn, tuned to match the properties of the observed stars (e.g. Paxton et al., 2011, 2013). Nevertheless, the fact that ζ increases with stellar mass in the mass range 0.1-1.2 $M_\odot$ implies that the slope of the radius valley in the planet size-stellar mass space increases in magnitude with increasing stellar mass. Consequently, given Equation (5.11), we find that the slope of the radius valley d logR_p/d logM_* = 0.13, 0.20 and 0.37 for 3 Gyr old stars with masses 0.1-

0.15 $M_{\odot}$, 0.4-0.6 $M_{\odot}$ and 0.8-1.2 $M_{\odot}$, respectively. We summarize this result in Table 5.1. These slopes have been plotted in Figure 5.4 using dashed lines and provide an excellent match to the simulations.

5.3.3 Comparing the predictions of core-powered mass-loss with photoevaporation, and observations

The results presented above raise the question if these new predictions for the core-powered mass-loss mechanism are significantly different from those expected from photoevaporation. Figure 5.5 aims to address this question. In this figure, we examine how the radius valley slope in the planet size-stellar mass space, d $\log R_p$/d $\log M_*$, changes with ζ (i.e. stellar mass) for the two mass-loss models. To estimate the slope of d $\log R_p$/d $\log M_*$ for the core-powered mass-loss theory, we used Equation (5.11); for estimating the same slope for photoevaporation, we used derivations from Rogers et al. (2021) where it was shown that d $\log R_p$/d $\log M_* \sim 0.12(\zeta - (2/3)) - 0.17$. For a full derivation of the latter result, the reader is referred to the discussion accompanying Equations 6 and 24 in Rogers et al. (2021). We find that for photoevaporation too the slope of the radius valley is likely to decrease in magnitude towards lower stellar masses because of the dependence of ζ on stellar mass. However, this figure also shows that while the difference in the slopes is quite small for solar-mass stars, it increases substantially towards lower stellar masses. This result further motivates efforts toward characterizing the radius valley around M dwarfs.

Two observational studies, Berger et al. (2020a) and Petigura et al. (2022), have provided constraints on the radius valley slope in the planet size-stellar mass space: $0.26^{+0.21}_{-0.16}$ and $0.18^{+0.08}_{-0.07}$, respectively. In theory, one could compare the predictions presented in Figure 5.5 with these values. However, ζ for these studies were not estimated and it is not known how

these slopes change with stellar mass. Although this implies that a direct comparison of the slopes estimated by Berger et al. (2020a) and Petigura et al. (2022) and our predictions is not very informative, the magnitude of the observed slopes are in the range expected for planets evolving under core-powered mass-loss $\sim 0.20 - 0.35$. It should be noted that for correctly comparing a slope obtained from observational studies to the predictions of core-powered mass-loss or photoevaporation, one cannot simply choose a value for ζ using the MIST tracks. The purpose of using MIST tracks in this study is to simply demonstrate how the radius valley slope changes with stellar mass by using an open-source tool widely used in the community. The MIST tracks, on their part, are informed by theory and observations, however, the samples of stars used to constrain MESA is likely going to be different from the survey used for analyzing the planet demographics. For instance, to estimate ζ in this study we used an underlying host star distribution that is log-uniform in mass, has a fixed metallicity ($Z = 0.014$) and age (3 Gyr), and identical planet multiplicity. These parameters may not be representative for a typical survey and thus the exact planet-host star distribution will impact the value of ζ. Furthermore, the value of ζ should be different for volume-limited and magnitude-limited surveys. In the latter case, observations are biased towards stars that are more luminous for a certain mass. Therefore, ζ for a magnitude-limited survey is likely to be higher than the ζ for a volume-limited survey. In a nutshell, to compare the predictions of different theories with observations, future observational studies should estimate ζ using their actual stellar sample.

5.4 Conclusions

In this work, we explore how the core-powered mass-loss mechanism shapes the radius valley for planets orbiting low mass stars such as M-dwarfs. For this purpose, we extended

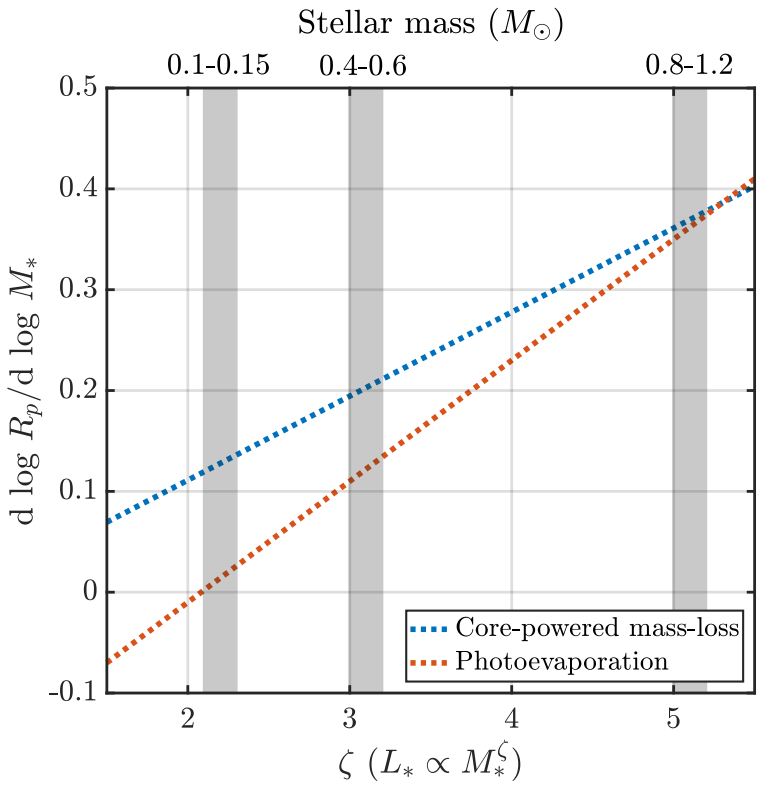

Figure 5.5: Comparison between the predictions of core-powered mass-loss and photoevaporation models for the variation in the radius valley slope in planet size-stellar mass space ($L_* \propto M_*^{\zeta}$) as a function of ζ (bottom x-axis) and stellar mass (top x-axis; *continued next page*).

Figure 5.5: Comparison between the predictions of core-powered mass-loss and photoevaporation models for the variation in the radius valley slope in planet size-stellar mass space ($L_* \propto M_*^{\zeta}$) as a function of ζ (bottom x-axis) and stellar mass (top x-axis). This figure demonstrates that the two mass-loss mechanisms predict increasingly different values for the slope of the radius valley in planet size-stellar mass space. Therefore, characterising the slope of the radius valley as a function of stellar mass around low mass stars may provide a fruitful avenue for distinguishing between core-powered mass loss and photoevaporation models. Two observational studies, Berger et al. (2020a) and Petigura et al. (2022), have measured the value of this slope as $0.26^{+0.21}_{-0.16}$ and $0.18^{+0.08}_{-0.07}$, respectively. Both these estimates however can't be directly compared with the predictions here as (1) ζ for the relevant (survey) stellar mass range are not known and (2) these values correspond to the slope of the valley for the entire range of $\sim$ 0.5-1.5 $M_{\odot}$ and not for smaller stellar mass bins. Nevertheless, these observed slopes are in the range expected from evolution under core-powered mass-loss $\sim 0.20 - 0.35$. In future studies, observers could compare how the radius valley slope in the planet size-stellar mass space changes with ζ which could then give us further proof if atmospheric escape dictates planet evolution, and if so indeed, which among photoevaporation or core-powered mass-loss, if any, is the primary driver of this process.

our previous work where we had investigated the influence of this mechanism on planets hosted by FGK dwarfs (Ginzburg et al., 2018; Gupta & Schlichting, 2019, 2020, 2021) by accounting for the luminosity evolution of lower mass stars, which can be especially significant for stars such as TRAPPIST-1. We simulated populations of millions of planets with an orbital period distribution based on observations (e.g. Petigura et al., 2022) but a planet mass distribution that is log-uniform. Choosing a log-uniform planet mass distribution allowed us to be agnostic to the yet unknown 'true' planet mass distribution given the uncertainties in how it scales with stellar mass.

We find that accounting for the evolution in the luminosity of FGK dwarfs instead of assuming a constant luminosity results in a negligible change in the size distribution of planets. This demonstrates that our assumption of a constant luminosity to model core-powered mass-loss for planets residing around FGK dwarfs in previous studies (e.g. Ginzburg et al., 2018; Gupta & Schlichting, 2020) was well justified. For stars of much lower masses, e.g. for a 0.1 $M_{\odot}$ star, we find however that the radius valley is narrower and less empty when we correctly account for stellar luminosity evolution. Nevertheless, the changes in the planet distribution are not significant when compared with the case where the luminosity is assumed to be constant in time. For instance, both models still predict the radius valley to be centered at roughly the same location in planet size and find the same slopes for the radius valley in planet-size orbital-period space.

In the planet size-orbital period space, we predict that the radius valley should have a negative slope of $\mathrm{d}\log R_p/\mathrm{d}\log P \simeq -0.11$ even around stars as small as 0.1 $M_{\odot}$, just as previously observed for FGK dwarfs (e.g., Van Eylen et al., 2018; Martinez et al., 2019) and more recently, even for M-dwarfs (e.g., Van Eylen et al., 2021; Petigura et al., 2022). The valley is however moves to smaller planet size around a lower mass star and in addition, is narrower and less empty. Furthermore, our results show that the slope of

the radius valley in the planet size-stellar mass parameter space does not stay constant with stellar mass but decreases in magnitude towards lower mass stars. Previously, we predicted a slope of d logR_p/d logM_* $\sim$ 0.34 around Sun-like stars, i.e. stars close to 1.0 $M_\odot$; see Gupta & Schlichting (2020). Because of the core-powered mass-loss' dependence of stellar luminosity, we demonstrate analytically and numerically that, if core-powered mass-loss is indeed dictating planet evolution, the radius valley slope should decrease to d logR_p/d logM_* $\sim$ 0.20 around early M-dwarfs, i.e. stars close to 0.5 $M_\odot$, and to $\sim$0.13 around late M-dwarfs, i.e. those with masses close to 0.1 $M_\odot$. As shown in this work, the slope of the radius valley in the planet size-stellar mass space is d logR_p/d logM_* = $(3\zeta - 2)/36$, where $L_*/L_\odot = (M_*/M_\odot)^\zeta$. For a larger (smaller) value of ζ, the slope in planet size-stellar mass space is also larger (smaller). Based on MESA-derived stellar evolution tracks, we find that ζ increases with stellar mass in the range $\sim$ 0.08-1.5 $M_\odot$. We thus find that the slope of the radius valley also increases (decreases) with increasing (decreasing) stellar mass and that the magnitude of the increase (decrease) can be directly calculated from from the mass-luminosity relation ($L_*/L_\odot = (M_*/M_\odot)^\zeta$.). Finally, we demonstrated that core-powered mass-loss and photoevaporation predict increasingly different slopes for the radius valley in the planet size-stellar mass space as one moves towards lower mass stars. Taken together, these findings provide us with new avenues to distinguish the signatures of core-powered mass-loss and photoevaporation observationally.

In this work, we have explored how the radius valley evolves around low mass stars if atmospheric evolution of planets is solely dictated by the core-powered mass-loss mechanism. Our results and predictions motivate the need for new observational studies and surveys that search for planet populations around low mass stars. Studies such as Cloutier & Menou (2020), Van Eylen et al. (2021) and Petigura et al. (2022) show some of the recent progress that has been made in this direction. Extending such studies and surveys

further to even lower stellar masses and larger datasets with the help of TESS (e.g. Ricker et al., 2015), CHEOPS (e.g. Benz et al., 2021), PLATO (e.g. Rauer et al., 2014) and other ground and space-based instruments, could accelerate efforts towards understanding which mechanism, if any, is the true cause shaping the radius valley and dictating the evolution of small exoplanets.

CHAPTER 6

The story of hydrogen and water: understanding the interaction between planet atmospheres and interiors using density functional theory

Studies show that the typical planet forms with a hydrogen atmosphere, resulting in conditions where hydrogen and the planet's molten or super-critical interior interact for millions to billions of years. How the atmosphere and interior interact is thus critical to understanding their formation, evolution, and interior structure. Our understanding of such interactions is, however, lacking. To address this, here we use a novel approach to conduct computational experiments based on the density functional theory to investigate how hydrogen and water — two of the most important planetary constituents — interact in the temperature and pressure range of 750-6000 K and 0.25-2000 GPa, respectively. Our results show that at a given temperature $\lesssim$ 6000 K, hydrogen and water are completely miscible at lower pressures but their phases separate with increasing pressure. At temperatures of $\gtrsim$ 5000 K, we find these constituents to be completely miscible, and hydrogen can in fact suppress the ability of water to crystallize into its superionic phase at higher pressures in general. We find that our results are consistent with laboratory experiments performed at lower temperatures and pressures. We demonstrate that planets such as Neptune and Uranus are likely to have significant regions in their interiors where hydrogen and water

are completely mixed and, at the same time, regions with compositional gradients. We identify where these regions lie in pressure depths and show that they are correlated with the changes in the observationally constrained density-pressure profiles for these planets. In addition, our results reveal that if Uranus is hotter than Neptune deep in the interior, the paradox of Neptune's higher internal heat flux compared to Uranus can be explained as a consequence of the gravitational energy released due to the greater degree of demixing of hydrogen and water in Neptune's interior. Furthermore, we identify regions where the ice giant magnetic fields are likely generated and discuss how the reason behind the difference in their magnitudes could also be explained by virtue of the mixing properties of hydrogen and water. Our work thus highlights how critical it is to understand the interaction between the planet atmospheres and interiors, especially as we move into the era of the James Webb Space Telescope, the proposed Uranian orbiter, and other next-generation observatories.

6.1 Introduction

The last three decades have transformed how we perceive our place in this universe. During this period, not only have we witnessed a plethora of robotic spacecrafts exploring distant worlds within our Solar system, but a revolution in observational astronomy has led to the discovery of thousands of planets in our neighborhood of the Milky Way galaxy. Yet, the ice giants of our Solar system, Uranus and Neptune, remain a mystery.

Today, we know that roughly every other star has a planet orbiting it. Furthermore, one of the most important discoveries from NASA's *Kepler* mission was that the most abundant class of planets, yet discovered, are those between the sizes of Earth and Neptune (e.g., Fressin et al., 2013; Petigura et al., 2013). Follow-up studies have since revealed that there are, in fact, two separate populations of planets here — the small, rocky super-Earths and

large, gas- and/or ice-rich sub-Neptunes — separated by a *radius gap* (e.g., Fulton et al., 2017; Rogers, 2015). Theoretical studies have demonstrated that most of these planets were part of the same primordial population which accreted hydrogen-dominated atmospheres. However, some of these planets eventually lost their atmospheres (e.g., Lopez & Fortney, 2013; Owen & Wu, 2013; Jin et al., 2014; Ginzburg et al., 2018; Gupta & Schlichting, 2019). These studies have also shown that these planets likely have Earth-like silicate-rich interiors, especially given their close proximity to their host stars — most of them exist within Mercury's orbit. However, it is possible that some might have water-rich interiors, like our Neptune or Uranus (e.g., Piaulet et al., 2023). What fraction of these small exoplanets are water-rich? This is difficult to say (e.g., Luque & Pallé, 2022; Rogers et al., 2023).

Nevertheless, water-rich worlds are likely abundant in our galaxy given that water is expected to have been as abundant as rock at distances beyond the ice line when planets were forming in our Solar system (e.g., Lodders, 2003). Furthermore, we do find an increasing prevalence of water and ice-rich planets and satellites in our Solar system at larger distances from the Sun, e.g., Europa and Enceladus. While, given technological limitations, there has been limited detection of truly Neptune- or Uranus-like planets, i.e., at similar planetary equilibrium temperatures, this is about to change. Ongoing and future observational surveys, especially those based on astrometry (e.g., *Gaia*; Casertano et al., 2008) and microlensing (e.g., *Nancy Grace Roman Space Telescope*; Penny et al., 2019), are primed to detect tens of thousands of planets within the next year to decade — ushering a new era in the field of planetary astronomy. A significant fraction of these planets will be in the category of those with sizes or masses similar to Neptune and Uranus and orbiting at distances of $\sim$ 1-100 AU (e.g., Gaudi, 2022). The detection of thousands of sub-Neptune and Neptune class planets will enable population-level studies of a magnitude never seen

before.

Of even more significant consequence will be the findings of instruments such as the James Webb Space Telescope and the next-generation high-resolution spectrographs, which will enable atmospheric characterization of super-Earths and sub-Neptunes to unprecedented degrees (e.g., JWST Transiting Exoplanet Community Early Release Science Team et al., 2023; Kasper et al., 2023). Findings from such instruments are expected to unravel new statistical trends in planet populations, such as, in atmospheric compositions. However, the fact is that we severely lack an understanding of the physical and chemical processes that dictate why atmospheres are the way they are.

It is thus evident that developing a comprehensive understanding of our Solar system's ice giants is more crucial than ever if we want to comprehend the formation, evolution, and prevalence of water-rich planets and their satellites, not just in our Solar system but across our galaxy. The ice giants of our Solar system, and planets such as Venus, provide one of the best testing grounds for our planet formation and evolution theories. Recognizing this, the latest Decadal Survey by the National Academy of Sciences for Planetary Science and Astrobiology has now recommended a mission to Uranus as its highest priority.

Even with our limited data on Uranus and Neptune, the Voyager 2 flyby and ongoing observations from space and ground-based observatories have revealed several fascinating aspects of these planets, which are seemingly more similar to being fraternal rather than identical twins. Uranus and Neptune not only have similar size, mass, and planetary equilibrium temperature but have also been reported to have a unique magnetic field topology dominated by quadrupolar and higher order terms (Connerney et al., 1987, 1991). Their magnetic fields are unlike those of Mercury, Earth, Jupiter, Saturn and Ganymede; all of which have dipole-dominated magnetic fields. This then suggests that the physical mode

of magnetic field generation in these two ice giants is likely similar. Stanley & Bloxham (2004, 2006) have demonstrated how their unique magnetic field morphology could be explained if it was being generated inside the planet in a thin, electrically conducting, convecting shell of thickness $\sim$ 20% of the planet size and at a depth of $\sim$ 0.6 times the planet radius. Though it should also be noted that the Uranian magnetic field is roughly 1.7 times stronger than that of Neptune (Kivelson & Bagenal, 2014). Nevertheless, the fact that these two planets resemble each other in so many aspects, suggests that they likely have a similar internal structure.

However, things get puzzling when one accounts for the observed internal heat flux from these planets, which are different by an order of magnitude, with Uranus having the lower luminosity. Explaining this difference between these ice giants that are otherwise so similar has been a long-standing challenge. For instance, certain theoretical studies have proposed that this could be because of the trapping of heat in the interior of Uranus, resulting in its lower heat flux (e.g., Hubbard et al., 1995). A number of intriguing theories have been put forward over the years; however, there is no consensus on the mechanism yet and usually, theories fail to explain both planets under the same framework (e.g., Vazan & Helled, 2020; Stixrude et al., 2021; Scheibe et al., 2021). In fact, studies also claim that Uranus is likely in equilibrium with the Sun and Neptune is the unusual planet. For example, work by Bailey & Stevenson (2021) showed that Neptune is likely releasing more energy than Uranus due to the demixing of hydrogen and water in its interior.

Past models have typically explored two scenarios for the interiors of planets such as Uranus and Neptune. In the first scenario, studies have typically assumed a stratified interior that is divided into several layers. An example is shown in the left panel of Figure 6.1. The layers are annotated to have pure hydrogen, as the atmosphere, and water, as the fluid or solid mantle or interior. But these two layers could similarly be assumed as a metal-poor

atmospheric layer and a metal-rich interior layer. For instance, Nettelmann et al. (2013) modeled the interior of Uranus and Neptune in an analogous manner. They assumed that the respective outer and inner envelopes are composed of hydrogen, helium and water with the outer envelope being dominated by hydrogen and helium, i.e., metal-poor, and the inner envelope being water-dominated, i.e., metal-rich. On the other hand, according to the other scenario, such planets might have a continuous compositional gradient from a hydrogen-rich region near the top of the planet to a water-rich region at increasing depths (e.g., Helled et al., 2011). Through observations of the Juno spacecraft, such compositional gradients have already been inferred near the core-envelope boundary for Jupiter (e.g., Wahl et al., 2017). However, as we demonstrate in this study, the reality is somewhere in between these two scenarios for planets such as Uranus and Neptune. Past studies such as Helled et al. (2011) have tried to model the internal structure of Uranus and Neptune with a parameterized profile that can account for a compositional gradient. But the internal structure inferred in this manner is not physical, as it is not grounded in how planet building materials, such as, hydrogen and water, interact. This has been a recent realization in the context of ice giants and sub-Neptunes, and more physically motivated models are now being actively developed to understand planets with interiors that are water or silicate rich (e.g., Markham & Stevenson, 2021; Misener & Schlichting, 2022).

While Bailey & Stevenson (2021) attempt to address this issue, their effort was limited by our lack of understanding of how hydrogen and water — the two major constituents of Neptune and Uranus and likely many exoplanets — interact with each other at relevant temperatures and pressures. Specifically, Bailey & Stevenson (2021) used the existing experimental data on when and how hydrogen and water mix with each other, but this is only available up to ~ 2 GPa and ~ 1000 K (Bali et al., 2013; Seward & Franck, 1981). The authors of this study thus extrapolated these findings to pressures of hundreds of GPa, i.e.,

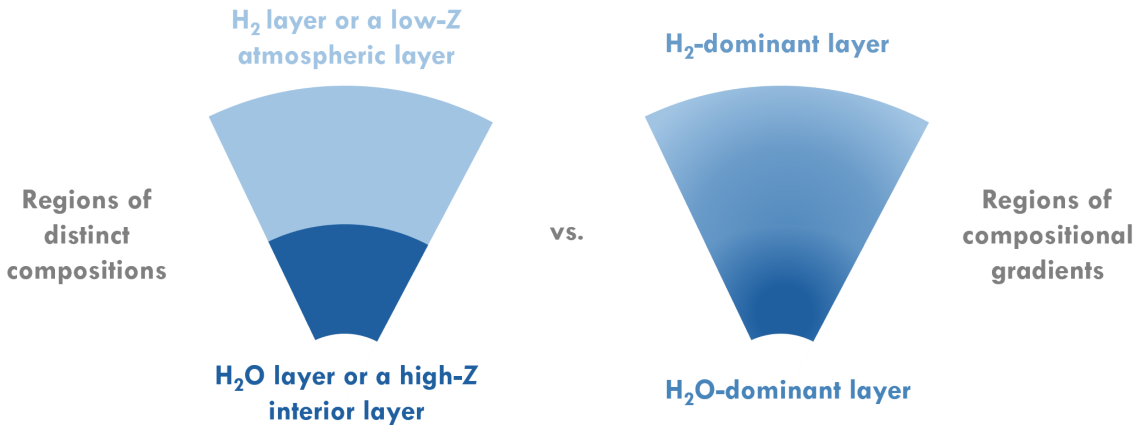

Figure 6.1: The two contemporary scenarios for the internal structure of a Neptune-like planet. On the left, we show the case where the internal structure is modeled as having two distinct layers. These could be pure H_2 and H_2O layers or equivalently, an outer, metal-poor atmospheric layer and an inner, metal-rich interior layer (see Section 6.1 for details). In the right panel, we show the case where the internal structure has a continuous compositional gradient instead. As we demonstrate in this work, the truth is likely a mixture of these both scenarios, at least for our Neptune and Uranus, and likely many exoplanets.

orders of magnitude away from the regime of the experiment. While there is a non-zero possibility that this simple extrapolation reflects reality, it could also be far from the truth. This highlights that while such models help gain insight into the mechanics of planets, they are critically limited by our lack of fundamental understanding of how planet building materials interact.

Unraveling this interaction between hydrogen and water is thus the subject of this study. Ultimately, we show how an improved understanding of the mixing in the interior of planets such as Uranus and Neptune could self-consistently explain their seemingly paradoxical observed attributes. The rest of this chapter is outlined as follows: In Section 6.2, we describe the concept of coexistence and critical curves, which forms the basis for understanding how any two components, such as hydrogen and water, mix into each other. Following this, we lay out the setup of our ab-initio computational experiments in Section 6.3. We then present our results Section 6.4 and discuss them in the context of the ice giants and exoplanets. Finally, we conclude this chapter in Section 6.5.

6.2 The concept of coexistence and critical curves

Let us consider a mixture of two arbitrary components, A and B. At any given temperature and pressure, their mixture will either be completely miscible in all proportions, i.e., exist as one phase, or partially miscible (and by extension, negligibly miscible or immiscible), i.e., exist as two separate phases. What exactly happens at a T/P condition depends on the Gibbs free energy of mixing A and B because any natural system evolves to minimize its total Gibbs free energy. The Gibbs free energy of mixing A and B, ΔG_{mix}, can be defined as

$$\Delta G_{mix} = \Delta H_{mix} \; - \; T\Delta S_{mix} \tag{6.1}$$

where ΔH_{mix} and ΔS_{mix} are the enthalpy and entropy of a solution, respectively. For an ideal solution, $\Delta H_{mix} = 0$, and the components always dissolve into each other as mixing two different components always increases entropy leading to a negative ΔG_{mix}. For a non-ideal solution, however, this depends on the magnitude of enthalpy of mixing. If the energy cost of mixing A and B is positive and high enough to overcome the negative entropy contribution, they will only mix to a certain degree.

In the latter scenario, given a temperature and pressure, there can be two coexisting equilibrium compositions of A and B which are the most stable, i.e., where the Gibbs free energy of the solution is negative and minimum (Putnis, 1992). The loci of these compositions are called coexistence curves and are depicted in pressure-composition (temperature-composition) phase space for a given temperature (pressure). In panel (c) of Figure 6.2, we show a typical example of such a curve. Above a critical pressure, P_c, A and B are entirely miscible outside this curve. Whereas below the critical pressure, A and B are miscible in all proportions.

The critical curve for the A-B system is the locus of these critical pressures and temperatures, as shown in panel (d) of Figure 6.2. This curve divides the temperature-pressure phase space into regions where A and B are miscible in all proportions and where they are only partially miscible. Hereafter, any reference to a 'critical temperature' or 'critical pressure' or, more generally, a 'critical point' will refer to a point on this critical curve.

Comparing a model temperature-pressure profile of a water-rich planet with a hydrogen atmosphere, such as Uranus or Kepler-138d (a potential water-rich exoplanet; Piaulet et al., 2023), with the critical curve of the hydrogen-water system can help us predict how the planet's interior is structured. Further delving into the relevant coexistence curve can then

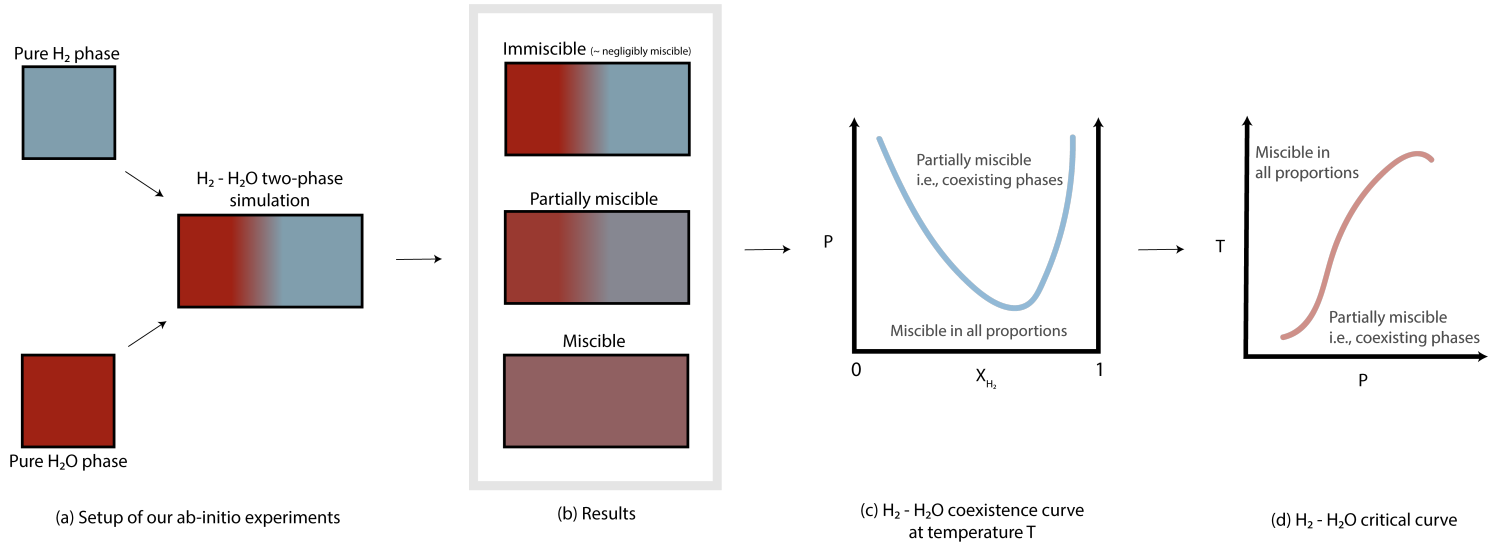

Figure 6.2: Methodology in a nutshell (*continued next page*).

Figure 6.2: Methodology in a nutshell. This figure summarizes our approach to understanding how hydrogen and water interact using density functional theory-based computational experiments. In panel (a), we show how our simulation setup involves preparing equilibrated phases of pure hydrogen and water at a certain temperature and pressure, which are then brought together and allowed to interact. These resulting two-phase simulations then equilibrate over time, and, as depicted in panel (b), depending on the Gibbs free energy of the mixture, either stay separated as two phases, partially mix into each other or become one uniformly mixed phase. These simulation results are then analyzed to determine the degree of mixing between hydrogen and water, which is then used to estimate the coexistence curves, as shown in panel (c). This helps determine the critical pressure (temperature) at a given temperature (pressure). These critical points are then used to determine the critical curve for the hydrogen-water system, as depicted in panel (d).

tell us how exactly the interior composition varies with depth or pressure and temperature. This work aims to map the coexistence and critical curve for the hydrogen-water system in the temperature-pressure phase space relevant to water-rich planets and exoplanets such as Uranus and Kepler-138d.

As alluded to earlier, experimental studies exist on the interaction of hydrogen and water, but these are limited — in number and in the phase space they explore. Later, we discuss how this past experimental data compare with our results.

6.3 Methodology: setup of our computational experiments

To study the hydrogen-water system, we employ the method of Born-Oppenheimer ab-initio molecular dynamics based on the Density Functional Theory (e.g., Kohn & Sham, 1965). To achieve this, we use the projector-augmented wave method (PAW; Kresse & Joubert, 1999) as implemented in the Vienna Ab-initio Simulation Package (VASP; Kresse & Hafner, 1993; Kresse & Furthmüller, 1996; Kresse & Furthmüller, 1996). H and O have valence configurations of ($1s^1$) and ($2s^2$ $2p^4$), respectively. For the exchange-correlation potential, we use the PBEsol approximation (Perdew et al., 2008). Previous studies have demonstrated that PBEsol yields good agreement with results from condensed matter experiments (Scipioni et al., 2017; Holmström et al., 2018, e.g.). We sample the Brillouin zone at the Gamma point and use a plane-wave cutoff of 500 eV.

With this setup, we perform canonical ensemble (*NVT*) simulations, i.e., simulations with a constant number of atoms (N), volume (V), and temperature (T) using the Nosé-Hoover thermostat (Hoover, 1985). As demonstrated in panel (a) of Figure 6.2, first of all, we equilibrate pure phases of water and hydrogen in a cubic simulation cell at a chosen temperature (T) and pressure (P). We initialize our simulations of pure water with an

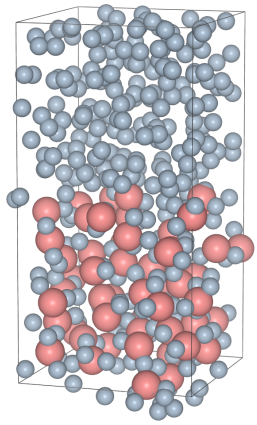

Figure 6.3: Snapshot of a two-phase simulation at t=0, conducted at 2000 K and ~ 30 GPa. This simulation instance involves 96 hydrogen and 54 water molecules (or equivalently, 54 oxygen and 300 hydrogen atoms). Hydrogen atoms are in blue and oxygen atoms are in red. Simulations employ periodic boundary conditions.

Ice X structure and the number of water molecules N_{H_2O} are kept fixed across all of our simulations at 54. The volume of the cell, V, is estimated given this set of $\{T, P, N_{H_2O}\}$, which is, in turn, used to estimate N_{H_2}. These pure phase simulations are then run with a time-step of 0.5 or 1 fs until temporal pressure deviations are within 1%. For simulations at pressures $\lesssim$ 0.5 GPa, we run simulations until these deviations are within 5%. Depending on the $\{T,P\}$ conditions, this takes ~ 5-50 ps. The exact time-step for a particular composition (pure hydrogen or water, or a mixture) and $\{T, P\}$ is chosen such that the energy drift is within ~ 2 meV/atom/ps.

We then bring together the equilibrated pure-phase simulations, as shown in panel (a) of Figure 6.2 and Figure 6.3, to perform two-phase water-hydrogen simulations across the relevant phase space of pressure and temperature. N ranges from anywhere between ~300 to 450 atoms, and we run these simulations until a compositional steady-state is reached

— typically lasting for ∼ 25 to 200 ps. These calculations were primarily performed on the UCLA Hoffman 2 Cluster and took roughly 3 million CPU hours.

As evident, our novel approach is conceptually simple and explores the process of mixing as expected to occur in nature. In addition, unlike other studies, our method involves no approximations or assumptions beyond those inherent to a numerical implementation of density functional theory, our choice of the associated exchange-correlation function, and the finite size of our simulated system. However, it comes at the cost of being computationally intensive.

6.4 Results and Discussion

We study the behavior of the hydrogen-water mixtures across temperatures of 750, 1000, 1500, 2000, 3000, 4000, and 6000 K and pressures spanning 0.25 to 2000 GPa to map out the coexistence and critical curves. In this section, we first elucidate how we analyze the raw results from our simulations to synthesize the coexistence curve. Following this, we discuss the characteristics of the resulting critical curve and what it implies for the formation, evolution, and interior structure of planets and exoplanets such as Uranus and Neptune.

6.4.1 Analyzing the equilibrated two-phase simulations

As our two-phase simulations evolve, the hydrogen-water system naturally matures into an equilibrium state where hydrogen and water are completely or partially miscible, as depicted in panel (b) of Figure 6.2. This behavior is further illustrated in Figure 6.4 where we share an example of our simulation results at T = 1500 K. In the top panels of this

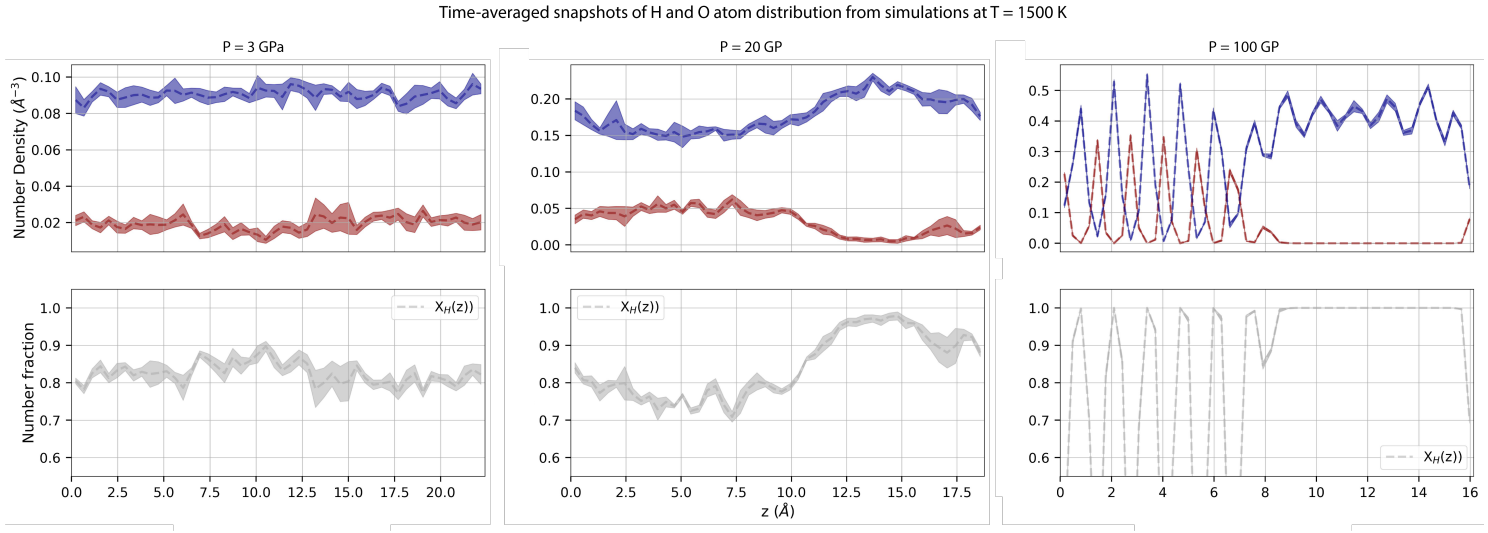

Figure 6.4: An example of simulation results from our two-phase ab initio computational experiments performed at 1500 K and for three different pressures (*continued next page*).

Figure 6.4: An example of simulation results from our two-phase ab initio computational experiments performed at 1500 K and for three different pressures. Profiles showing the distribution of atoms in two-phase simulation cells averaged over 10 ps. The three vertical panels, from left to right, show time-averaged (10 ps) snapshots of the distribution of H (in blue) and O (in red) atoms in the top row and X_H (in grey) in the bottom row along the long axis of the simulation cell, i.e., the axis along which the pure hydrogen and water phase simulations are connected. Dashed lines show the mean value of these distributions, whereas the shaded regions represent the uncertainties. These snapshots show how hydrogen and water are completely mixed at 3 GPa, partially mixed at 20 GPa, and in the 100 GPa case, water is in a crystalline phase, and hydrogen and water are immiscible.

figure, we show the number densities of O (in red; $N_O(z)$) and H (in blue; $N_H(z)$) as a function of z — the axis along which the equilibrated pure phases are merged, i.e., the long axis of our simulation cell; see Figure 6.3 for reference. The bottom panels of the figure further show how the number or (local) mole fraction of H, $X_H(z)$, changes, where $X_H(z) = N_H(z)/(N_H(z) + N_O(z))$. The dashed lines show the mean values, whereas the shaded regions surrounding them depict the 1 σ uncertainties in these estimates over a timescale corresponding to 10,000 simulation steps. This uncertainty is estimated using the blocking method laid out by Flyvbjerg & Petersen (1989) and accounts for the correlation in the data. From left to right, this figure shows how hydrogen and water become immiscible as one goes toward higher pressures. At low pressures of 3 GPa, we find water and hydrogen are completely miscible. Spatial variation in the relative composition of H and O atoms is comparable to the temporal uncertainties. At 20 GPa, in comparison, the two components are partially miscible. Here, the spatial variation in the relative composition of H and O

atoms is more significant than the temporal uncertainties. At even higher pressures of 100 GPa, conditions are such that water is in its crystalline state, Ice X, and we hardly see any miscibility. Since water is crystalline, the temporal uncertainties in relative compositions are negligible. No or negligible miscibility when one of the two components is crystalline is not surprising. However, as we discuss later, we find that hydrogen can suppress water's ability to crystallize. This fascinating behavior is more pronounced at higher pressures.

Given such data from our computational experiments, we estimate the coexistence curve for the hydrogen and water system. To remind the reader, a coexistence curve of the water-hydrogen mixture at a given temperature represents a locus of their most stable compositions across pressure space. Under the relevant nomenclature, the composition of hydrogen and water is defined as

$$X_{H_2} = \frac{N_{H_2}}{N_{H_2} + N_{H_2O}} \text{ and } X_{H_2O} = 1 - X_{H_2}, \tag{6.2}$$

i.e., as their respective mole or number fractions. To estimate X_{H_2} and map out the coexistence curve, we first determine X_H and use two approaches.

Firstly, we use the theoretically motivated hyperbolic tangent fit (e.g., Cahn & Hilliard, 1958) to the X_H mole fraction profiles as shown in the bottom panel of Figure 6.4. The functional form for this profile can be expressed as

$$X_H(z) = X_{H,\text{off}} + (X_{H,\text{cm}} - X_{H,\text{off}}) \times (\Gamma_p - \Gamma_m), \text{ where} \tag{6.3}$$

$$\Gamma_p = \tanh\left(\frac{(z - z_{\text{cm}}) - [z - z_{\text{cm}}] + z_w)}{\delta}\right) \text{ and} \tag{6.4}$$

$$\Gamma_m = \tanh\left(\frac{(z - z_{\text{cm}}) - [z - z_{\text{cm}}] + z_w)}{\delta}\right). \tag{6.5}$$

In these equations, 'off' and 'cm' subscripts correspond to the X_H values for regions that are poor and rich in H, respectively. z_{cm} and z_w refer to the location and width of the

H-rich phases where the maximum value of z, i.e., the length of the simulation cell, has been normalized to 1. δ is the width of the interface between the rich and poor phases and relates to aspects of the interaction between the two phases (e.g., Cahn & Hilliard, 1958). Finally, we use the notation [.] to express that the value inside the brackets is rounded to the nearest integer. This term then helps account for the periodic boundary conditions of our simulation cell (Insixiengmay & Stixrude, in prep.). We use Bayesian inference analysis to fit this equation to the X_H profiles. Specifically, we use the Dynamic Nested Sampling method (Skilling, 2004, 2006; Higson et al., 2019) as implemented in the open-source code `dynesty` (Speagle, 2020; Koposov et al., 2023).

Secondly, we use a simple statistical approach to determine X_H. For this, we determine $X_{H,\mathrm{off}}$ and $X_{H,\mathrm{cm}}$ by determining the temporal and spatial averages of the highest and lowest points in the profiles. At any time instant, we take an average of $X_H(z)$ across ten percent of the box length centered at the extrema of the profiles and repeat this across three time-blocks of 10,000 time-steps. We repeat the same procedure with the associated errors. Then X_{H_2} is simply $1 - (2/X_H)$. We show the corresponding values across the temperature-pressure space in Figure 6.5.

To then determine the critical pressure at a given temperature, we exploit the fact that the chemical potentials, $\mu_{H_2,\{1,2\}}$, for the two equilibrium compositions of hydrogen, $X_{H_2,\{1,2\}}$, at a given pressure and temperature, are the same, i.e., $\mu_{H_2,1} = \mu_{H_2,2}$ (e.g., Putnis, 1992). We assume that the excess Gibbs free energy of mixing, $G_{mix,ex}$, can be expressed as

$$G_{mix,ex} = W_G X_{H_2} X_{H_2O} \tag{6.6}$$

where W_G is the Gibbs free energy interaction parameter. As evident from Figure 6.5, the coexisting equilibrium phases are asymmetric about $X = 0.5$. We thus introduce

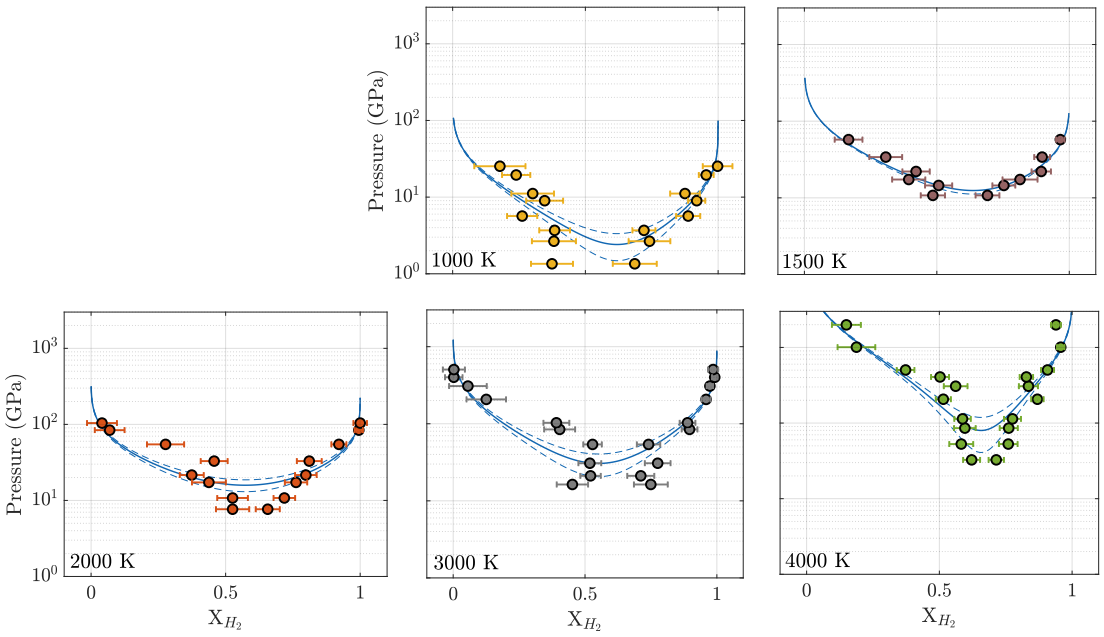

Figure 6.5: Coexistence curves across temperature-pressure-composition space. Each panel in this figure shows the relative fraction of hydrogen X_{H_2} in the hydrogen-rich and -poor phases — the most stable phase compositions at the respective pressures and temperatures. The error bars denote the 1 sigma uncertainty in the compositions and pressures. These data points are then fit to Equation (6.7), the solution to which is shown with a solid line. The dashed lines enclose the 1 sigma confidence interval to these fits.

an asymmetry parameter λ to capture this such that $X_{H_2,1} = \lambda(1 - X_{H_2,2})$. Given that $\mu = \partial G/\partial X$ and $\mu_{H_2,1} = \mu_{H_2,2}$ on the coexistence curve, at a given temperature and pressure, we solve the resulting equations to get the following relation

$$P = \frac{1}{W_V}\left(\frac{\log\left(X_{H_2}\right) - \log\left(\lambda(1 - X_{H_2})\right)}{2X_{H_2} + \lambda X_{H_2} - \lambda X} - W_0\right). \tag{6.7}$$

W_V and W_0 are interaction parameters such that $W_G = W_H - TW_S + PW_V = W_0 + PW_V$ and $W_\Phi = \Delta\Phi X_{H_2} X_{H_2O}$ with $\Phi \in \{H, S, V\}$. Subscripts H, S, and V stand for enthalpy, entropy, and volume, respectively. We then fit this expression to the X_{H_2} data using the Levenberg-Marquardt algorithm with the Least Absolute Residuals (LAR) criterion. We choose the LAR criterion given that our data can be quite noisy, and this criterion is relatively robust against outliers. We find that the results from either approach are within 1 sigma.

As shown in Figure 6.5, our results can thus help us determine how the equilibrium composition of hydrogen and water changes with temperature and pressure. Though strictly speaking, the second approach is only suitable for determining critical points rather than the equilibrium compositions as it underestimates the magnitude of mixing. Thus, using the first approach is more appropriate in this context. In theory, these values of equilibrium compositions or the corresponding coexistence curves can be used to construct more accurate interior models for water and ice-rich planets. However, such an exercise is outside the scope of this work, but we plan to explore this in a future study with relevant equations of state.

As mentioned earlier, the hydrogen-water coexistence curves are asymmetric and skewed towards a hydrogen-rich composition. This skewness implies that hydrogen is more soluble in water than vice-versa, likely due to the difference in the sizes of the respective molecules: hydrogen is much smaller than a water molecule, and this difference

gets more pronounced at higher pressures. Furthermore, adding hydrogen to water should lead to more hydrogen bonds, likely making a hydrogen-rich mixture energetically more favorable. The skewness towards a higher X_{H_2} becomes more pronounced at higher pressures and temperatures. This behavior is apparent from the steepness of the coexistence curves, which increases with temperature. We do not show any coexistence curve for 6000 K because, at this temperature, we do not find any substantial evidence for immiscibility at any pressure up to 2000 GPa.

Finally, we find that the critical pressure P_c increases in magnitude with increasing temperature. Note that the y-axis is in logarithmic space across the plots in Figure 6.5. The difference in P_c across temperatures is thus more substantial than it might appear. This trend is more apparent in Figures 6.6 and 6.7 where we present how the critical curve varies in the temperature-pressure phase space.

6.4.2 Good agreement with experimental data

In Figure 6.6, we present the critical curve for the hydrogen-water system across the temperature-pressure space. The temperature range we explore extends from 750 K to 6000 K, whereas pressure ranges from 0.25 GPa (2.5 kbar) to 2000 GPa (20 Mbar). Each filled circle represents one of our numerous two-phase simulations. Their colors denote the final composition of the hydrogen-water mixture at the respective temperature and pressure: the darkest shade of blue represents complete mixing, whereas the intermediate and lightest shades represent partial or negligible to no mixing, respectively. The gray dotted line represents the critical curve for the hydrogen-water system constructed using spline interpolation against the critical conditions calculated across the temperature-pressure space. This line thus divides the temperature-pressure phase space into regimes where hydrogen

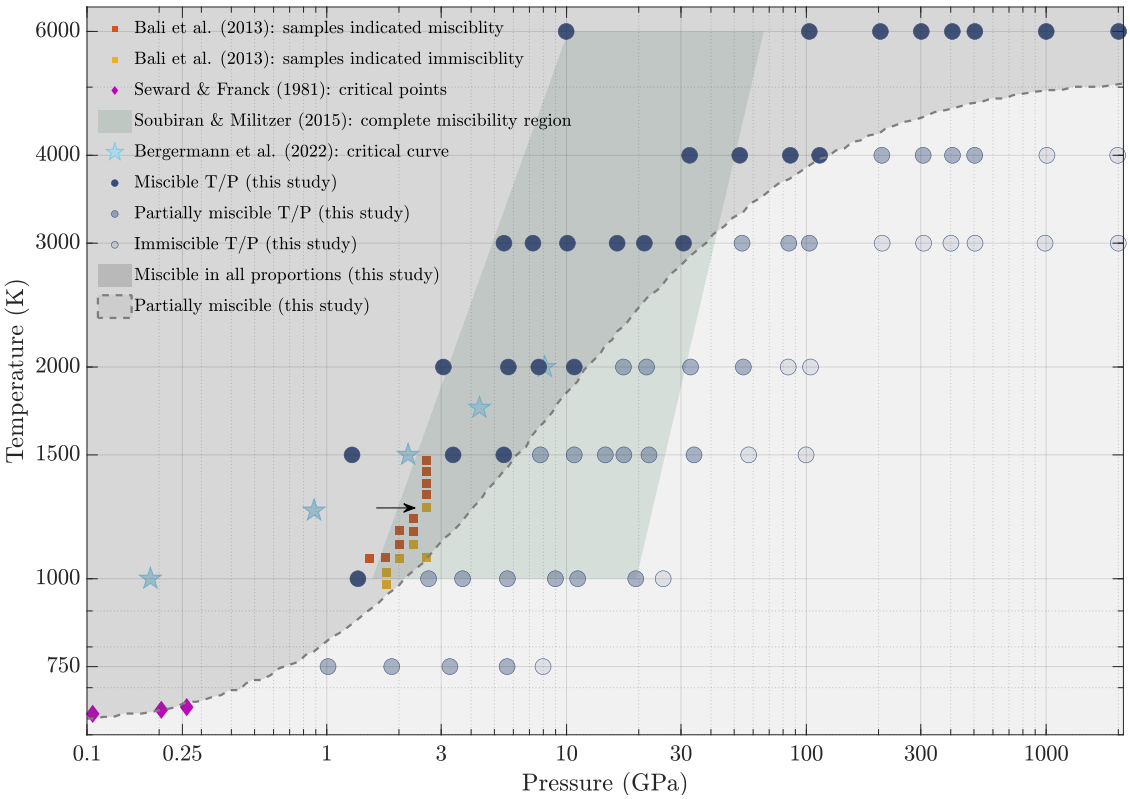

Figure 6.6: Comparison of our results with past experimental and computational studies. In this figure, we plot the critical curve obtained from our study alongside past experimental data on the hydrogen-water system from Seward & Franck (1981) and Bali et al. (2013). Our results are in good agreement with those reported by Bali et al. (2013) and consistent with those from Seward & Franck (1981). In addition, we also plot results from the past computational studies by Soubiran & Militzer (2015) and Bergermann et al. (2021). Unlike our work, both these computational studies are quite inconsistent with experimental data. We attribute this to the approximations in these past computational studies, such as the use of pair potentials.

and water mix in all proportions (shaded dark gray) and where they are only partially miscible/immiscible (shaded light gray).

We then also summarize the available data on the hydrogen-water system from experimental studies by Seward & Franck (1981) and Bali et al. (2013), and computational studies by Soubiran & Militzer (2015) and Bergermann et al. (2021). We leave a detailed discussion on the characteristics of the critical curve to Section 6.4.3 and instead limit ourselves to comparing our results with these past studies here. Seward & Franck (1981) estimated the location of the critical points for the water-hydrogen system at temperatures and pressures close to $\sim$ 650 K and $\sim$ 0.1 GPa. Magenta diamonds denote these critical points. Bali et al. (2013) performed experiments at temperatures and pressures of $\sim$ 1250 K and $\sim$ 2 GPa. The conditions in which they found hydrogen and water to be completely miscible are marked with orange squares, whereas where they found them to be immiscible are marked with yellow squares. The green-shaded region corresponds to the study by Soubiran & Militzer (2015), and they find hydrogen and water to be completely miscible across this entire parameter space. Lastly, the sky-blue stars represent the critical points determined by Bergermann et al. (2021).

As evident from Figure 6.6, the results of computational studies performed by Soubiran & Militzer (2015) and Bergermann et al. (2021) had significant disagreement with experimental data. For instance, Bali et al. (2013) found that the water-hydrogen system has a critical point at roughly 2 GPa at 1250 K. However, Soubiran & Militzer (2015) do not find evidence of this even up to pressures of $\sim$20 GPa. Soubiran & Militzer (2015) used a complex interplay of force and energy calculations that are partially based on (1) pair potentials and (2) density function theory, to ultimately estimate the Gibbs free energy of the hydrogen-water system using the method of thermodynamic integration. Soubiran & Militzer (2015) do not explore conditions close to those investigated by Seward & Franck

(1981). Results reported by Bergermann et al. (2021) are inconsistent with the experimental results of both Bali et al. (2013) and Seward & Franck (1981). Bergermann et al. (2021) use calculations purely based on pair potentials. As the authors of this study themselves note, while this approach is very computationally efficient in comparison to density functional theory-based simulations, the use of pair potentials can lead to inaccurate results since interactions based on pair potentials do not capture several physical aspects pertinent to atomic and molecular interactions such as changes in electronic structure with temperature and pressure or dissociation. Both studies, Soubiran & Militzer (2015) and Bergermann et al. (2021), likely yield inaccurate results given their reliance on pair potentials.

Nevertheless, Soubiran & Militzer (2015) attribute the discrepancy with the experimental results of Bali et al. (2013) to the presence of silicates in the latter's experimental samples. While we agree with their reasoning on qualitative grounds, i.e., contamination of samples with silicates should alter the mixing behavior when compared to that of a non-contaminated sample, it is surprising that they do not see any mixing at all, even at pressures higher by an order-of-magnitude. Thus, this discrepancy likely stems from the use of pair potentials in the calculations by Soubiran & Militzer (2015). Bali et al. (2013) themselves noted that the presence of silicates could lead to a shift in their critical curves away from what would be expected for a pure water-hydrogen system. However, they pointed out that the presence of silicates was minimal and believed that such impurities should only result in a slight shift in the temperature-pressure space. Indeed, this is exactly what we find.

As evident from Figure 6.6, our results are in good agreement with the experimental data of Bali et al. (2013) and also consistent with the findings of Seward & Franck (1981). We thus find minimal to no discrepancies between the material behavior found in experimental data and that predicted by the density functional theory.

Though, we note that the slope of the critical curve predicted by Bali et al. (2013) at pressures of $\sim$ 2 GPa is steeper than we find. However, this discrepancy can be entirely attributable to a single data point, indicated by an arrow in Figure 6.6. If we remove this single data point, even the slopes are in good agreement. It is thus possible that the referenced sample was compromised in some way.

6.4.3 Characteristics of the critical curve for the hydrogen-water system

In Figure 6.7, we present the critical curve for the hydrogen-water system in the context of the physical properties of pure water and hydrogen, and Uranus and Neptune. Specifically, we plot the different phase boundaries for hydrogen and water: the H_2O melting curve (blue dashed line; Millot et al., 2019), H_2O solid insulator to superionic boundary (orange dashed line; French et al., 2016) and H insulator to semi-metal, to metal boundary (brown and grey dotted lines, respectively; McWilliams et al., 2016, and references therein).

Not only are we finding that with increasing pressure and temperature, hydrogen and water become less miscible but also that they are nearly immiscible the closer one gets to the H_2O melting curve, i.e., the more crystalline water gets, especially at temperatures of $\sim$ 750 to 1500 K. This, however, begins to change towards higher temperatures $\sim$ 2000 - 4000 K. Close to these temperatures, we observe that the presence of hydrogen suppresses the freezing of H_2O given the significant amount of mixing we find to the right of the H_2O melting curve. We predict this is likely due to the change in the structure of the H_2O ice. At conditions within the H_2O solid insulator-superionic boundary, H_2O is in the Ice X phase. Above this curve and thus at temperatures of $\gtrsim$ 2000 K, H_2O is in a superionic phase — Ice XVIII (e.g., Millot et al., 2019). Superionic ice consists of an oxygen lattice surrounded by mobile hydrogen ions with a stoichiometric ratio of 1:2. As discussed previously, if

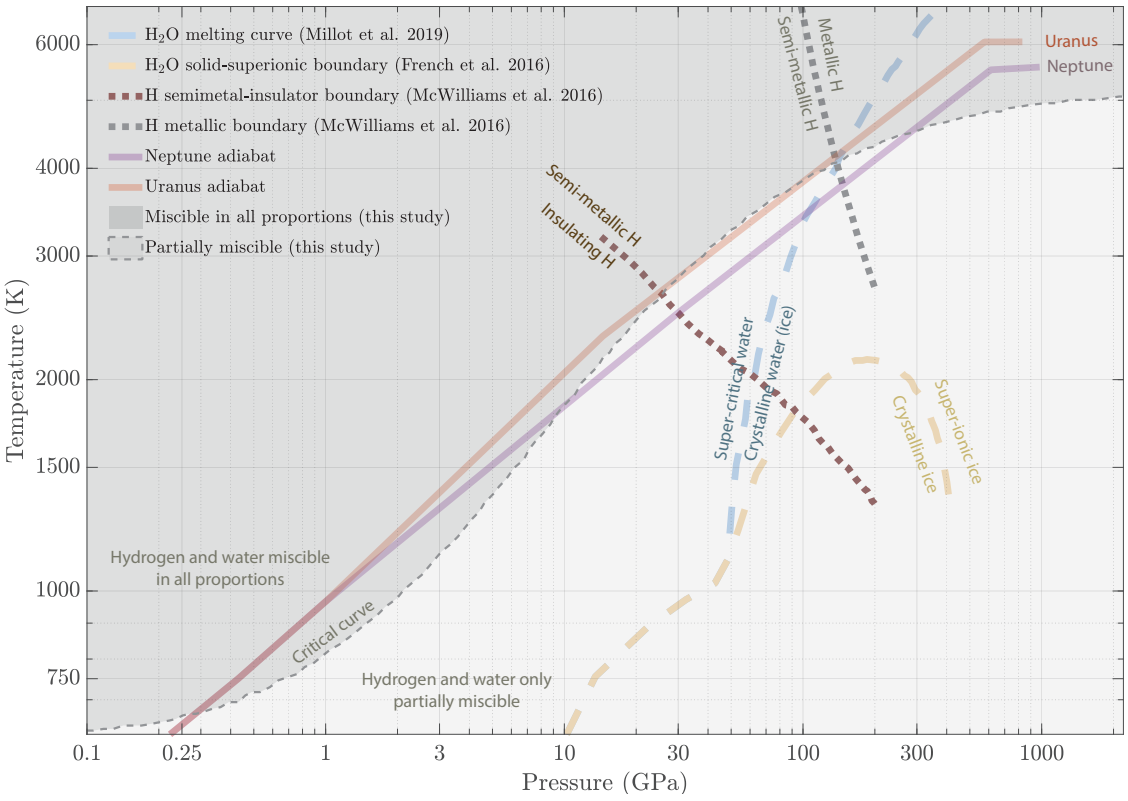

Figure 6.7: Critical curve for the hydrogen-water system. This plot shows how the critical curve for the hydrogen-water system varies across the pressure-temperature space. We also plot water-ice melting curve (Millot et al., 2019), water solid-superionic boundary (French et al., 2016), and the hydrogen insulator to semi-metal boundary and the boundary predicting metallization of fluid H (McWilliams et al., 2016). In addition, we also plot adiabats for Neptune and Uranus as calculated by Nettelmann et al. (2013) assuming a three-layer model for their interior. As evident from the comparison of the Neptune adiabat with the critical curve, Neptune is expected to have large regions of completely miscible interior along with regions of compositional gradients. While Uranus should also have similar regions, if it is indeed hotter than Neptune in its deep interior, the magnitude of any such gradients will be lower.

two components mix or not, depends on the Gibbs free energy of mixing, which, in turn, depends on the entropy and enthalpy of mixing. Around temperatures of 750-1500 K, pure water-ice begins to crystallize at higher pressures, so evidently, the energy cost to break it and mix it with hydrogen molecules must be high. Therefore, mixing between hydrogen and water molecules will become unfavorable as pressure increases. In other words, the enthalpy of mixing gets larger at higher pressures, becoming so large closer to the ice line that mixing is thermodynamically infeasible. At even higher temperatures of 2000-4000 K, since hydrogen ions in Ice XVIII are already mobile, it appears that the enthalpy of mixing is not as significant. On the other hand, the negative contribution of the entropy of mixing term is more substantial as it is $\propto$ T.

Things change further at temperatures of $\sim$ 4000 to 6000 K. At these temperatures, we find that the slope of the critical curve decreases rapidly, becoming almost zero at $\sim$ 5000 K. And we do not find any clear evidence of hydrogen-water immiscibility at 6000 K, all the way up to pressures of 2000 GPa. Note that the X-axis is in logarithmic scale. Beyond 100 GPa, the critical curve temperature hardly changes even as pressure increases to 2000 GPa. This change in behavior closely follows the predicted metallization of hydrogen as depicted by the gray dotted line in Figure 6.7 and appears to suggest that the critical curve could turn over. However, we do not find any clear evidence of this, at least up to pressures of 2000 GPa. For instance, even at 2000 GPa, water is crystalline at temperatures of 3000 to 4000 K.

6.4.4 Insights into the formation, evolution, and internal structure of planets

To put our results in the context of the formation, evolution, and interior of water-rich planets and exoplanets, we also include the adiabats for Neptune (purple) and Uranus (red)

in Figure 6.7. These adiabats approximately follow those estimated in Nettelmann et al. (2013). In their work, Nettelmann et al. (2013) assumed that Uranus and Neptune have an interior best described by three distinct layers: a rocky interior surrounded by an inner, metal-rich and an outer, metal-poor envelope composed of hydrogen, helium and water. The inner, metal-rich envelope is water-dominated whereas the outer, metal-poor envelope is dominated by hydrogen and helium. To then constrain these adiabats (and the relative amounts of hydrogen, helium and water in the inner and outer envelopes), they used our knowledge of the planet's mass, radius, surface pressure, rotation rates, and J_2/J_4 gravity data. Back in 2013, this work by Nettelmann and collaborators was state-of-the-art, using all the latest evidence on the physical properties of these two planets and that on their assumed constituents. However, as we discuss below, comparing these adiabats to our results shows that their model of the ice-giant internal structure requires improvements.

In addition, in Figure 6.8, we show a comparison of our results (middle panel) with density-pressure profiles for Neptune (left panel) and Uranus (right panel) based on observational constraints. In the middle panel here, we reproduce the plot from Figure 6.7 and present plots from Figure 12 of Movshovitz & Fortney (2022) in the other panels. To determine these density-pressure profiles, Movshovitz & Fortney (2022) used a parameterized function to satisfy the constraints from the following properties of the respective planets: mass, radius, rotation period, and J_2, J_4 gravity coefficients. Each panel is divided into four Parts, namely, $A \in [10^{-5}, 5 \times 10^{-3}]$ Mbar, $B \in [5 \times 10^{-3}, 2 \times 10^{-1}]$ Mbar, $C \in [2 \times 10^{-1}, 2]$ Mbar and $D \in [2, 5]$ Mbar where 1 Mbar = 100 GPa. The pressures where one *Part* switches to another approximately align with the pressure depth where the slope of the density-pressure curves/bands change in the left and right panels. At the same time, this also correlates with pressure depths where the critical curve and the Neptune and Uranus adiabats crossover each time. This correlation is thus tentative evidence showing

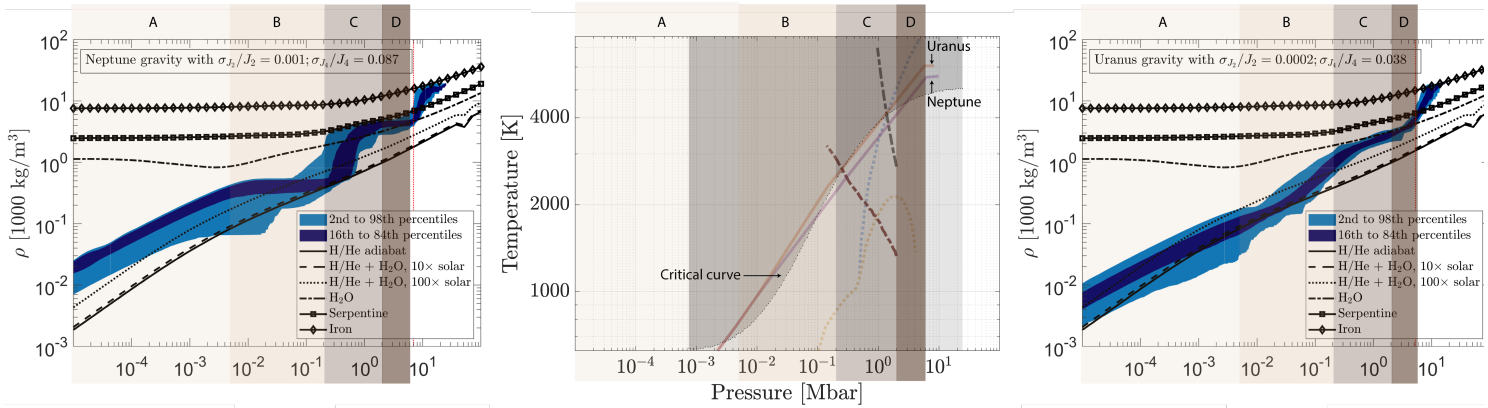

Figure 6.8: Comparison of our results (middle panel) in temperature-pressure phase space with the observational constraints on the density-pressure profiles for Neptune (left panel) and Uranus (right panel) calculated by Movshovitz & Fortney (2022); reproduced here with permission from Naor Movshovitz (*continued next page*).

Figure 6.8: Comparison of our results (middle panel) in temperature-pressure phase space with the observational constraints on the density-pressure profiles for Neptune (left panel) and Uranus (right panel) calculated by Movshovitz & Fortney (2022); reproduced here with permission from Naor Movshovitz. The middle panel is the same as Figure 6.7. The density-pressure profiles from Movshovitz & Fortney (2022) are estimated using a parameterized function, fit to best satisfy the observables of the two planets, i.e., their mass, radius, rotation period and gravity coefficients. In the left and right panels, the dark blue band represents the density-pressure profile at 1 sigma confidence, whereas the light blue band corresponds to a 2 sigma confidence estimate. Each panel is divided into four highlighted 'Parts' corresponding to the same pressure range: $A \in [10^{-5}, 5 \times 10^{-3}]$ Mbar, $B \in [5 \times 10^{-3}, 2 \times 10^{-1}]$ Mbar, $C \in [2 \times 10^{-1}, 2]$ Mbar and $D \in [2, 5]$ Mbar where 1 Mbar = 100 GPa. The transition pressure between adjacent *Parts* roughly aligns with the pressure at which the slope of the density-pressure profiles change. Comparing these transitions with the middle plot reveals that these transitions are correlated with each crossover between the hydrogen-water critical curve and the Neptunian and Uranian adiabats taken from Nettelmann et al. (2013). In other words, this agreement is evidence that mixing between hydrogen and water plays a critical role in the interior of ice giants, and our results help elucidate the compositional transitions present inside these planets.

that these crossovers between the critical curve and the adiabats reflect the compositional and structural changes present in the interior of Neptune and Uranus. Below, we have a more detailed look into this.

6.4.4.1 Internal structure: multiple homogeneous regions and compositional gradients

For the purpose of the following discussion, let us only focus on Neptune's adiabat until stated otherwise. As evident from Figure 6.7, this adiabat is above the critical curve at pressures between $\sim$ 0.5 to 20 GPa. These pressure depths correspond to the Part *B* from Figure 6.8. The fact that the adiabat is above the critical curve implies that Neptune's hydrogen-rich atmosphere and water-rich interior at these pressure depths should be thoroughly mixed, i.e., there should be one phase of a water-hydrogen mixture. At pressure depths progressively below $\sim$ 0.5 GPa, i.e., in Part *A*, Neptune should have a hydrogen-dominated atmosphere with progressively less water fraction. As suggested by the experimental results of Seward & Franck (1981), the hydrogen-water critical curve is relatively shallow at the corresponding low temperatures and pressures. Therefore, while it is possible for convective mixing to increase the amount of water at even lower pressure depths, thermodynamically, the allowed water fraction in a hydrogen-dominated atmosphere decreases steeply with pressures below $\sim$ 0.5 GPa.

At pressure depths $\gtrsim$ 20 GPa and $\lesssim$ 200 GPa, i.e., in Part *C*, we find that the Neptune adiabat again enters a phase space where water and hydrogen start to separate or become only partially miscible. In other words, as one goes deeper inside Neptune, we predict Neptune's interior should be increasingly rich in water and poor in hydrogen. This change should lead to a progressively denser interior that is more similar to pure water than

hydrogen.

Finally, beyond pressures of ~200 GPa, the adiabat enters a regime where hydrogen and water are completely miscible. On top of this, in this temperature-pressure regime, not only is pure water in the superionic crystalline phase, but pure hydrogen is predicted to become metallic. It thus seems that Neptune's interior is likely highly conductive at this depth, and this region corresponding to Part *D*, between roughly 200 to 500 GPa, is the thin conductive, convective shell where Neptune's quadrupole-dominated magnetic field is likely generated (e.g., Stanley & Bloxham, 2004, 2006). Although, as noted earlier, studies in the past predicted that at these pressure depths, the interior is likely in a superionic crystalline phase of water Millot et al. (e.g., 2019), we find that the presence of hydrogen can suppress water's ability to crystallize. This behavior would then result in a fluid phase of mixed hydrogen and water. More work is, however, required to better characterize this unexpected fluid phase that might be present in Neptune's interior. The rationale for the higher limit on the pressure of Part *D* is that there is likely another compositional transition at roughly such depths in Neptune and Uranus. Such a transition is indicated by the change in the slope of the density-pressure profile at the pressure of ~ 500 GPa — a likely transition to a rocky core. However, this inference is speculative at the moment. We plan to explore the electrical conductivity of the hydrogen-water mixture at these conditions more thoroughly in future work.

A comparison of Uranus' adiabat with the critical curve shows that Uranus, too, has similar internal structural and compositional transitions as present in Neptune. However, if Uranus is indeed hotter in its deep interior, as suggested by these adiabats from Nettelmann et al. (2013) and shown in Figures 6.7 and 6.8, any compositional gradient inside Uranus will be less pronounced when compared with Neptune because hydrogen and water would be more mixed given hotter temperatures. Movshovitz & Fortney (2022) found precisely

this – a relatively muted density-pressure profile for Uranus inferred from observational constraints. This further illustrates the relevance of our results and the importance of understanding the interaction between hydrogen and water inside Neptune and Uranus.

6.4.4.2 Solution to the ice-giant luminosity paradox: thermal evolution and demixing

Now imagine a much younger Neptune, which must have been hotter than it is today. The adiabat of this younger Neptune would have lied at higher temperatures than the one plotted in Figure 6.7, which, in turn, implies that Neptune must have long had an interior ($\gtrsim$ 0.1 GPa) where hydrogen and water were completely mixed, as a single phase of fluid, everywhere. Over time, as the planet has cooled, hydrogen and water must have started to demix. This demixing process must have then led to the release of gravitational energy, which likely continues. Separation of hydrogen and water is likely happening in Uranus' deep interior too. However, if Uranus is indeed hotter than Neptune on the inside, its adiabat would be closer to the critical curve than Neptune's adiabat as seen in Figure 6.7. If so, hydrogen-water demixing has happened to a much lower degree in Uranus or is just beginning, implying that much less gravitational energy has been released inside Uranus than in Neptune. This excess energy from demixing in Neptune is thus the likely reason behind Neptune's excess luminosity compared to Uranus.

As discussed earlier, this has been suggested before. We build upon the idea posited by Bailey & Stevenson (2021), who attempted to demonstrate this for Neptune but were limited by a lack of understanding of how water and hydrogen interact in relevant conditions. Even earlier, Stevenson & Salpeter (1977a,b) used the same concept to explain the excess luminosity of Saturn, given the immiscibility of hydrogen and helium ('helium rain'). Our work presents the first evidence, with the accuracy of density functional theory, that

Neptune is experiencing something similar — allowing us to elucidate the physical and chemical processes behind the observed difference in the ice giant luminosities, within the same framework. This does not mean that the processes laid out by previous studies are unimportant or do not occur in nature. However, it seems likely that the dominant cause behind the ice giant luminosity paradox is the release of gravitational energy due to the demixing of hydrogen and water.

6.4.4.3 Magnetic field: the source and differences in strength

Ice-giant have distinct magnetic fields that are highly non-dipolar, whereas all other planetary bodies, from Earth to Jupiter to Ganymede, have dipole-dominated magnetic fields. To explain this puzzling behavior, studies have suggested that the source of the ice-giant magnetic fields source should be a thin, highly conductive, convecting shell of fluid deep inside these planets Stanley & Bloxham (e.g., 2004, 2006). As discussed earlier, it is thus likely that the region approximately encapsulated by the Part *D* shown in Figure 6.8 is the source for magnetic field generation in both planets.

Furthermore, something that is not often discussed is the difference in the surface magnetic field strengths of ice giants, despite having similar mass, size, and magnetic field morphologies: Uranus and Neptune have surface magnetic field strengths of 0.23 and 0.13 Gauss, respectively (Lang, 1992), i.e., Uranus has a magnetic field stronger by ~ 1.7 times. The mixing properties of hydrogen and water also hint at the answer to this observation. If Uranus is hotter than Neptune, as suggested in Nettelmann et al. (2013) and other studies, then the region with characteristics attributed to Part *D* should be larger for Uranus than Neptune. In other words, Uranus likely has a relatively thicker shell of highly conductive, convecting fluid than Neptune. The electrical conductivity of this shell is also likely higher

for Uranus, given higher temperatures. If indeed true, this naturally explains why Uranus should have a higher magnetic field strength than Neptune.

Finally, we note that comparing the adiabats from Nettelmann et al. (2013) with our hydrogen-water phase diagrams is, technically, not self-consistent. While one can estimate how the density inside Neptune or Uranus varies with depth or pressure using observational data (e.g., Movshovitz & Fortney, 2022), an equation of state is needed to estimate how temperature varies with depth or pressure. To know the equation of state at any depth, one needs to know the composition there. Given that the interior model by Nettelmann et al. (2013) requires adjustments given how hydrogen and water interact, comparing their adiabats with our hydrogen-water phase curves is not a self-consistent exercise. In addition, we also neglect the effect of gravity, which could make a heavier constituent differentiate or fractionate to larger depths. Nevertheless, as evident from the discussion in this section, such a comparison clearly sheds light on the physical and chemical processes that are critical to understanding the interior structure of planets such as Uranus and Neptune, helps us make tentative predictions on their evolution and current internal states, and shows a pathway for future theoretical and observational investigations.

6.5 Conclusion

In this study, we performed Density Functional Theory based ab-initio molecular dynamics simulations to investigate the interaction between hydrogen and water. Specifically, we explore the behavior of hydrogen-water mixtures at temperatures and pressures ranging between 750 to 6000 K and 0.25 to 2000 GPa, a range relevant to the interiors of planets and exoplanets such as Uranus and Neptune. In this temperature-pressure regime, we map out the coexistence and critical curves for the hydrogen-water system and discuss the

implications of the mixing and separation of these two components in the formation and evolution of such planets.

We use the coexistence curves to estimate the critical conditions beyond which hydrogen and water become miscible in all proportions. We use this knowledge to map out the critical curve for the hydrogen-water system: the locus of temperatures and pressures dividing the phase space into regions where hydrogen and water are miscible in all proportions and only partially miscible/immiscible. We find that the critical curve lies approximately at 2 GPa at 1000 K, going to 100 GPa at 4000 K, and then becomes approximately constant in temperature, at least up to 2000 GPa. The resulting curve is in good agreement with the experimental results of Bali et al. (2013) at temperatures of $\sim$ 1200 K and consistent with the critical curve determined by Seward & Franck (1981) at temperatures of $\sim$ 650 K. Interestingly, a comparison of this critical curve with the melting curve of pure water shows that presence of hydrogen can suppress the crystallization of water, especially in the regime where the corresponding phase of pure water-ice is the superionic Ice XVIII. This behavior is likely due to the higher entropy of a superionic ice phase making it more susceptible to mixing with hydrogen over Ice X. On the other hand, we find that the flattening out of the critical at temperatures of $\gtrsim$ 100 GPa closely follows the boundary predicted for the metallization of pure hydrogen.

Finally, we discuss the insights the critical curve provides into the formation, evolution, and interior structure of the ice giants. To this end, we present a comparison of the critical curve with (1) the adiabats of the ice giants predicted by Nettelmann et al. (2013), and (2) the density-pressure profiles for the ice giants based on their respective observational constraints such as mass, radius, rotation period and gravity measurements, as determined by Movshovitz & Fortney (2022). This comparison yields several fascinating insights. For instance, there should inevitably be compositional gradients inside Neptune and Uranus.

In fact, we expect multiple regions where hydrogen and water are completely mixed and regions with compositional gradients. This assertion, while tentative, is corroborated by the fact that the pressure depths where the slope of the density-pressure profiles change for Uranus and Neptune and where the critical curve for hydrogen-water system and their respective adiabats crossover each time are strongly correlated. In addition, given the ability of hydrogen to suppress the crystallization of water ice, we expect the deep interior, $\sim$ 200 - 500 GPa, of these planets to have a large ocean of a fluid hydrogen and water mixture. It is likely that this shell is highly electrically conducting and thus is the sought-after thin conductive, convecting shell where the highly non-dipolar magnetic field of these ice giants are generated (e.g., Stanley & Bloxham, 2004).

We expect Neptune and Uranus to have a similar interior structure by virtue of similarities in their similar physical properties. However, if Uranus' deep interior is hotter than Neptune's, as predicted by Nettelmann et al. (2013) and other studies, water and hydrogen would be less demixed in Uranus' interior. Therefore, any compositional or structural changes inside Uranus are bound to be less pronounced, i.e., Uranus should have a smoother density-pressure profile than Neptune. This, too, is consistent with the observational constraints. What then naturally follows from this argument is that Neptune and Uranus should have had even more homogeneous interiors of water-hydrogen mixtures in the past. Only lately, on astronomical timescales, water and hydrogen must have started to demix in their interior. A consequence of this demixing is the release of gravitational potential energy. Since Neptune's interior is more demixed than Uranus, the gravitational energy released should be more significant for Neptune than Uranus. This excess energy is then the likely source of Neptune's higher internal heat flux than that observed for Uranus, as first suggested in Bailey & Stevenson (2021) (see also Stevenson & Salpeter, 1977a,b). Thus, understanding the mixing behavior of hydrogen and water helps elucidate the phys-

ical and chemical processes behind the observed difference in the luminosities of the ice giants within a self-consistent framework. Finally, we also present arguments to explain why Uranus' magnetic field strength is much larger than that observed for Neptune despite having similar physical attributes, including magnetic field morphologies.

Some of our inferences require more detailed calculations and follow-up observations. Nevertheless, our work shows the undeniable importance of understanding how planetary constituents interact. This is especially true as we move into an era of *James Webb Space Telescope*, which has started to provide unprecedented observational constraints on the composition of exoplanetary atmospheres. Furthermore, this work underscores the importance of understanding Uranus and Neptune which can provide us with the best benchmarks to better comprehend the physical and chemical processes that dictate formation and evolution of planets and their envelopes. But again, without further efforts toward developing a fundamental understanding of how the dominant planet-building materials interact (e.g., hydrogen, helium, silicates, methane, iron), this will not be possible.

CHAPTER 7

Summary

Motivated by a revolution in observational astronomy over the last quarter century, which has led to the discovery of thousands of exoplanets, we present a series of projects in this thesis where we explored the origin, evolution, and structure of planets in our local Galactic neighborhood. We summarize our main takeaways and results below:

1. **The core-powered mass-loss mechanism can explain the 'radius valley' observed in the distribution of small exoplanets, independent of photoevaporation** (Gupta & Schlichting, 2019)

   In this work, we investigated the origin of the radius valley observed in the distribution of small exoplanets. We explored the idea that if a typical planet completes its formation in the presence of its protoplanetary gas disk, it would also accrete a hydrogen-dominated atmosphere. Once this atmosphere becomes optically thick during the formation process, any energy loss from the planet would be regulated by radiative diffusion across the radiative-convective boundary of its atmosphere. This would slow down the rate at which the planet loses its primordial energy of formation.

   Later in the planet's evolution, once the protoplanetary gas disk has dissipated and after the spontaneous mass-loss process instigated by the disk dispersal, all of this primordial energy of formation and the host star's bolometric luminosity can drive a

hydrodynamic wind leading to atmosphere loss. Eventually, certain planets can lose their atmospheres entirely, becoming rocky super-Earths. Planets that survive with their primordial atmospheres are today's sub-Neptunes.

We use a simple analytic model to demonstrate how this idea can explain the observed planet population around Sun-like stars. We demonstrate that whether a planet becomes a super-Earth or a sub-Neptune primarily depends on the balance between its cooling and mass-loss timescales. We infer that such planets have a mass distribution that peaks around 4 Earth masses and find that they are likely to have a bulk interior composition similar to Earth's.

2. **Core-powered mass-loss theory can self-consistently explain, and predict, observations across the phase space of planet size and host star properties** (Gupta & Schlichting, 2020)

   In this study, we extended our previous work to explore the impact of host star properties on planet demographics under the core-powered mass-loss mechanism. We showed that this theory self-consistently explains how the radius valley changes with stellar mass and stellar metallicity for Sun-like stars, and in addition, we presented predictions for changes with stellar age.

   We found that planets are more susceptible to losing their atmospheres around more massive stars. This is because more massive stars are also more luminous, and the increased luminosity can drive a stronger hydrodynamic wind that can strip away the planet's atmosphere. Furthermore, we demonstrated that metal-rich stars are more likely to host larger sub-Neptunes. The reason behind this trend with metallicity is that metal-rich stars are more likely to host planets with metal-rich atmospheres, and such planets, in turn, are expected to have higher atmospheric opacities leading to

slower cooling rates. Finally, we showed that planets would lose their primordial atmospheres on timescales of roughly 0.5 to a few billion years under core-powered mass-loss. This prediction has since been confirmed by observational studies.

3. **Several planet candidates can be identified that are likely losing their atmospheres today, including those that might host secondary atmospheres or ice-rich interiors** (Gupta & Schlichting, 2021)

   In complement to planet demographic studies, we developed a hybrid planet evolution-Bayesian inference model to analyze the evolution of individual small exoplanets for which we have observational constraints on their mass, size and host star properties such as mass, luminosity and age. Our objective was to shortlist candidates that could be losing their atmospheres today if their evolution is indeed dictated by core-powered mass-loss. We found that the following planets are likely losing their atmospheres at a rate $\gtrsim 10^7$ g/s at 50 percent confidence level: pi Men c, Kepler-60 d, Kepler-60 b, HD 86226 c, EPIC 249893012 b, Kepler-107 c, HD 219134 b, Kepler-80 e, Kepler-138 d, and GJ 9827 d.

   In addition, we identified several additional planet candidates that likely harbor secondary atmospheres with high mean molecular weight or low-density interiors rich in ices, or both. We found that the following are likely to be such planets: WASP-47 e, Kepler-78 b, Kepler-10 b, CoRoT-7 b, HD 80653 b, 55 Cnc e, and Kepler-36 b.

4. **Planet surveys for M-dwarf planets are excellent test-beds for distinguishing between the leading radius valley theories such as core-powered mass-loss and photoevaporation** (Gupta et al., 2022)

   M-dwarfs are by far the most common type of stars in our universe, and they are also

the most suitable for discovering super-Earths and sub-Neptunes, given their small size. In this work, we investigated planet demographics around low-mass stars, i.e., M-dwarfs, while accounting for their evolving bolometric luminosity, which can change by up to two orders of magnitude over a timescale of hundreds of millions years.

We found that if planet evolution is indeed dictated by core-powered mass-loss, the slope or shape of the radius valley is, to the first order, the same across stellar masses in the planet size-orbital period space, as reported in recent observational studies. At the same time, we expect the slope of the radius valley to decrease with stellar mass. Furthermore, we showed how this slope depends on the stellar mass-luminosity relationship and, on the same note, how different observational surveys might find different slopes for the radius valley depending on the particulars of their stellar sample.

Finally, we found that surveys for planets around M-dwarfs can be especially fruitful in distinguishing between the predictions of the two leading theories on the origin of the radius valley, namely, core-powered mass-loss and photoevaporation. Both these theories successfully explains planet demographics around Sun-like stars. However, we found that their predictions diverge for planets around low-mass stars.

5. **Understanding the interaction between hydrogen and water sheds light on the interiors of planets such as Uranus and Neptune**

   We investigated how hydrogen and water interact across the temperature and pressure phase space relevant to the interiors of water-rich planets and exoplanets such as Uranus and Neptune. To achieve this, we performed computational experiments using molecular dynamics simulations based on the density functional theory, as

implemented in the Vienna Ab Initio Simulation Package (VASP). In these calculations, which took around 3 million CPU hours, we allowed pure equilibrated phases of hydrogen and water to interact with each other. We then evaluated their mixing behavior to determine the coexistence and critical curve of the hydrogen-water system.

Our results are in good agreement with past experimental studies. We found that Neptune used to have large regions of its interior where hydrogen and water were completely mixed. At present, it still has such regions, but also regions with compositional gradients where hydrogen and water have started to demix. We expect Uranus to have a similar evolutionary history and qualitatively similar internal layers, but with a less demixed interior. The gravitational energy released due to the greater degree of demixing in Neptune can explain why it has a higher internal heat flux than Uranus. Our results thus shed light on the physical process behind the distinct present-day luminosities of Uranus and Neptune, within a self-consistent framework. At the same time, we found that both planets are likely to have regions in the deep interior where water and hydrogen are completely mixed, in fluid phase and conductive, leading to conditions required for generating magnetic fields of similar morphologies. Our findings are corroborated by the fact that the pressure depths where observationally constrained density-pressure profiles change slopes, which reflects a compositional or structural change, is correlated with the pressure depths where the hydrogen-water critical curve and the ice-giant adiabats cross each other, i.e., where our results predict compositional and structural changes to happen.

Bibliography

Allart, R., Bourrier, V., Lovis, C., et al. 2018, Science, 362, 1384

Almenara, J. M., Díaz, R. F., Dorn, C., Bonfils, X., & Udry, S. 2018, MNRAS, 478, 460

Angelo, I., & Hu, R. 2017, AJ, 154, 232

Bailey, E., & Stevenson, D. J. 2021, PSJ, 2, 64

Bali, E., Audétat, A., & Keppler, H. 2013, Nature, 495, 220

Batalha, N. M., Borucki, W. J., Bryson, S. T., et al. 2011, ApJ, 729, 27

Bean, J. L., Raymond, S. N., & Owen, J. E. 2021, Journal of Geophysical Research (Planets), 126, e06639

Becker, J. C., Vanderburg, A., Adams, F. C., Rappaport, S. A., & Schwengeler, H. M. 2015, ApJ, 812, L18

Benneke, B., Knutson, H. A., Lothringer, J., et al. 2019, Nature Astronomy, 3, 813

Benz, W., Broeg, C., Fortier, A., et al. 2021, Experimental Astronomy, 51, 109

Berger, T. A., Huber, D., Gaidos, E., & van Saders, J. L. 2018, ApJ, 866, 99

Berger, T. A., Huber, D., Gaidos, E., van Saders, J. L., & Weiss, L. M. 2020a, AJ, 160, 108

Berger, T. A., Huber, D., van Saders, J. L., et al. 2020b, AJ, 159, 280

Bergermann, A., French, M., & Redmer, R. 2021, Phys. Chem. Chem. Phys., 23, 12637

Biersteker, J. B., & Schlichting, H. E. 2021, MNRAS, 501, 587

Bonomo, A. S., Zeng, L., Damasso, M., et al. 2019, Nature Astronomy, 3, 416

Borucki, W. J., Koch, D., Basri, G., et al. 2010, Science, 327, 977

Bourrier, V., Ehrenreich, D., King, G., et al. 2017, A&A, 597, A26

Bourrier, V., Lecavelier des Etangs, A., Ehrenreich, D., et al. 2018, A&A, 620, A147

Bower, D. J., Kitzmann, D., Wolf, A. S., et al. 2019, arXiv e-prints, arXiv:1904.08300

Brown, T. M., Latham, D. W., Everett, M. E., & Esquerdo, G. A. 2011, AJ, 142, 112

Cahn, J. W., & Hilliard, J. E. 1958, The Journal of chemical physics, 28, 258

Carleo, I., Youngblood, A., Redfield, S., et al. 2021, arXiv e-prints, arXiv:2101.06277

Carter, J. A., Agol, E., Chaplin, W. J., et al. 2012, Science, 337, 556

Casertano, S., Lattanzi, M. G., Sozzetti, A., et al. 2008, A&A, 482, 699

Chachan, Y., & Stevenson, D. J. 2018, ApJ, 854, 21

Chao, K.-H., deGraffenried, R., Lach, M., et al. 2020, arXiv e-prints, arXiv:2012.07337

Charbonneau, D., Brown, T. M., Latham, D. W., & Mayor, M. 2000, ApJ, 529, L45

Charbonneau, D., Berta, Z. K., Irwin, J., et al. 2009, Nature, 462, 891

Chen, H., & Rogers, L. A. 2016, ApJ, 831, 180

Choi, J., Dotter, A., Conroy, C., et al. 2016, ApJ, 823, 102

Christiansen, J. L., Clarke, B. D., Burke, C. J., et al. 2015, ApJ, 810, 95

Cloutier, R., & Menou, K. 2020, AJ, 159, 211

Connerney, J. E. P., Acuna, M. H., & Ness, N. F. 1987, J. Geophys. Res., 92, 15329

—. 1991, J. Geophys. Res., 96, 19023

Dai, F., Masuda, K., Winn, J. N., & Zeng, L. 2019, ApJ, 883, 79

Demory, B.-O., Gillon, M., Madhusudhan, N., & Queloz, D. 2016a, MNRAS, 455, 2018

Demory, B.-O., Gillon, M., de Wit, J., et al. 2016b, Nature, 532, 207

Dong, S., Xie, J.-W., Zhou, J.-L., Zheng, Z., & Luo, A. 2018, Proceedings of the National Academy of Science, 115, 266

Dorn, C., Harrison, J. H. D., Bonsor, A., & Hands, T. O. 2019, MNRAS, 484, 712

Dorn, C., & Heng, K. 2018, ApJ, 853, 64

Dorn, C., Hinkel, N. R., & Venturini, J. 2017a, A&A, 597, A38

Dorn, C., Venturini, J., Khan, A., et al. 2017b, A&A, 597, A37

dos Santos, L. A., Ehrenreich, D., Bourrier, V., et al. 2020, A&A, 634, L4

Dotter, A. 2016, ApJS, 222, 8

Doyle, A. E., Young, E. D., Klein, B., Zuckerman, B., & Schlichting, H. E. 2019, Science, 366, 356

Dressing, C. D., Charbonneau, D., Dumusque, X., et al. 2015, ApJ, 800, 135

Ehrenreich, D., Bourrier, V., Bonfils, X., et al. 2012, A&A, 547, A18

Ehrenreich, D., Bourrier, V., Wheatley, P. J., et al. 2015, Nature, 522, 459

Eker, Z., Bakış, V., Bilir, S., et al. 2018, MNRAS, 479, 5491

Elkins-Tanton, L. T., & Seager, S. 2008, ApJ, 685, 1237

Esteves, L. J., de Mooij, E. J. W., Jayawardhana, R., Watson, C., & de Kok, R. 2017, AJ, 153, 268

Feroz, F., Hobson, M. P., & Bridges, M. 2009, MNRAS, 398, 1601

Fischer, D. A., & Valenti, J. 2005, ApJ, 622, 1102

Flyvbjerg, H., & Petersen, H. G. 1989, J. Chem. Phys., 91, 461

Fortney, J. J., Marley, M. S., & Barnes, J. W. 2007, ApJ, 659, 1661

Freedman, R. S., Marley, M. S., & Lodders, K. 2008, ApJS, 174, 504

French, M., Desjarlais, M. P., & Redmer, R. 2016, Phys. Rev. E, 93, 022140

Fressin, F., Torres, G., Charbonneau, D., et al. 2013, ApJ, 766, 81

Frustagli, G., Poretti, E., Milbourne, T., et al. 2020, A&A, 633, A133

Fulton, B. J., & Petigura, E. A. 2018, AJ, 156, 264

Fulton, B. J., Petigura, E. A., Howard, A. W., et al. 2017, AJ, 154, 109

Gaidos, E., Hirano, T., Mann, A. W., et al. 2020, MNRAS, 495, 650

Gandolfi, D., Barragán, O., Livingston, J. H., et al. 2018, A&A, 619, L10

García Muñoz, A., Youngblood, A., Fossati, L., et al. 2020, ApJ, 888, L21

Gaudi, B. S. 2022, in Astrophysics and Space Science Library, Vol. 466, Demographics of Exoplanetary Systems, Lecture Notes of the 3rd Advanced School on Exoplanetary Science, ed. K. Biazzo, V. Bozza, L. Mancini, & A. Sozzetti, 237–291

Gillon, M., Jehin, E., Lederer, S. M., et al. 2016, Nature, 533, 221

Gillon, M., Triaud, A. H. M. J., Demory, B.-O., et al. 2017, Nature, 542, 456

Ginzburg, S., Schlichting, H. E., & Sari, R. 2016, ApJ, 825, 29

—. 2018, MNRAS, 476, 759

Greene, T. P., Line, M. R., Montero, C., et al. 2016, ApJ, 817, 17

Gupta, A., Nicholson, L., & Schlichting, H. E. 2022, MNRAS, 516, 4585

Gupta, A., & Schlichting, H. E. 2019, MNRAS, 487, 24

—. 2020, MNRAS, 493, 792

—. 2021, MNRAS, 504, 4634

Hadden, S., & Lithwick, Y. 2014, ApJ, 787, 80

—. 2017, AJ, 154, 5

Helled, R., Anderson, J. D., Podolak, M., & Schubert, G. 2011, ApJ, 726, 15

Hidalgo, D., Pallé, E., Alonso, R., et al. 2020, A&A, 636, A89

Higson, E., Handley, W., Hobson, M., & Lasenby, A. 2019, Statistics and Computing, 29, 891

Hirano, T., Dai, F., Gandolfi, D., et al. 2018, AJ, 155, 127

Holmström, E., Stixrude, L., Scipioni, R., & Foster, A. S. 2018, Earth and Planetary Science Letters, 490, 11

Hood, C. E., Fortney, J. J., Line, M. R., et al. 2020, AJ, 160, 198

Hoover, W. G. 1985, Phys. Rev. A, 31, 1695

Howard, A. W., Sanchis-Ojeda, R., Marcy, G. W., et al. 2013, Nature, 503, 381

Hsu, D. C., Ford, E. B., & Terrien, R. 2020, MNRAS, 498, 2249

Hu, R., Seager, S., & Yung, Y. L. 2015, ApJ, 807, 8

Hubbard, W. B., Podolak, M., & Stevenson, D. J. 1995, in Neptune and Triton, 109–138

Inamdar, N. K., & Schlichting, H. E. 2015, MNRAS, 448, 1751

Ito, Y., Ikoma, M., Kawahara, H., et al. 2015, ApJ, 801, 144

Jackson, A. P., Davis, T. A., & Wheatley, P. J. 2012, MNRAS, 422, 2024

Jensen, A. G., Redfield, S., Endl, M., et al. 2012, ApJ, 751, 86

Jin, S., & Mordasini, C. 2018, ApJ, 853, 163

Jin, S., Mordasini, C., Parmentier, V., et al. 2014, ApJ, 795, 65

Jindal, A., de Mooij, E. J. W., Jayawardhana, R., et al. 2020, AJ, 160, 101

Johnson, J. A., Petigura, E. A., Fulton, B. J., et al. 2017, AJ, 154, 108

Jontof-Hutter, D., Ford, E. B., Rowe, J. F., et al. 2016, ApJ, 820, 39

JWST Transiting Exoplanet Community Early Release Science Team, Ahrer, E.-M., Alderson, L., et al. 2023, Nature, 614, 649

Kasper, D., Bean, J. L., Oklopčić, A., et al. 2020, AJ, 160, 258

Kasper, D., Bean, J. L., Line, M. R., et al. 2023, AJ, 165, 7

Kite, E. S., & Barnett, M. N. 2020, Proceedings of the National Academy of Science, 117, 18264

Kite, E. S., Fegley, Bruce, J., Schaefer, L., & Gaidos, E. 2016, ApJ, 828, 80

Kivelson, M. G., & Bagenal, F. 2014, in Encyclopedia of the Solar System (Third Edition), third edition edn., ed. T. Spohn, D. Breuer, & T. V. Johnson (Boston: Elsevier), 137–157. https://www.sciencedirect.com/science/article/pii/B9780124158450000074https://www.sciencedirect.com/

Kohn, W., & Sham, L. J. 1965, Physical Review, 140, 1133

Koposov, S., Speagle, J., Barbary, K., et al. 2023, v2.1.1, Zenodo, doi:10.5281/zenodo.7832419

Kral, Q., Davoult, J., & Charnay, B. 2020, Nature Astronomy, 4, 769

Kresse, G., & Furthmüller, J. 1996, Phys. Rev. B, 54, 11169

Kresse, G., & Furthmüller, J. 1996, Computational Materials Science, 6, 15

Kresse, G., & Hafner, J. 1993, Phys. Rev. B, 47, 558

Kresse, G., & Joubert, D. 1999, Phys. Rev. B, 59, 1758

Kubyshkina, D., Fossati, L., Erkaev, N. V., et al. 2018, A&A, 619, A151

Kulow, J. R., France, K., Linsky, J., & Loyd, R. O. P. 2014, ApJ, 786, 132

Lang, K. R. 1992, Astrophysical Data I. Planets and Stars.

Lavie, B., Ehrenreich, D., Bourrier, V., et al. 2017, A&A, 605, L7

Lee, E. J., & Chiang, E. 2015, ApJ, 811, 41

—. 2016, ApJ, 817, 90

Lee, E. J., & Connors, N. J. 2020, arXiv e-prints, arXiv:2008.01105

Léger, A., Rouan, D., Schneider, J., et al. 2009, A&A, 506, 287

Ligi, R., Dorn, C., & Crida, A. 2019, in EPSC-DPS Joint Meeting 2019, Vol. 2019, EPSC–DPS2019–840

Lodders, K. 2003, ApJ, 591, 1220

Lopez, E. D., & Fortney, J. J. 2013, ApJ, 776, 2

—. 2014, ApJ, 792, 1

Lopez, E. D., & Rice, K. 2018, MNRAS, 479, 5303

Loyd, R. O. P., Shkolnik, E. L., Schneider, A. C., et al. 2020, ApJ, 890, 23

Luque, R., & Pallé, E. 2022, Science, 377, 1211

MacDonald, M. G., Ragozzine, D., Fabrycky, D. C., et al. 2016, AJ, 152, 105

Malsky, I., & Rogers, L. A. 2020, ApJ, 896, 48

Mamajek, E. E. 2009, in American Institute of Physics Conference Series, Vol. 1158, Exoplanets and Disks: Their Formation and Diversity, ed. T. Usuda, M. Tamura, & M. Ishii, 3–10

Mann, A. W., Gaidos, E., Mace, G. N., et al. 2016, ApJ, 818, 46

Marcy, G. W., Weiss, L. M., Petigura, E. A., et al. 2014a, Proceedings of the National Academy of Science, 111, 12655

Marcy, G. W., Isaacson, H., Howard, A. W., et al. 2014b, ApJS, 210, 20

Markham, S., & Stevenson, D. 2021, PSJ, 2, 146

Marounina, N., & Rogers, L. A. 2020, ApJ, 890, 107

Martinez, C. F., Cunha, K., Ghezzi, L., & Smith, V. V. 2019, ApJ, 875, 29

Mayor, M., & Queloz, D. 1995, Nature, 378, 355

McArthur, B. E., Endl, M., Cochran, W. D., et al. 2004, ApJ, 614, L81

McWilliams, R. S., Dalton, D. A., Mahmood, M. F., & Goncharov, A. F. 2016, Phys. Rev. Lett., 116, 255501

Millot, M., Coppari, F., Rygg, J. R., et al. 2019, Nature, 569, 251

Misener, W., & Schlichting, H. E. 2022, MNRAS, 514, 6025

Motalebi, F., Udry, S., Gillon, M., et al. 2015, A&A, 584, A72

Mousis, O., Deleuil, M., Aguichine, A., et al. 2020, ApJ, 896, L22

Movshovitz, N., & Fortney, J. J. 2022, PSJ, 3, 88

Muirhead, P. S., Hamren, K., Schlawin, E., et al. 2012, ApJ, 750, L37

Nettelmann, N., Helled, R., Fortney, J. J., & Redmer, R. 2013, Planet. Space Sci., 77, 143

Ninan, J. P., Stefansson, G., Mahadevan, S., et al. 2020, ApJ, 894, 97

Niraula, P., Redfield, S., Dai, F., et al. 2017, AJ, 154, 266

Nortmann, L., Pallé, E., Salz, M., et al. 2018, Science, 362, 1388

Oklopčić, A., & Hirata, C. M. 2018, ApJ, 855, L11

Owen, J. E., & Murray-Clay, R. 2018, MNRAS, 480, 2206

Owen, J. E., & Wu, Y. 2013, ApJ, 775, 105

—. 2016, ApJ, 817, 107

—. 2017, ApJ, 847, 29

Parker, E. N. 1958, ApJ, 128, 664

Paxton, B., Bildsten, L., Dotter, A., et al. 2011, ApJS, 192, 3

Paxton, B., Cantiello, M., Arras, P., et al. 2013, ApJS, 208, 4

Paxton, B., Marchant, P., Schwab, J., et al. 2015, ApJS, 220, 15

Paxton, B., Schwab, J., Bauer, E. B., et al. 2018, ApJS, 234, 34

Paxton, B., Smolec, R., Schwab, J., et al. 2019, ApJS, 243, 10

Penny, M. T., Gaudi, B. S., Kerins, E., et al. 2019, ApJS, 241, 3

Perdew, J. P., Ruzsinszky, A., Csonka, G. I., et al. 2008, Phys. Rev. Lett., 100, 136406

Petigura, E. A., Marcy, G. W., & Howard, A. W. 2013, ApJ, 770, 69

Petigura, E. A., Howard, A. W., Marcy, G. W., et al. 2017, AJ, 154, 107

Petigura, E. A., Marcy, G. W., Winn, J. N., et al. 2018, AJ, 155, 89

Petigura, E. A., Rogers, J. G., Isaacson, H., et al. 2022, AJ, 163, 179

Piaulet, C., Benneke, B., Almenara, J. M., et al. 2023, Nature Astronomy, 7, 206

Piso, A.-M. A., & Youdin, A. N. 2014, ApJ, 786, 21

Putnis, A. 1992, An Introduction to Mineral Sciences (Cambridge University Press), doi:10.1017/CBO9781139170383

Queloz, D., Bouchy, F., Moutou, C., et al. 2009, A&A, 506, 303

Rafikov, R. R. 2006, ApJ, 648, 666

Ramirez, R. M., & Kaltenegger, L. 2014, ApJ, 797, L25

Rauer, H., Catala, C., Aerts, C., et al. 2014, Experimental Astronomy, 38, 249

Raymond, S. N., Quinn, T., & Lunine, J. I. 2004, Icarus, 168, 1

Rice, K., Malavolta, L., Mayo, A., et al. 2019, MNRAS, 484, 3731

Ricker, G. R., Winn, J. N., Vanderspek, R., et al. 2015, Journal of Astronomical Telescopes, Instruments, and Systems, 1, 014003

Ridden-Harper, A. R., Snellen, I. A. G., Keller, C. U., et al. 2016, A&A, 593, A129

Rizzuto, A. C., Vanderburg, A., Mann, A. W., et al. 2018, AJ, 156, 195

Rodriguez, J. E., Vanderburg, A., Eastman, J. D., et al. 2018, AJ, 155, 72

Rogers, J. G., Gupta, A., Owen, J. E., & Schlichting, H. E. 2021, MNRAS, 508, 5886

Rogers, J. G., & Owen, J. E. 2020, arXiv e-prints, arXiv:2007.11006

Rogers, J. G., Schlichting, H. E., & Owen, J. E. 2023, ApJ, 947, L19

Rogers, L. A. 2015, ApJ, 801, 41

Rogers, L. A., & Seager, S. 2010, ApJ, 712, 974

Rowe, J. F., Bryson, S. T., Marcy, G. W., et al. 2014, ApJ, 784, 45

Salaris, M., & Cassisi, S. 2005, Evolution of Stars and Stellar Populations

Scalo, J., Kaltenegger, L., Segura, A. G., et al. 2007, Astrobiology, 7, 85

Schaefer, L., & Fegley, B. 2009, ApJ, 703, L113

Scheibe, L., Nettelmann, N., & Redmer, R. 2021, A&A, 650, A200

Schlichting, H. E., Sari, R., & Yalinewich, A. 2015, Icarus, 247, 81

Schlichting, H. E., & Young, E. D. 2022, PSJ, 3, 127

Scipioni, R., Stixrude, L., & Desjarlais, M. P. 2017, Proceedings of the National Academy of Science, 114, 9009

Seager, S., Kuchner, M., Hier-Majumder, C. A., & Militzer, B. 2007, ApJ, 669, 1279

Seager, S., & Sasselov, D. D. 2000, ApJ, 537, 916

Seward, T. M., & Franck, E. U. 1981, Berichte der Bunsengesellschaft für physikalische Chemie, 85, 2

Shaikhislamov, I. F., Fossati, L., Khodachenko, M. L., et al. 2020, A&A, 639, A109

Skilling, J. 2004, in American Institute of Physics Conference Series, Vol. 735, American Institute of Physics Conference Series, ed. R. Fischer, R. Preuss, & U. V. Toussaint, 395–405

Skilling, J. 2006, Bayesian Anal., 1, 833

Soubiran, F., & Militzer, B. 2015, ApJ, 806, 228

Spake, J. J., Sing, D. K., Evans, T. M., et al. 2018, Nature, 557, 68

Speagle, J. S. 2020, MNRAS, 493, 3132

Stanley, S., & Bloxham, J. 2004, Nature, 428, 151

—. 2006, Icarus, 184, 556

Steffen, J. H., Fabrycky, D. C., Agol, E., et al. 2013, MNRAS, 428, 1077

Stevenson, D. J., & Salpeter, E. E. 1977a, ApJS, 35, 221

—. 1977b, ApJS, 35, 239

Stixrude, L., Baroni, S., & Grasselli, F. 2021, PSJ, 2, 222

Tabernero, H. M., Allende Prieto, C., Zapatero Osorio, M. R., et al. 2020, arXiv e-prints, arXiv:2009.10122

Teske, J., Díaz, M. R., Luque, R., et al. 2020, AJ, 160, 96

Tsiaras, A., Rocchetto, M., Waldmann, I. P., et al. 2016, ApJ, 820, 99

Tu, L., Johnstone, C. P., Güdel, M., & Lammer, H. 2015, A&A, 577, L3

Valencia, D., O'Connell, R. J., & Sasselov, D. 2006, Icarus, 181, 545

Van Eylen, V., Agentoft, C., Lundkvist, M. S., et al. 2018, MNRAS, 479, 4786

Van Eylen, V., Astudillo-Defru, N., Bonfils, X., et al. 2021, arXiv e-prints, arXiv:2101.01593

Vazan, A., & Helled, R. 2020, A&A, 633, A50

Vidal-Madjar, A., Lecavelier des Etangs, A., Désert, J. M., et al. 2003, Nature, 422, 143

Vissapragada, S., Jontof-Hutter, D., Shporer, A., et al. 2020, AJ, 159, 108

Vogt, S. S., Burt, J., Meschiari, S., et al. 2015, ApJ, 814, 12

Waalkes, W. C., Berta-Thompson, Z., Bourrier, V., et al. 2019, AJ, 158, 50

Wahl, S. M., Hubbard, W. B., Militzer, B., et al. 2017, Geophys. Res. Lett., 44, 4649

Wallack, N. L., Knutson, H. A., Morley, C. V., et al. 2019, AJ, 158, 217

Weiss, L. M., & Marcy, G. W. 2014, ApJ, 783, L6

Wolszczan, A., & Frail, D. A. 1992, Nature, 355, 145

Wu, Y. 2019, ApJ, 874, 91

Yan, F., & Henning, T. 2018, Nature Astronomy, 2, 714

Zahnle, K., Kasting, J. F., & Pollack, J. B. 1990, Icarus, 84, 502

Zeng, L., Jacobsen, S. B., Sasselov, D. D., et al. 2019, Proceedings of the National Academy of Science, 116, 9723

Zhang, M., Knutson, H. A., Wang, L., et al. 2020, arXiv e-prints, arXiv:2012.02198

Zink, J. K., Hardegree-Ullman, K. K., Christiansen, J. L., et al. 2020, AJ, 160, 94